EFFICIENT CONSERVATIVE NUMERICAL METHODS FOR FLUID FLOW PROBLEMS WITH INTERFACES

HOM NATH KANDEL

A DISSERTATION SUBMITTED TO
THE FACULTY OF GRADUATE STUDIES
IN PARTIAL FULFILMENT OF THE REQUIREMENTS
FOR THE DEGREE OF
DOCTOR OF PHILOSOPHY

GRADUATE PROGRAM IN MATHEMATICS AND STATISTICS
YORK UNIVERSITY
TORONTO, ONTARIO

FEBRUARY, 2021

Abstract

The surface fluid flows coupled with porous media flows have many applications in science and engineering. The mathematical models are the coupled partial differential equations with interface conditions. It is of importance to develop efficient numerical methods for modeling and analyzing these interface problems. In the dissertation, we first investigate the long wave solutions for the surface flows on inclined porous media. The flows are derived by the Navier-Stokes equations governing the clear flows in the surface fluids and the nonlinear Forchheimers flow equations are for the porous media flows in substrates. We derive out a corresponding Orr-Sommerfeld problem by linearizing the infinitesimal perturbations in the system of coupled equations for analyzing the long wave solutions of surface flows. Numerical analysis is further developed by using Chebyshev collocation method to its eigenvalue problems to analyze critical condition and stable regions of long wave solutions. Secondly, a new mass preserving solution-flux scheme is proposed for solving parabolic multilayer interface problems. The domain is divided into staggered meshes for layers. At regular grid points in each subdomain, the solution-flux scheme is proposed to approximate the equation. The important feature of the work is that at the irregular grid points, the novel corrected approximate fluxes from two sides of the interface are proposed by combining with the interface jump conditions, which ensure the developed solution-flux scheme mass conservative while keeping accuracy. We prove theoretically that our scheme satisfies mass conservation in the discrete form over the whole domain for the interface equations. Numerical experiments show mass conservation and convergence orders of our scheme and the application of the heat propagation in the multilayer media. Thirdly, an efficient conservative pressure-velocity scheme for coupled free and porous media flow system is proposed. The Stokes equations are applied in the free flow domain and Darcy's law is used to model the porous media flow. The system couples the two flows of an incompressible fluid at fluid-porous media interface via an appropriate set of interface conditions including the Beavers-Joseph-Saffman condition. Based on the efficient treatments of the interface conditions, a time-splitting conservative pressure-velocity scheme within a staggered grid framework is developed to solve primitive variables in the free and porous media flow system. We prove theoretically that our scheme satisfies mass conservation in discrete form over the whole domain. Numerical simulations are carried out for two model problems, two real model problems and a realistic problem. Numerical results show the convergence, mass conservation and excellent performance of the proposed scheme.

Acknowledgments

First and foremost I offer my sincerest gratitude to my supervisor Professor Dong Liang who supported me throughout my thesis with his patience and knowledge. I attribute the level of my Ph.D degree to his encouragement and effort; without him this thesis would not have been completed or written. I am always indebted to him for his valuable time and guidance.

Besides my supervisor, I would like to thank the rest of my thesis committee members Professors Michael C Haslam and Yuehua Wu for their encouragement and valuable suggestions. At the same time I would like to thank my nephew Narayan for his technical support. Also I would like to thank York University for giving me the valuable opportunity to study in the Applied Mathematics program. Last but not the least, I would like to thank my parents, my wife Sita, my son Anupam and my daughter Alina for their sacrifices, unconditional support and love throughout all my studies at York University.

Contents

List of Figures

List of Tables

Chapter 1

Introduction

1.1 Background

The fluid flows overlying porous media have many applications in science and engineering, such as coating, mass transfer process in chemical technology, mass transfer in different phases such as clear surface and filters, connection within surface water and soil system, and ground-water flow through fractures [4, 15, 25, 27, 29, 65]. Many other environmental and biological problems also involve interfaces, such as continuous casting in the metallurgical industry, the freezing process of perishable food-stuffs in the food engineering, the magnetic fluid hypothermia treatment of cancer [2, 5, 7, 94]. The mathematical models describing these processes are coupled interface partial differential equations, where interface conditions are established to couple the systems along the interfaces. Modeling coupled interface free and porous media flows has recently obtained increasing interest in both mathematical and numerical points of view due to the importance of the problems. It is very important to develop highly efficient numerical methods in modeling and analyzing the free and porous media flow systems with interfaces.

The Newtonian surface fluid flow on an inclined porous media plane is an active research area due to its inertial instability that appears in the interfacial waves. Waves are common occurrences in laminar fluid films flowing on porous media surfaces, which are recognized as instability of uniform films, as well as reported in experimental studies (See more details, for examples, in [6, 11, 13, 21, 34, 67, 70, 79, 93]). A study based on the assumption of slow filtration flow due to low permeability was carried out by Pascal [68], where a slip condition is assumed at fluid-porous medium interface based on experimental results in Beavers and Joseph's [8]. Extension studies on one-sided models were taken for nonlinear effect [79, 82], and non-Newtonian rheology [69], etc.

The long-wave structures resulted from isothermal flows that appear on an inclined plane (or vertical wall) have attracted many researches since the pioneering experiment was done by Kapitza and Kapitza [47]. The studies of fluid flows down impermeable inclined planes were done in Benjamin [10] and Yin [91], where the critical conditions for the onset of stability were obtained from solutions of the Orr-Sommerfeld equations for the long-wave solutions of perturbation problems. Gravity-driven flows down inclined impermeable planes were futher studied on different aspects of the flows, summarized in the review papers by Kalliadasis et al. [41] and Craster and Matar [20]. Moreover, many experimental studies have recently been done in linear stability and dynamics of the free surface waves of a gravity driven flow down in inclined plane to analyze steady-state and perturbation flows. Trifonov [86] investigated for linear and nonlinear stability in corrugated incline plane focusing their transformation due to the wall corrugations; and Dauth and Aksel [22] performed on the evolution of nonlinear traveling free surface wave over strongly undulated inclines and focused on the impact of the substrates' shape and periodicity on the traveling wave.

Efforts on numerical stability have been made for free-surface flows with permeable substrates. Liu and Liu [61] conducted a linear stability analysis of the surface flow over porous media where the Darcy's law governs filtration flow and Beavers-Joseph condition is considered at the fluid-porous medium interface. Samanta et al. [81] applied a composite formulation to the whole system under an assumed vertical variation of the medium. Kandel and Pascal[42] studied on the coupling free surface flow and flow through filtration where Darcy's law and Jones' condition were applied at the fluid-porous medium interface.

On the other hand, nonlinear Forchheimer's law [31] along with Brinkman's law describes different fluid flows through porous media [39, 53, 67, 72, 73, 87]. It is important to study the critical conditions for the onset of instability of surface-flow over the porous media with nonlinear Forchheimer's law and the long wave solutions of the flows. To our best knowledge, there is no work on the surface flow coupled by nonlinear Forchheimer's porous media flow, where nonlinear Forchheimer's law describes the porous media flow through filtration substrates.

Interface partial differential equations (PDEs) are very important in many problems that involve diffusion processes with interfaces; such as, continuous casting and contaminant diffusion across interfaces soils. These applications have attracted a lot of attention from both theoretical and numerical analysts in recent years. The models are the interface parabolic equations where there are solution-jump conditions and flux-jump conditions along multiple interfaces of the domains. The solutions to interfaces problems basically are non-smooth or even discontinuous across the interfaces because the input data (such as diffusion coefficients of differential equations, sources terms etc.) across the interfaces of these problem may be discontinuous or singular in one or several interfaces in the solution domain.

Numerical methods designed for smooth solutions do not work or work poorly for interface problems. Some finite difference methods have been proposed in the literature for solving interface problems. For solving elliptic equations with discontinuous coefficients and singular sources, the immersed interface FD method was proposed in [52] where a local correction of finite difference on irregular grid points are pursued throughout the domain by incorporating interface jump conditions. Further improvements of finite difference methods for interface elliptic equations have been done such as the schemes based on fictitious-domain in [95] and a scheme preserving discrete maximum principle in [57]. Papers [30, 63] introduced the Ghost-Fluid method for solving a two-phase problem with interfaces and solving the elliptic equations in the presence of interfaces respectively, where the fictitious values (ghost values) on the grid points on the other side of the interface (ghost points) are found by an extrapolation. [89] proposed a jump condition capturing finite difference method for elliptic interface problems. The immersed interface method has also achieved a tremendous success in solving parabolic interface problems [56]. The finite difference schemes for solving parabolic interface problems have been developed in [35, 45, 54, 94]. It is more important to solve efficiently in a large linear system at each time step in implicit time stepping for parabolic interfaces problems. [54, 60, 94] offered different approaches especially by reducing a multidimensional system to set of independent one dimensional systems in finite difference schemes without considering interface conditions. The papers developed tensor-product decomposition of jump conditions which decouples 2D jump conditions into 1D ones as spirit of splitting method. Then these 1D conditions are applied into the matched interface and boundary (MIB) scheme [36] in the matched ADI schemes.

However, these previous schemes do not satisfy mass conservation for the interface problems. Without interfaces, recently some of work has been done by combining the operator splitting technique and the solution-flux coupled scheme on staggered meshes. The papers [23, 96, 97, 98] proposed the mass conservation domain decomposition methods for parabolic equations and convection- diffusion equations with constant and variables diffusion coefficients. On the other hand, recent flourish in research activity has been focused on analytical and numerical methods for solving multi-layer diffusion problems [17, 24, 33, 46, 59, 62, 64, 76]. But, there is no work on mass-preserving schemes to time-dependent diffusion equations with multi-layers. To develop the mass-preserving finite difference numerical schemes is of great importance for solving the problems with interfaces. It is a challenging task to develop the mass-preserving finite difference schemes for the parabolic multi-layer equations with jump conditions at interfaces.

The fluid transport phenomena across the interface between free flow region and porous media are exhibited in many applications. Stokes-Darcy model has been extensively studied in the recent years due to its wide range of natural problems and industrial settings such as overland flow interactions with groundwater aquifers, filtration processes, flow in veggy porous media. When dealing with numerical methods to solve 2D free flow, projection method was introduced years ago by Chorin [18] and independently by Temam [85] as a way of computing efficiently the solutions of incompressible Navier-Stokes equations (NSE). Over the years projection method has played a dominant role in the computation of viscous incompressible flows based on the primitive variable formulation. It is getting increasingly popular in applications to viscous incompressible flows at low to moderate Reynolds number. With periodic boundary conditions, the performance of the projection method is well-understood from the work of Chorin [19]. The most well-known primitive variables projection methods are works by [9, 48] in Navier-Stokes equations. Some projection methods in Navier-Stokes or Stokes are presented in [1, 14, 84, 92]. Projection method was based on the following philosophy: In incompressible flows, pressure does not carry any thermodynamic meaning and is present only as a Lagrange multiplier for the incompressibility constraint [19].

In the free flow region, Stokes equations are used to describe momentum conservation while Darcy's law is applied as an approximation conservation of momentum equation in the porous medium [77]. The coupling between free flow and porous medium domains can be done through the sharp interface approach by setting a suitable set of interface conditions at boundary between the flow domain [26, 66, 75, 88] or by taking a transition zone between two flow regions and developing a transition region model [37]. At the sharp interface, the Beavers-Joseph velocity jump condition [8] is a common practice to couple the two different flow domains, in conjunction with restrictions that arise due to mass conservation and balance of normal forces across the interface.The Beaver-Joseph condition establishes the connection between the free flow velocity and the porous medium velocity tangent to the interface, and it is an additional condition to couple equations of different orders. [80] proposed a modification of the Beaver-Joseph- Saffman condition that contains only variables in the free flow region, since the porous medium velocity is much smaller than the free flow velocity, and can thus be neglected.

Several numerical methods have been developed for solving the coupled systems. Vast majority of study in this area is based on finite element method [50]. A finite volume method has been studied by [78] and finite difference method has been studied by [50, 55]. There is significantly less effort in finite difference methods to develop conservative numerical methods for the free and porous media flow system. The mass conservation is an important physical law in coupling surface and porous media flows. To preserve the mass over the whole domain is important for developing numerical methods to solve the time-dependent coupled system of free and porous media flows.

1.2 Thesis work

Flow processes in a free-fluid region adjacent to a porous medium and interface partial differential equations occur in many relevant applications. In this thesis, we study the coupling system of free-fluid and porous medium and interface partial differential equations to investigate long-wave solutions with small wave-numbers, to develop mass-preserving solution-flux scheme for multi-layer interface parabolic equations in porous media and to develop the efficient conservative pressure-velocity scheme for solving the coupled Stokes-Darcy flows with interface conditions.

In the first part of thesis, consider a model for free surface flow over inclined porous media with nonlinear flow which is described by Forchheimer's law [31]. As velocity increases the transition to nonlinear drag is quite smooth, where the linearity is breakdown and the nonlinear Forchheimer's law describes the flow [31, 67]. Meanwhile, the flow behavior in the porous media also depends on grain's shape and size, not only in fluid properties. The drag coefficient value is directly related to the form drag coefficient of a grain or the elementary porous solid material. Thus, the flow regime exhibits nonlinear velocity affection described by Forchheimer's law [3, 40, 72]. Two-dimensional incompressible Newtonian fluid flow with no external force along the surface of a porous medium is considered. We investigate the long-wave solutions with small wave-numbers for the gravity-driven surface flows on porous media, where the coupled porous media flows satisfies Forchheimer's law. Our focus is to investigate the effects on the long-wave flow solutions of the surface flows coupled with nonlinear Forchheimer porous flows by varying parameters' values underlying on porous media. We consider filtration flows in the substrates by prescribing a variant of the Beavers-Joseph condition modification from Jones [38].

To solve the model which depends on the fluid properties, inclination and permeability of porous medium as well as the relation between the discharge quantity and cross-stream height of free flows, we derive dimensionless system of equations. We introduce the infinitesimal perturbations to study the long-wave solutions where they interact to equilibrium flows, and then the linearized perturbation equation. We carry out analysis of the long wave solutions of the surface flows, where base state solutions are first derived out and the perturbed states for long wave solutions are further analyzed by corresponding Orr-Sommerfeld type equations which is an eigenvalue equation describing the linear two-dimensional modes of disturbance to flow to determine the stability of flow. The critical condition and stable regions of the long wave solutions are then analyzed from the eigenvalue problems of the Orr-Sommerfeld type equations using Chebyshev collocation numerical method. The influences of key parameters $c_F, D_a, \cot\theta, K_a, \alpha_{BJ}$ and ϕ on the stability are studied and analyzed focusing on the long wave solutions. We obtain different neutral stability marginal curves using different sets of parameters. These curves that identify the transitions shift stable and unstable flow regimes can provoke crucial flow stabilization. This work has been published in [43].

In the second part of thesis, we focus on numerical solution of multi-interfaces partial differential equations. The mass conservation is an important physical feature of the flow and heat process. Developing mass-preserving finite difference numerical schemes is important and challenging for solving interface parabolic equations. In this part, we develop a new mass-preserving solution-flux finite difference scheme for solving time-dependent multi-layer problems where there are solution-jump conditions and flux-jump conditions along interfaces. In the construction of scheme, the domain is divided into staggered meshes for layers. The operator splitting technique is first applied to solve the problems. The solution and flux scheme is proposed to solve it at regular grid points in each layer or subdomain. However, due to the interface jump conditions, it is challenging to define the approximate fluxes at the irregular points next to interfaces for satisfying mass conservation for the scheme across the interfaces. We propose novel corrected approximate fluxes from two sides of the interface (as "+" and "−") the irregular points next to interfaces by combining with the interface conditions at interfaces, which ensure the developed solution-flux scheme mass conservative while keeping accuracy. The resulting linear system of equations gives a sequence of tri-diagonal systems where the correction terms are approximated explicitly with given jump conditions.

We prove the proposed schemes to satisfy conservation of mass in the discrete form for 1D and 2D parabolic interface equations with multi-layers. Numerical experiments are given for both 1D problems and 2D problems to show mass conservation and convergence orders of our proposed schemes in time and space step sizes. We also compute the real applications of the diffusion process with large difference piecewise diffusion coefficients and the heat propagation in the multi-layer media. Numerical results show the excellent performance of our scheme. This work has been published in [44].

In the third part of thesis, we consider two dimensional flow system of interest which includes two flow models coupled of the surface flow and porous medium flow, and the interface conditions at the fluid-porous interface as well as boundary conditions. The main objective of this work is to develop an efficient and mass conservative numerical scheme in computation of coupled Stokes-Darcy flows with interface conditions in sharp interface including the Beaveres-Joseph-Saffman condition. Since velocities and pressures are primary variables in flows, the whole coupled Stokes-Darcy domain is partition into staggered meshes where free flow velocities, Darcy velocities and pressures in both regions are approximated within staggered grid framework [83].

Based on the projection techniques in free flow, and proposing the efficient treatment of interface conditions, we construct a time-splitting discretization scheme for the system. Further, applying the staggered finite difference operators, we develop a new conservative pressure-velocity scheme for the coupled free and porous media flow system. The important features of the developed scheme are that it is mass conservative and it is decoupled in computation. We theoretically prove that the scheme satisfies mass conservation over the whole domain of free flow and porous media flow. Two model problems for numerical experiments are first given to show mass conservation and the convergence of proposed algorithm in time and space sizes. Then, we solve by using our scheme two famous problems in fluid flow lid driven cavity and inflow-outflow to show mass conservation and the reliability of computation. Finally, we compute a realistic problem in inflow-outflow setting where porous media has two layers besides of the intersection of free flow and porous media flow. Numerical results show numerically our proposed scheme performs excellently.

Chapter 2

The long wave fluid flows on inclined porous media with nonlinear Forchheimer's law

2.1 Introduction

Long-wave fluid flows that appear on inclined planes have been studied in [10, 20, 41, 86, 91], since the pioneering experiment was done [47]. Efforts on stability of long-waves have been made for free flow with permeable substrate where Darcy's law was applied [42, 61, 81]. The Darcy's law is linear in the seepage velocity which describes the flow under the Reynolds number of the flow based on the a typical pore is smaller than order unity. As velocity in porous media increases, the problem becomes nonlinear and the flow in the pores is still laminar. Thus the flow regime exhibits nonlinear velocity affection described by Forchheimer's law [31, 39, 67, 72]. It is important to study such kind of flow system and to our best knowledge, there is no work on the surface flow coupled by nonlinear Forchheimer's porous media flow, where nonlinear Forchheimer's law describes the porous media flow through filtration substrates.

Therefore, in this chapter, we investigate long wave fluid flow down a porous incline where the porous media flow is described by Forchheimer's law. We consider a model of two-dimensional incompressible Newtonian fluid flow for free surface flows over inclined porous media with nonlinear flow of Forchheimer's law where no external force along the surface of a porous medium is taken. In Section 2.2, we set up the governing equation in a model of the filtration flow in the substrate by nonlinear Forchheimer's law and couple it to the surface flow by prescribing a variant of the Beavers-Joseph condition proposed by Jones [38]. In Section 2.3, we carry out an analysis of the long wave solution of the full systems by introducing the infinitesimal perturbations to study the long-wave solutions where they interact to equilibrium flows. Further, base state solutions are first derived out and the perturbed states for long wave solutions are further analyzed by corresponding Orr-Sommerfeld type equations. In Section 2.4, we propose to perform the approximation solution of Orr-Sommerfeld equations by a Chebyshev collocation method to analyze stability of long-wave in surface flow. In Section 2.5, we numerically study and analyze the influence of different flow parameters and porous media parameters on stability of long wave solutions, for which we will numerically analyze critical neutral stability curve, stable and unstable regions in the domain of Reynolds number and wavenumber. The conclusion of work is presented in Section 2.6.

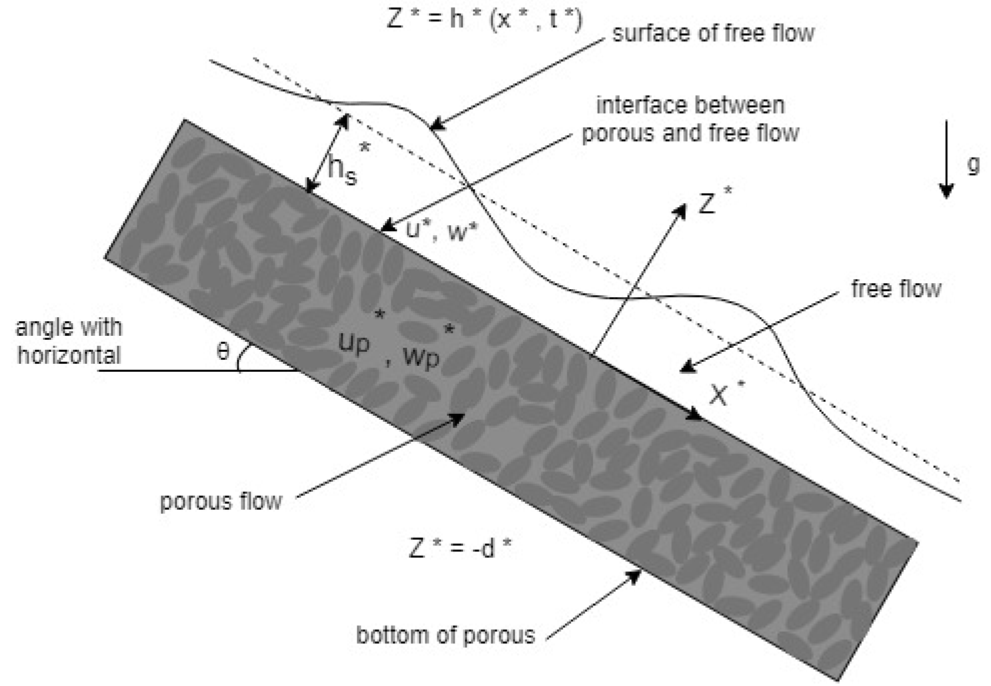

Figure 2.1: Graph of the problem.

2.2 Model of problem

Consider the two-dimensional incompressible Newtonian fluid flow with no external force along the surface of a porous medium substrate at an angle θ with horizontal, as shown in Fig. 2.1. The fluid has density ρ, viscosity μ and the surface tension γ and the porous medium has porosity ϕ and permeability κ, that are assumed to remain constants. We choose (x^*, z^*) as the coordinates respectively where the coordinate x^*-axis is parallel to the surface of the substrate while the z^*-axis is vertical to the surface of the substrate. Pressures and velocity components are denoted as p^*, u^*, w^* in clear flow and p_p^*, u_p^*, w_p^* in porous media flow. Therefore, a fully developed laminar flow is driven by gravitation, both in the fluid and the porous media.

The free surface flow over porous media substrate is coupled with porous media flow in substrate. We assume a fully saturated porous media flow in porous media slabs. The porosity ϕ of porous media in our study is between $0.01 - 0.6$ [67]. In the case, it is usually assumed that wetting fluid imbibing into liquid-coated porous media leads to a contact angle between $30^0 - 40^0$ where imbibing fluid will freely wet, and meanwhile, the liquid non-wetted with air leads to a contact angle between $130^0 - 150^0$ [90, 93].

2.2.1 Governing equations with Forchheimer's law

The equations of motion for the clear fluid flow in two dimensions in the inclined plane obtained from the conservation of mass and the conservation of momentum are given by the Navier-Stokes equations. The $x-$momentum equation is given by

$$\frac{\partial u^*}{\partial t^*} + u^* \frac{\partial u^*}{\partial x^*} + w^* \frac{\partial u^*}{\partial z^*} = -\frac{1}{\rho}\frac{\partial p^*}{\partial x^*} + \frac{\mu}{\rho}\left(\frac{\partial^2 u^*}{\partial x^{*2}} + \frac{\partial^2 u^*}{\partial z^{*2}}\right) + g\sin\theta, \tag{2.1}$$

while the $z-$ momentum equation is expressed as

$$\frac{\partial w^*}{\partial t^*} + u^* \frac{\partial w^*}{\partial x^*} + w^* \frac{\partial w^*}{\partial z^*} = -\frac{1}{\rho}\frac{\partial p^*}{\partial z^*} + \frac{\mu}{\rho}\left(\frac{\partial^2 w^*}{\partial x^{*2}} + \frac{\partial^2 w^*}{\partial z^{*2}}\right) - g\cos\theta, \tag{2.2}$$

where p^* is pressure, g is acceleration due to gravity, ρ is density of the fluid, and μ is viscosity. The continuity equation can be written as

$$\frac{\partial u^*}{\partial x^*} + \frac{\partial w^*}{\partial z^*} \;=\; 0. \tag{2.3}$$

The porous media flow in the substrate is described by nonlinear Forchheimer law

[31]. As the inertial effects start dominating the flow, it suggests the inclusion of an inertial nonlinear term of kinematic energy of the fluid to Darcy equation [67]. The inertial term is expressed as $\lambda\rho\left|\mathbf{u}_{\mathbf{p}}^{*}\right|\mathbf{u}_{\mathbf{p}}^{*}$, and the parameter λ is obtained by Ergun [28] in experiments given as

$$\lambda = \frac{c_F}{\sqrt{\kappa}},$$

where κ denotes its permeability, and c_F dimensionless drag constant (Ergun constant). Values of permeability κ for natural materials vary widely. For examples, typical values, in terms of the unit m^2, are $10^{-7} - 10^{-9}$ for clean gravel, $10^{-9} - 10^{-12}$ for clean sand, $10^{-11} - 10^{-13}$ for peat and $10^{-16} - 10^{-20}$ for unweathered clay [67]. The drag constant c_F might be a constant with a value of approximately 0.55 but later it was found to be varied with the nature of the porous medium grain's shape and size and can be as small as 0.1 ([67, 72]).

For the flow in porous media referred to Forchheimer's law, the equations can be expressed as

$$\frac{\rho}{\phi}\frac{\partial u_p^*}{\partial t^*} = -\frac{\partial p_p^*}{\partial x^*} - \frac{\mu}{\kappa}u_p^* - \frac{c_F}{\sqrt{\kappa}}\rho u_p^*\sqrt{u_p^{*2} + w_p^{*2}} + g\rho\sin\theta, \tag{2.4}$$

$$\frac{\rho}{\phi}\frac{\partial w_p^*}{\partial t^*} = -\frac{\partial p_p^*}{\partial z^*} - \frac{\mu}{\kappa}w_p^* - \frac{c_F}{\sqrt{\kappa}}\rho w_p^*\sqrt{u_p^{*2} + w_p^{*2}} - g\rho\cos\theta, \tag{2.5}$$

where p_p^* is the intrinsic volume averaged pressure, ϕ is porosity of the porous medium. For a natural porous medium, porosity ϕ does not normally exceed 0.6 but smaller, i.e, we consider ϕ is between $0.01 - 0.6$ ([67]).

The continuity equation of the flow in the porous media is given by

$$\frac{\partial u_p^*}{\partial x^*} + \frac{\partial w_p^*}{\partial z^*} = 0. \tag{2.6}$$

Conditions at the free surface of fluid are obtained from the continuity of force and conservation of mass. The total stress tensor associated with the flow is given by $\mathcal{S} = -p^*\mathcal{I} + \tau$ and stress vector acting on surface $z^* = h^*(x^*, t^*)$ is then $\mathcal{S}\widehat{n}$, where $\widehat{n}$ is the unit normal vector. The normal force exerted by the flow on the surface is balanced by surface tension. This is expressed mathematically as $(\mathcal{S}\widehat{n}) \cdot \widehat{n} = \gamma\mathcal{C}$, where γ is the surface tension coefficient and $\mathcal{C}$ measures the mean curvature of the surface. So, we have

$$-p^* + \frac{2\mu}{1+\left(\frac{\partial h^*}{\partial x^*}\right)^2}\left[\left(\frac{\partial h^*}{\partial x^*}\right)^2 \frac{\partial u^*}{\partial x^*} + \frac{\partial w^*}{\partial z^*} - \frac{\partial h^*}{\partial x^*}\left(\frac{\partial u^*}{\partial z^*} + \frac{\partial w^*}{\partial x^*}\right)\right] = \frac{\gamma \frac{\partial^2 h^*}{\partial x^{*2}}}{\left(1+\left(\frac{\partial h^*}{\partial x^*}\right)^2\right)^{\frac{3}{2}}}, \quad \text{at} \quad z^* = h^*. \tag{2.7}$$

With the assumption that the surface tension is constant, the tangential component of the force exerted by the flow on the surface must equal zero, and then we have $(\mathcal{S}\widehat{n})\cdot\widehat{t} = 0$, where $\widehat{t}$ is the unit tangent vector along the surface. It follows that

$$\frac{\mu}{1+\left(\frac{\partial h^*}{\partial x^*}\right)^2}\left[-4\frac{\partial h^*}{\partial x^*}\frac{\partial u^*}{\partial x^*} + \left(1-\left(\frac{\partial h^*}{\partial x^*}\right)^2\right)\left(\frac{\partial u^*}{\partial z^*} + \frac{\partial w^*}{\partial x^*}\right)\right] = 0, \quad \text{at} \quad z^* = h^*. \tag{2.8}$$

We assume the effect of evaporation is negligible, and then there is no flux source of matters into the surface of free flow. Let interface curve be $z^* = h^*(x^*, t^*)$, which is a material line. Thus, the cross-stream component of the fluid velocity at surface must equal to the material derivative of the height function of the surface, which is expressed under evaporation is negligible [32, 49] as

$$\frac{Dh^*}{Dt^*} \equiv \frac{\partial h^*}{\partial t^*} + \frac{\partial h^*}{\partial x^*} u^* = w^*, \quad \text{at} \quad z^* = h^*, \tag{2.9}$$

where equation (2.9) is known as kinematic condition at $z^* = h^*(x^*, t^*)$.

Noting that the stress acting on the interface of fluid-porous medium at $z^* = 0$ is σ_{22} in the $z-$direction, the continuity of normal stress is expressed as

$$-p^* + 2\mu \frac{\partial w^*}{\partial z^*} = -p_p^* + 2\mu \frac{\partial w_p^*}{\partial z^*}, \quad \text{at} \quad z^* = 0, \tag{2.10}$$

and the continuity of cross-stream velocity gives that

$$w^* = w_p^*, \quad \text{at} \quad z^* = 0. \tag{2.11}$$

The slip-velocity condition at a fluid-porous medium interface originally proposed by Beavers and Joseph [8] stipulates a proportionality between velocity shear and difference of surface flow velocity and filtration velocity at interface. For our problem, we will employ the modified version proposed by Jones [38], which replaces velocity shear by shear stress, expressed by

$$\frac{\partial u^*}{\partial z^*}+\frac{\partial w^*}{\partial x^*}=\frac{\alpha_{BJ}}{\sqrt{\kappa}}\left(u^*-u_p^*\right), \quad \text{at} \quad z^*=0, \tag{2.12}$$

where α_{BJ} is Beaver-Joseph parameter, i.e. an empirical quantity which depends on the pore-space geometry of the porous medium. The experimental study by Beaver and Joseph [8] indicates that the parameter α_{BJ} is positive real number values upto 4.0.

At the bottom of the porous medium substrate, we assume it impermeable and consequently appropriate boundary condition,

$$w_p^*=0, \quad \text{at} \quad z^*=-d^*, \tag{2.13}$$

where $d^*>0$ is the thickness of the porous medium substrate.

2.2.2 Dimensionless equations

The solution of our model depends on the fluid properties, inclination and permeability of porous medium as well as the relation between the discharge and cross-stream height of clear flow. We derive out dimensionless equations. We let the dimensionless discharge quantity Q be prescribed, cross-stream height by employing the Nusselt thickness H which satisfies $H=\left(\frac{3\mu Q}{\rho g\sin\theta}\right)^{1/3}$, and describes the scale of thickness of uniform surface flow over the porous substrate. Let U and L denote the stream-wise velocity component and the length scale of the flow respectively. Scaled cross-stream velocity component and pressure in surface fluid flow are δU and ρU^2 respectively; where $\delta = \frac{H}{L}$ is the ratio of cross-stream hight scale to stream-wise length scale and δ is considered to be very small, denoted as the small parameter. Meanwhile, the time scale is $\frac{H}{U}$.

Therefore, we have dimensionless equations of the surface flow

$$\frac{\partial u}{\partial x} + \frac{\partial w}{\partial z} = 0, \tag{2.14}$$

$$\delta R_e \frac{Du}{Dt} = -\delta R_e \frac{\partial p}{\partial x} + \delta^2 \frac{\partial^2 u}{\partial x^2} + \frac{\partial^2 u}{\partial z^2} + 3, \tag{2.15}$$

$$\delta^2 R_e \frac{Dw}{Dt} = -R_e \frac{\partial p}{\partial z} + \delta^3 \frac{\partial^2 w}{\partial x^2} + \delta \frac{\partial^2 w}{\partial z^2} - 3\cot\theta, \tag{2.16}$$

where p is pressure, (u, w) is velocity of surface flow, $\frac{D}{Dt}$ denotes the two-dimensional material derivative and the Reynolds number is defined as $R_e = \frac{\rho Q}{\mu}$. We will focus on the study of the long wave solutions of laminar surface flows over inclined porous media substrates where the inclined angle θ of the porous media substrates is from $30^o - 70^o$. The obtained critical stability curves and the stable regions of the long wave solutions of surface flows fall in the range of Reynolds number R_e from 0.8 to 3.2, where the flows are laminar. See, numerical results in Section 2.5.

At the free surface, $z = h(x, t)$, they satisfy

$$\begin{aligned} p \;=\; & \frac{2\delta}{R_e\left[1+\delta^2\left(\frac{\partial h}{\partial x}\right)^2\right]}\left[\delta^2\left(\frac{\partial h}{\partial x}\right)^2\frac{\partial u}{\partial x}+\frac{\partial w}{\partial z}-\frac{\partial h}{\partial x}\frac{\partial u}{\partial z}-\delta^2\frac{\partial h}{\partial x}\frac{\partial w}{\partial x}\right] \\ & -\frac{\delta^2 W_e}{\left[1+\delta^2\left(\frac{\partial h}{\partial x}\right)^2\right]^{3/2}}\frac{\partial^2 h}{\partial x^2}, \end{aligned} \tag{2.17}$$

$$\left[1-\delta^2\left(\frac{\partial h}{\partial x}\right)^2\right]\left(\frac{\partial u}{\partial z}+\delta^2\frac{\partial w}{\partial x}\right)-4\delta^2\frac{\partial h}{\partial x}\frac{\partial u}{\partial x}=0, \tag{2.18}$$

and

$$\frac{\partial h}{\partial t}+u\frac{\partial h}{\partial x}=w, \tag{2.19}$$

where $W_e=\left(\frac{3}{Re^5\sin\theta}\right)^{1/3}K_a$ is the Weber number, and K_a denotes the Kapitza number which is a scaled surface tension given by $K_a=\gamma/(g^{1/3}\rho\nu^{4/3})$, with γ being the surface tension and ν being the kinematic viscosity.

In porous medium, the stream-wise velocity scale U_p can be expressed as scale $\dfrac{\kappa\rho g\sin\theta}{3\mu}$, and pressure P_p is scaled in $\dfrac{\rho U^2}{R_e\delta}$. By scaling, we have dimensionless equations of the porous media flow

$$\frac{\partial u_p}{\partial x}+\frac{\partial w_p}{\partial z}=0, \tag{2.20}$$

$$\frac{D_a^2R_e\delta}{\phi}\frac{\partial u_p}{\partial t}=-\frac{\partial p_p}{\partial x}-u_p-c_FD_a^3R_eu_p\sqrt{u_p^2+\delta^2w_p^2}+3, \tag{2.21}$$

and

$$\frac{D_a^2R_e\delta^3}{\phi}\frac{\partial w_p}{\partial t}=-\frac{\partial p_p}{\partial z}-\delta^2w_p-\delta^2c_FD_a^3R_ew_p\sqrt{u_p^2+\delta^2w_p^2}-3\delta\cot\theta, \tag{2.22}$$

where $D_a=\frac{\sqrt{\kappa}}{H}$ is Darcy number and c_F is drag constant (Ergun constant), which measure the permeability of the porous medium to fluid filtration.

At the interface of surface flow and the porous media, $z = 0$, it hols that

$$\begin{aligned} \delta R_e p - 2\delta^2 \frac{\partial w}{\partial z} &= p_p - 2D_a^2 \delta^2 \frac{\partial w_p}{\partial z}, && (2.23) \\ w &= D_a^2 w_p, && (2.24) \\ \frac{\partial u}{\partial z} + \delta^2 \frac{\partial w}{\partial x} &= \frac{\alpha_{BJ}}{D_a}(u - D_a^2 u_p), && (2.25) \end{aligned}$$

At the bottom of the porous medium substrate, $z = -d$, it satisfies

$$w_p = 0 \tag{2.26}$$

where $d = d^*/H$ is scaled thickness of porous medium by characteristic thickness H of clear fluid film.

2.3 Analysis of the long-wave solution

2.3.1 Base state solution

We first find stationary and uniform flow solutions in the inclination direction, which are denoted as $h = h_s, u = u_s(z), u_p = u_{p,s}, p = p_s(z)$, $p_p = p_{p,s}(z)$ and $w = w_s, w_p = w_{p,s}$. It is clear that $w_s = 0, w_{p,s} = 0$. The equilibrium velocities $u_s(z)$ in surface flow and $u_{p,s}$ in porous media can be obtained from equations of (2.14)-(2.26) as

$$u_p = u_{p,s} = \frac{-1 + \sqrt{1 + 12\beta}}{2\beta}, \tag{2.27}$$

where $\beta = c_F D_a^3 R_e$, and

$$u = u_s(z) = 3h_s z - \frac{3}{2}z^2 + 3\frac{D_a}{\alpha_{BJ}}h_s + u_{ps}D_a^2, \tag{2.28}$$

where the above expression recovers the familiar parabolic profile of the free flow.

The equilibrium pressures, $p_s(z)$ and $p_{p_s}(z)$, can be obtained as

$$p = p_s(z) = 3\frac{\cot\theta}{R_e}(h_s - z), \tag{2.29}$$

and

$$p_p = p_{p,s}(z) = 3\delta\cot\theta(h_s - z), \tag{2.30}$$

Finally, we derive out the equilibrium thickness h_s of the free flow. We prescribe discharge as a unit, i.e. $Q = 1$, then we have

$$Q = \int_0^{h_s} u_s(z)dz, \tag{2.31}$$

further from (2.28) and (2.31) we get that

$$h_s = \frac{1}{6r^{1/3}\alpha_{BJ}}(r^{2/3} - 12u_{ps}D_a^2\alpha_{BJ}^2 + 36D_a^2 - 6D_a r^{1/3}), \tag{2.32}$$

where the constant r is $r = 108\,u_{p,s}{D_a}^3{\alpha_{BJ}}^2 + 108\,\alpha_{BJ}^3 - 216\,{D_a}^3 + 12\sqrt{3}\,{\alpha_{BJ}}^{3/2}r_0^{\frac{1}{2}}$ with $r_0 = [4\,{D_a}^6\alpha_{BJ}^3u_{p,s}^3 - 9\,{D_a}^6\alpha_{BJ}u_{p,s}^2 + 54\,{D_a}^3{\alpha_{BJ}}^2u_{p,s} + 27\,{\alpha_{BJ}}^3 - 108\,{D_a}^3]$.

Thus, we have the base state solution of $h = h_s, u = u_s(z), u_p = u_{p,s}, p = p_s(z)$,

$p_p = p_{p,s}(z)$ and $w = 0, w_p = 0$ given by (2.27), (2.28), (2.29), (2.30), (2.32).

2.3.2 Perturbated state for the long wave solution

We study the long wave solutions of perturbed to the equilibrium flows. We impose perturbations under δ (the ratio of cross-stream hight scale to stream-wise length scale) being very small. Denoting perturbation unknown variables by tildes, we have that

$$
\begin{aligned}
&h = h_s + \eta(x,t), \quad u = u_s(z) + \tilde{u}(x,z,t), \quad w = \tilde{w}(x,z,t), \\
&p = p_s(z) + \tilde{p}(x,z,t), \quad p_p = p_{p,s}(z) + \tilde{p_p}(x,z,t), \\
&u_p = u_{p,s} + \tilde{u_p}(x,z,t), \quad \text{and} \quad w_p = \tilde{w_p}(x,z,t),
\end{aligned}
$$

where $\eta, \tilde{u}, \tilde{w}, \tilde{p}, \tilde{p_p}, \tilde{u_p}, \tilde{w_p}$ are called the perturbation solutions, which are very small.

Eliminating the quadratic nonlinear terms of perturbation unknown variables, the linearized perturbation equations can be written in the forms as

$$
\frac{\partial \tilde{u}}{\partial x} + \frac{\partial \tilde{w}}{\partial z} = 0, \tag{2.33}
$$

$$
\delta R_e \left(\frac{\partial \tilde{u}}{\partial t} + u_s \frac{\partial \tilde{u}}{\partial x} + \tilde{w} \frac{\partial u_s}{\partial z} \right) = -\delta R_e \frac{\partial \tilde{p}}{\partial x} + \delta^2 \frac{\partial^2 \tilde{u}}{\partial x^2} + \frac{\partial^2 \tilde{u}}{\partial z^2}, \tag{2.34}
$$

$$
\delta^2 R_e \left(\frac{\partial \tilde{w}}{\partial t} + u_s \frac{\partial \tilde{w}}{\partial x} \right) = -R_e \frac{\partial \tilde{p}}{\partial z} + \delta^3 \frac{\partial^2 \tilde{w}}{\partial x^2} + \delta \frac{\partial^2 \tilde{w}}{\partial z^2}, \tag{2.35}
$$

and

$$
\frac{\partial \tilde{u_p}}{\partial x} + \frac{\partial \tilde{w_p}}{\partial z} = 0, \tag{2.36}
$$

$$\frac{D_a^2 R_e \delta}{\phi} \frac{\partial \tilde{u_p}}{\partial t} = -\frac{\partial \tilde{p_p}}{\partial x} - \tilde{u_p} - 2\beta u_{p,s} \tilde{u_p}, \tag{2.37}$$

$$\frac{D_a^2 R_e \delta^3}{\phi} \frac{\partial \tilde{w_p}}{\partial t} = -\frac{\partial \tilde{p_p}}{\partial z} - \delta^2 \tilde{w_p} - \delta^2 \beta u_{p,s} \tilde{w_p}, \tag{2.38}$$

with

$$\tilde{p} - \frac{3}{R_e} \cot\theta \eta - \frac{2\delta}{R_e} \frac{\partial \tilde{w}}{\partial z} + \delta^2 W_e \frac{\partial^2 \eta}{\partial x^2} = 0, \quad \text{at} \quad z = h_s, \tag{2.39}$$

$$-3\eta + \frac{\partial \tilde{u}}{\partial z} + \delta^2 \frac{\partial \tilde{w}}{\partial x} = 0, \quad \text{at} \quad z = h_s, \tag{2.40}$$

$$\frac{\partial \eta}{\partial t} + u_s \frac{\partial \eta}{\partial x} = \tilde{w}, \quad \text{at} \quad z = h_s, \tag{2.41}$$

and

$$\delta R_e \tilde{p} - 2\delta^2 \frac{\partial \tilde{w}}{\partial z} = \tilde{p_p} - 2D_a^2 \delta^2 \frac{\partial \tilde{w_p}}{\partial z}, \quad \text{at} \quad z = 0, \tag{2.42}$$

$$\frac{\partial \tilde{u}}{\partial z} + \delta^2 \frac{\partial \tilde{w}}{\partial x} = \frac{\alpha_{BJ}}{D_a} \left(\tilde{u} - D_a^2 \tilde{u_p} \right), \quad \text{at} \quad z = 0, \tag{2.43}$$

$$\tilde{w} = D_a^2 \tilde{w_p}, \quad \text{at} \quad z = 0, \tag{2.44}$$

$$\tilde{w_p} = 0, \quad \text{at} \quad z = -d. \tag{2.45}$$

The linear stability analysis consists of presuming and analyzing the existences of sinusoidal disturbances to base state solution. The velocity field of a base state flow moves constant along x-axis with a speed and varies along z-axis.

We impose a spatially extended disturbances of long wave solution form (called as the normal mode form) as

$$(\tilde{u}, \tilde{w}, \tilde{p}, \eta) = (\hat{u}(z), \hat{w}(z), \hat{p}(z), \hat{\eta})\, e^{ik(x-ct)},$$

$$(\tilde{u_p}, \tilde{w_p}, \tilde{p_p}) = (\hat{u_p}(z), \hat{w_p}(z), \hat{p_p}(z))\, e^{ik(x-ct)},$$

where $\hat{u}(z), \hat{w}(z), \hat{p}(z), \hat{u_p}(z), \hat{w_p}(z), \hat{p_p}(z)$ are z- dependent amplitudes of perturbations, k is a real positive quantity representing the wavenumber of the perturbations, and c is a complex quantity whose real part is the phase speed of the perturbations while the imaginary part multiplied by k is temporal growth rate. The pressure distribution on the surface of free flow is hydrostatic for long wave flows. However, the pressure disturbance $\tilde{p}$ and $\tilde{p_p}$ can be eliminated from linearized perturbation equations, and the z-dependent velocity disturbance can be written from stream function given by

$$\hat{u} = \frac{\partial \psi}{\partial z},\ \hat{w} = -\frac{\partial \psi}{\partial x},\ \hat{u_p} = \frac{\partial \psi_p}{\partial z},\ \hat{w_p} = -\frac{\partial \psi_p}{\partial x}.$$

Further, we introduce the normal modes for stream functions of wave solutions expressed as

$$(\psi, \psi_p) = (\Psi(z), \Psi_p(z))\, e^{ik(x-ct)}.$$

Using the normal mode of stream functions in equations (2.33)-(2.45), it leads the following Orr-Sommerfeld type equations of stream functions $\{\Psi(z), \Psi_p(z)\}$ as

$$D^4\Psi - \left[iKR_e(u_s - c) + 2K^2\right] D^2\Psi + \left[iK^3R_e(u_s - c) + iKR_eD^2u_s + K^4\right]\Psi = 0, \quad (2.46)$$

$$\left(1 + 2\beta u_{p,s} - iKc\frac{ReD_a^2}{\phi}\right) D^2\Psi_p - K^2\left(1 + \beta u_{p,s} - iKc\frac{ReD_a^2}{\phi}\right)\Psi_p = 0, \quad (2.47)$$

where $K = k\delta$ and $D = \frac{\partial}{\partial z}$, and the boundary conditions at $z = h_s$ are

$$D^3\Psi - \left[iKR_e(u_s - c) + 3K^2\right] D\Psi + \frac{3iK\,\cot\theta + iK^3R_eW_e}{u_s - c}\Psi = 0\,, \tag{2.48}$$

$$D^2\Psi + \frac{3\Psi}{u_s - c} + K^2\Psi = 0\,, \tag{2.49}$$

and the boundary conditions at $z = 0$ are

$$D^3\Psi - \left[iKR_e(u_s - c) + 3K^2\right] D\Psi + iKR_eDu_s\Psi = \left(\frac{icKD_a^2R_e}{\phi} - 1 - 2\beta u_{p,s} - 2K^2D_a^2\right) D\Psi_p \tag{2.50}$$

$$D\Psi - D_a^2D\Psi_p = \frac{D_a}{\alpha_{BJ}}(D^2\Psi + K^2\Psi)\,, \tag{2.51}$$

$$\Psi = D_a^2\Psi_p\,, \tag{2.52}$$

and at $z = -d$,

$$\Psi_p = 0\,. \tag{2.53}$$

We solve equation (2.47) using the boundary conditions (2.52), (2.53). We thus obtain that at the interface $z = 0$

$$D\Psi_p = \frac{\sqrt{d_1 - ec}}{D_a^2}\coth\left(\sqrt{(d_1 - ec)}d\right)\Psi\,, \tag{2.54}$$

where $a = \beta u_{ps}$, $d_1 = \dfrac{K^2(1 + 3a + 2a^2)}{(1 + 2a)^2}$, $e = \dfrac{aR_1K^2}{(1 + 2a)^2}$, and $R_1 = \dfrac{R_eD_a^2iK}{\phi}$.

We can eliminate Ψ_p from the equations (2.50), (2.51) by substituting the value of

$D\Psi_p$ from (2.54). Then, we obtain that

$$\begin{aligned} & D^3\Psi - \left[iKR_e(u_s - c) + 3K^2\right] D\Psi + iKR_e Du_s\Psi \\ & = \left(\frac{icKD_a^2R_e}{\phi} - 1 - 2\beta u_{p,s} - 2K^2D_a^2\right) \frac{\sqrt{(d_1 - ec)}}{D_a^2} \coth\left(\sqrt{(d_1 - ec)}d\right)\Psi, \end{aligned} \tag{2.55}$$

and

$$D\Psi - \sqrt{(d_1 - ec)} \coth\left(\sqrt{(d_1 - ec)}d\right)\Psi = \frac{D_a}{\alpha_{BJ}}(D^2\Psi + K^2\Psi). \tag{2.56}$$

In order to carry out the stability analysis of long-wave solution for a given set of parameters (R_e, K_a, D_a, ϕ, α_{BJ}, d, $\cot\theta$, c_F), we need to determine the growth rate of a particular perturbation distinguished by its wavenumber. More specifically, we need to analyze the corresponding value of c. If $\Im(c)$ is negative, the perturbation is damped, while if $\Im(c)$ is positive, the perturbation is amplified. Thus, in dealing with the system given by equations (2.46), (2.48), (2.49), (2.55) and (2.56), c is also an unknown parameter. We will determine c by requiring that nontrivial solutions exist for Ψ. Therefore, equations (2.46), (2.48), (2.49), (2.55) and (2.56) comprise an eigenvalue problem of c to which the characteristic values are required to analyze, which leads to the analysis to an eigenvalue PDE problem.

Remark 1. The stream-wise direction velocities of our basic steady state solutions, $u = u_s(z)$ and $u_p = u_{p,s}$, are given by equations (2.27) and (2.28) in porous media flow and free surface flow respectively under the influence of gravity and porous media, the speed $u = u_s(z)$ in the surface flow varies in the z-direction vertical to the surface of the porous media substrate which recovers the parabolic profile of free flow, while the speed $u_p = u_{p,s}$ is constant in substrate, where cross-stream velocities remain zero ($w_s = 0$ and $w_{p,s} = 0$). The thickness of the fluid is assumed to vary in space and time. The wave number of fluid wave on the surface of flow is inversely proportional to its wave length. We consider long wave perturbation solutions $\tilde{u}(x, z, t)$, $\tilde{w}(x, z, t)$ and $\tilde{u}_p(x, z, t)$, $\tilde{w}_p(x, z, t)$ to base steady solution. The long wave solutions are keeping the same shape traveling in the $k(x - ct)$ plane with small wavenumber k and wave speed kc. Over the time, the flows can be perturbed with very small perturbations in z-direction and travel in the direction of with small wavenumber k, where on the surface of the free flow, it can be seen as damped or amplified in z-direction, i.e. a long wave flow. In fact, we take $K = k\delta$ where k is the wavenumber and δ is the small parameter of the length scale ratio. It points out that $2\pi/K$ is the wavelength of the perturbations scaled with characteristic fluid thickness H which is large traveling wave of fluid on the surface provided that the value of K is small.

Remark 2. In this study, we analyze the long wave solutions of free surface flows over inclined porous media substrates, which is subject to an active area of research because of its inertial stability that appears in the interfacial waves and in many applications in [6, 11, 13, 21, 34, 67, 70, 79, 93]. When considering non-Newtonain fluid flows, due to strong nonlinear terms modelled by power-law, it is likely to occur roll waves, nonlinear turbulence waves or discontinuous waves for non-Newtonain fluid flows. See, for examples, [6, 69].

2.4 Numerical method of long-wave stability

In this section, we analyze numerically the long-wave stability of surface flow described in Section 2.3. We will use Chebyshev's numerical method to approximate the solution of Orr-Sommerfeld equations due to its high accuracy. Chebysyhev approximation produces a nearly optimal approximation coming close to minimizing the absolute error and the approximation can be computed more easily. Chebyshev method also admits a fast efficient implementation and efficient way to solve for a smooth non-periodic function and it can handles the boundaries condition properly [12]. In more details, to calculate eigenvalues for the problem of (2.46), (2.48), (2.49), (2.55) and (2.56), we propose to use a Chebyshev collocation method [12] to solve the problem.

We first transform the domain $z \in (0, h_s)$ to $\xi \in (-1, 1)$ by employing the transformation of

$$\xi = \frac{2}{h_s} z - 1.$$

Letting $\Phi(\xi) = \Psi(z)$ and $D = \frac{\partial}{\partial z} = \frac{\partial}{\partial \xi}$, the derivatives then become $D\Psi(z) = \frac{2}{h_s}\Phi(\xi)$, $D^2\Psi(z) = (\frac{2}{h_s})^2 D^2\Phi(\xi)$, $D^3\Psi(z) = (\frac{2}{h_s})^3 D^3\Phi(\xi)$ and $D^4\Psi(z) = (\frac{2}{h_s})^4 D^4\Phi(\xi)$. Let Chebyshev polynomial set $\{T_{j-1}(\xi) = \cos((j-1)\arccos\xi), j = 1, 2, \cdots, N\}$, we thus expand an unknown function $\Phi(\xi)$ in terms of Chebyshev polynomials as

$$\Phi(\xi) = \sum_{j=1}^{N} a_j T_{j-1}(\xi),$$

where $a_1, a_2, \cdots, a_N$ are unknown coefficients.

Consequently, the PDE problem of (2.46), (2.48), (2.49), (2.55) and (2.56) reduces to

$$\sum_{j=1}^{N} a_j\Big(\frac{16}{h_s^4}D^4T_{j-1}(\xi) \quad - \quad \frac{4}{h_s^2}\left[iKR_e(u_s-c)+2K^2\right]D^2T_{j-1}(\xi) \\ + \quad \left[iK^3R_e(u_s-c)+iKR_eD^2u_s+K^4\right]T_{j-1}(\xi)\Big) = 0, \tag{2.57}$$

and boundary conditions are that at $\xi = 1$

$$\sum_{j=1}^{N} a_j\left(\frac{8}{h_s^3}D^3T_{j-1}(1) - \left[iKR_e(u_s-c)+3K^2\right]DT_{j-1}(1) + \frac{3iK\cot\theta + iK^3R_eW_e}{u_s-c}T_{j-1}(1)\right) = 0\,, \tag{2.58}$$

$$\sum_{j=1}^{N} a_j\left(\frac{4}{h_s^2}D^2T_{j-1}(1) + \frac{3\Phi}{u_s-c} + K^2T_{j-1}(1)\right) = 0\,, \tag{2.59}$$

and at $\xi = -1$

$$\sum_{j=1}^{N} a_j\left(\frac{8}{h_s^3}D^3T_{j-1}(-1) - \frac{2}{h_s}\left[iKR_e(u_s-c)+3K^2\right]DT_{j-1}(-1) + iKR_eDu_sT_{j-1}(-1)\right) \\ = \sum_{j=1}^{N} a_j\left(\left(\frac{icKD_a^2R_e}{\phi} - 1 - 2\beta u_{p,s} - 2K^2D_a^2\right)\frac{\sqrt{(d_1-ec)}}{D_a^2}\coth\left(\sqrt{(d_1-ec)}d\right)T_{j-1}(-1)\right) \tag{2.60}$$

and

$$\textstyle\sum_{j=1}^{N} a_j\left(\frac{2}{h_s}DT_{j-1}(-1) - \sqrt{(d_1-ec)}\coth\left(\sqrt{(d_1-ec)}d\right)T_{j-1}(-1)\right) \\ \textstyle = \sum_{j=1}^{N} a_j\left(\frac{D_a}{\alpha_{BJ}}\left(\frac{4}{h_s^2}D^2T_{j-1}(-1) + K^2T_{j-1}(-1)\right)\right). \tag{2.61}$$

Further we evaluate above equations (2.57) at interior grid points of $[-1,1]$ by using grid points

$$\xi_i = \cos\left(\frac{i\pi}{N-4}\right), \qquad i = 1, 2, \cdots, N-5.$$

This yields to an $N \times N$ algebraic system of coefficient vector $\vec{a} = (a_1, a_2, \ldots, a_N)^\tau$, which can be expressed in the matrix form

$$\mathbf{L}\vec{a} = c\mathbf{M}\vec{a}, \tag{2.62}$$

where $\mathbf{L}$ and $\mathbf{M}$ are $N \times N$ matrices and c remains as parameter. Eigenvalues of parameter c can be numerically solved by Matlab code. In the method, solving the algebraic eigenvalue system of (2.62) gives N eigenvalue values of c. However, the system should have a single value. To fix this issue, we calculate the eigenvalues of algebraic system for different values of N and find that for sufficiently large values, as N is increased, only one eigenvalue remains approximately constant. We select eigenvalue as appropriate solution for c.

2.5 Numerical results

We numerically study the influence of different flow parameters and porous media parameters on stability of long wave solutions, for which we will numerically analyze critical neutral stability curve, stable and unstable regions in the domain of Reynolds number R_e and wavenumber K. The study focus on important parameters such as

Drag value of flow in porous media, porosity of porous material, permeability of fluid flow inside the porous medium, porous material structure at the fluid-porous interface, and slop steepness. Our study is for the surface flow coupled by porous media flow of Newtonian fluid like pure water. To get the results from the given set of parameters, we simulate over a wavenumber and compute numerically the temporal growth rate. The resulting graphs are marginal (neutral) stability curves in $R_e - K$ plane, which indicate relationship of the wavenumber with zero growth rate with the Reynolds number. The curve divides the $R_e - K$ plane into stable and unstable regions corresponding to damped or amplified infinitesimal perturbations. The onset of stability for the long wave flows corresponds to the critical Reynolds number curve $R_e = R_{e,crit}(K)$, such that for smaller R_e values than the $R_{e,crit}$, the wavenumbers have a non-positive growth rate and the long wave flows are stable, while for larger R_e values than $R_{e,crit}$, there are wavenumbers with a positive growth rate indicating the long wave flows as unstable.

In Fig. 2.2, we first present the marginal stability curve of our model with nonlinear Forchheimer's law with very small drag constant c_F and compare it to the one of model with Darcy's law [42]. We observe that it is in an excellent agreement for smaller drag constant $c_F = 10^{-7}$. Thus, it shows that the Forchheimer's law with very small c_F corresponds to Darcy's law in porous medium. Our results of $R_{e,crit}$ for very small K in neutral stability curves are validated by analytical analyzed in [91]. It also confirms that the marginal stability curves of our nonlinear Forchheimer's law model is consistent- for very small drag constant c_F- to the one modelling with Darcy's law [42].

The drag constant c_F in nonlinear Forchheimer's law is a major influencing parameter

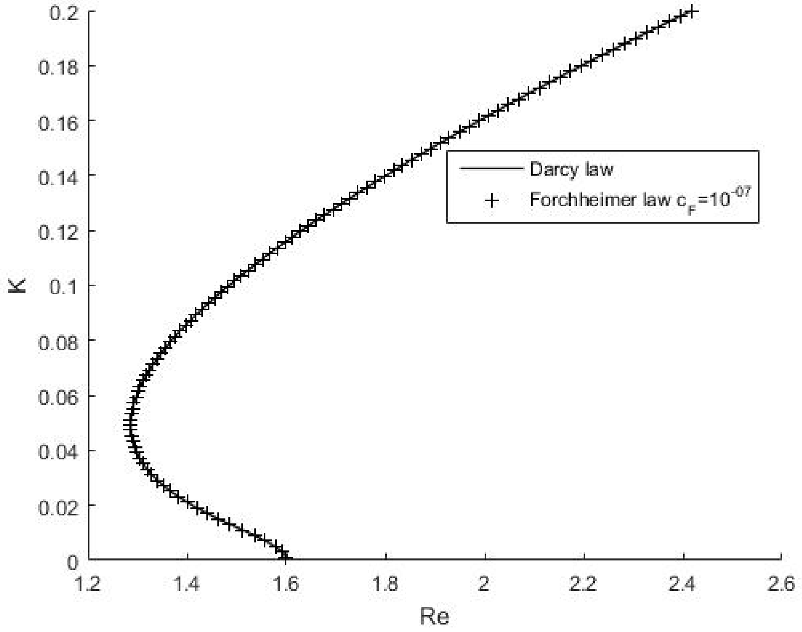

Figure 2.2: Comparison between the Forchheimer's law (with $c_F = 10^{-7}$) and Darcy law with $\cot\theta = 1, d = 1, \phi = 0.01, \alpha_{BJ} = 2, D_a = 0.3, K_a = 100$.

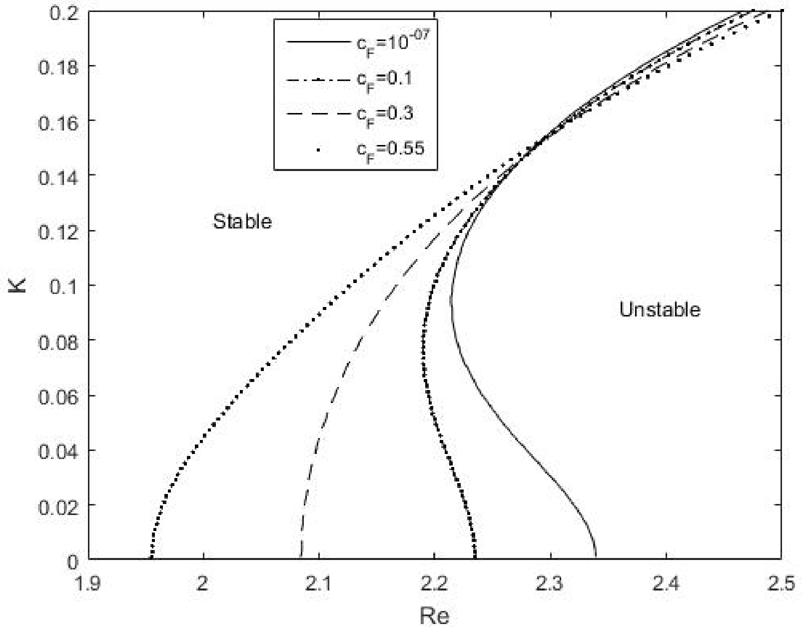

Figure 2.3: Effect of stability of long wave flows for different drag constant c_F with $\cot\theta = 1, d = 3, \phi = 0.1, \alpha_{BJ} = 1, D_a = 0.35, K_a = 100$.

in the stability of the long-wave solutions of free flows. To characterize the effects of the drag constant, we fix parameters $\cot\theta = 1, d = 3, \phi = 0.1, \alpha_{BJ} = 1, D_a = 0.35, K_a = 100$. Fig. 2.3 presents the marginal stability curves for various drag constant c_F; it can be clearly seen that with larger c_F, the long wave flow is more unstable than with smaller c_F. Letting $R_{e,0}$ be the intercept value of marginal curve $R_e = R_{e,crit}$ with R_e-axis where wavenumber value is as small as $K \to 0$, we interestingly notice that, for very small c_F, value $R_{e,crit}$ is smaller than $R_{e,0}$, i.e. as c_F increases, the difference between $R_{e,crit}$ and $R_{e,0}$ decreases. The critical stability curves $R_e = R_{e,crit}$ and the stable regions of long wave solutions of surface flows are obtained accurately by model of nonlinear Forchheimer's law with various drag constant c_F.

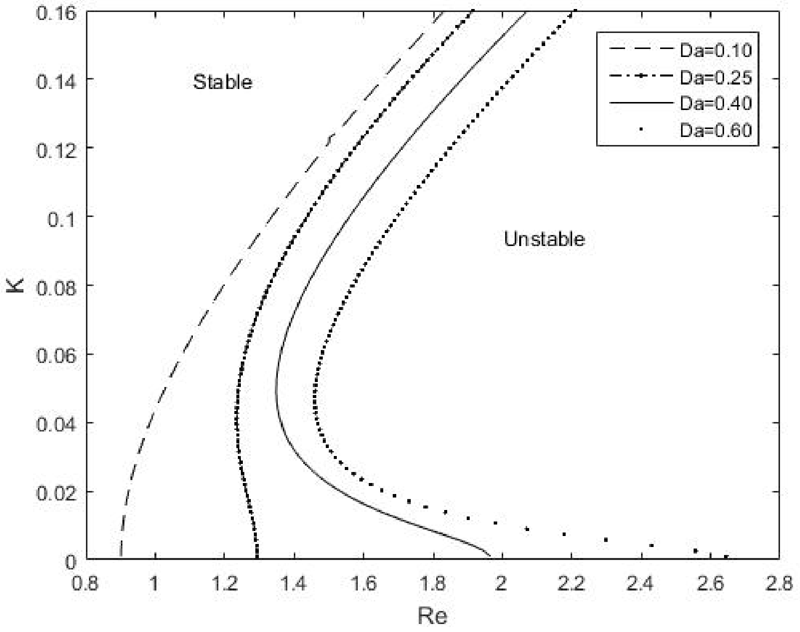

Figure 2.4: Effect of stability of long wave flows for different values of D_a with $\cot\theta = 1, d = 3, \phi = 0.01, \alpha_{BJ} = 2, K_a = 100, c_F = 0.55$.

Permeability D_a (Darcy number) underlying in porous media plays an important role in determining the stability on the long wave surface flows. To observe effect of the permeability on the long-wave stability, we fix $\cot\theta = 1, d = 3, \phi = 0.1, \alpha_{BJ} = 1, c_F = 0.55, K_a = 100$. In Fig. 2.4, the marginal curves for different permeability $D_a = 0.10, 0.25, 0.40$ and 0.60 are presented and observed that the bigger the permeability D_a, more stable in long wave flow ; but higher permeability has higher difference in $R_{e,crit}$ and $R_{e,0}$. Thus, it tells us that there is more sensitive areas to determine the stable/unstable condition in application for higher permeability case.

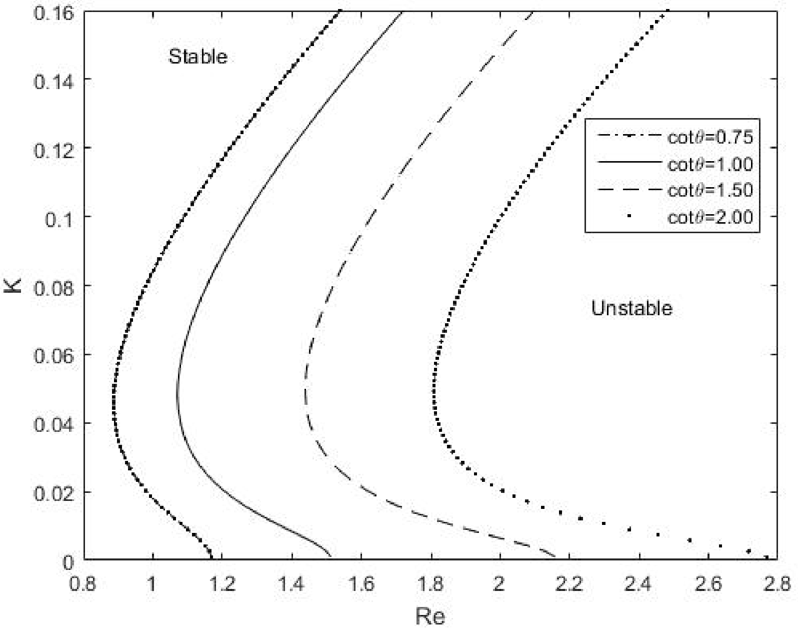

Figure 2.5: Effect of stability of long wave flows for different values of $\cot\theta$ with $K_a = 100, d = 1, \phi = 0.01, \alpha_{BJ} = 1, D_a = 0.4, c_F = 0.5$.

The marginal stability curves move (shift) from right to left as the cotangent value of angle θ increases, i.e. the inclination of porous medium substrate decreases. Fig. 2.5

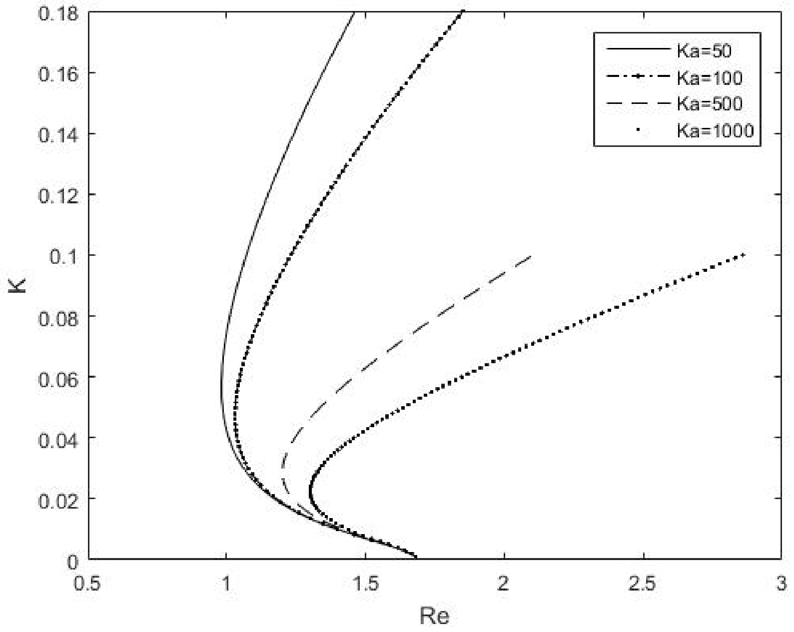

Figure 2.6: Effect of stability of long wave flows for different different surface tensions of K_a with $\cot\theta = 1, d = 1, \phi = 0.01, \alpha_{BJ} = 1, D_a = 0.5, c_F = 0.55$.

shows that the long wave flow can be stabilized for decreasing inclination. It is observed that the angle of inclination is also highly influenced factor as expected to stabilize flow. The marginal stability curves of long wave flows for different surface tension values K_a are shown in Fig. 2.6. The marginal curves have a common intercept with R_e-axis. It shows that the effect of surface tensions on the expression of $R_{e,0}$ is independent of surface tensions K_a for the large long wave solutions (where the wavenumber value is as small as $K \to 0$, i.e. K is less than 0.02) and the stability region of large long wave flows is unchanged as surface tension changes. However, as expected, in cases where the moderate long wave solution (with a proper small wavenumber K, i.e. K is from $0.02 - 0.15$) is stable, the surface tension affects the onset of stability of the flow. It shows that the moderate long wave flow is more stable as the surface tension increases.

These are also presented in [28, 38].

In the fluid-porous medium interface condition, the dimensionless Beaver-Joseph parameter α_{BJ} characterizes the structure of the permeability material near the fluid-porous medium interface. Beaver and Joseph's work [8] indicated that this parameter α_{BJ} should be assigned values between 0.1 and 4. In Fig. 2.7, the marginal stability curves display different values of $\alpha_{BJ}(= 1, 2, 3, 4)$. The marginal curves move from right to left when α_{BJ} increases, which means that for smaller Beaver-Joseph constant α_{BJ}, the long wave flows obviously becomes more unstable. On the other hand, effects of larger value α_{BJ} are indistinguishable but it is more sensitive to small α_{BJ}.

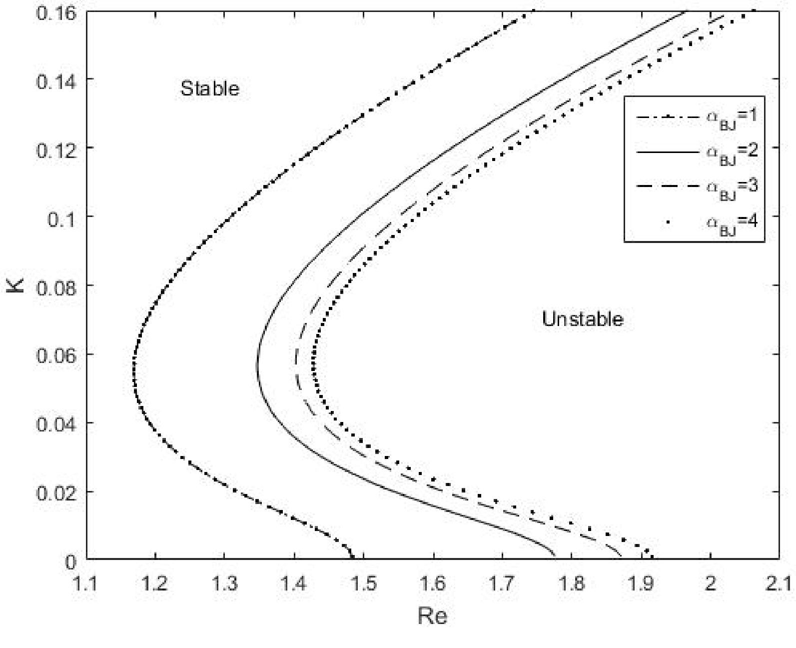

Figure 2.7: Effect of stability of long wave flows for different values of α_{BJ} with $\cot\theta = 1, d = 2, \phi = 0.01, K_a = 100, D_a = 0.3, c_F = 0.55$.

As it can be seen in Fig. 2.8, varying porosity ϕ of porous medium has a big effect as

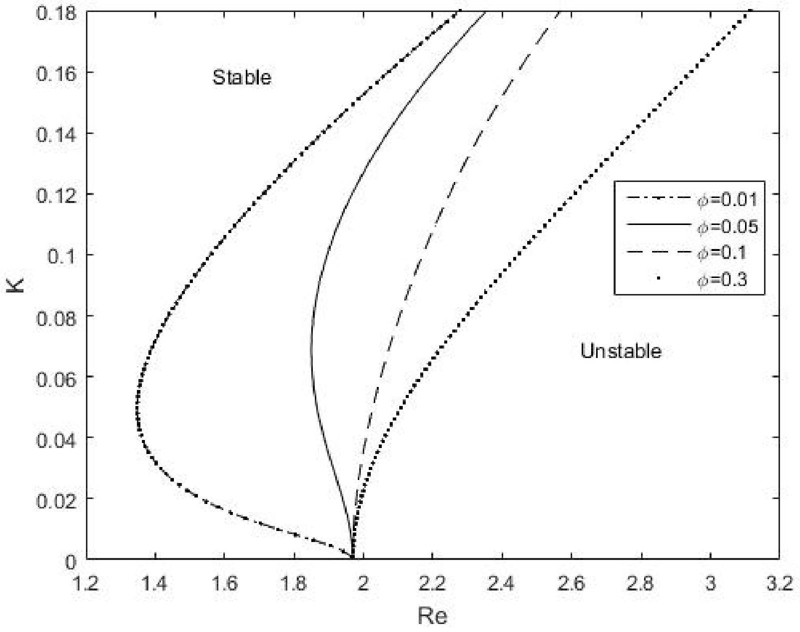

Figure 2.8: Effect of stability of long wave flows for different porosities of ϕ with $\cot\theta = 1, d = 1, K_a = 100, \alpha_{BJ} = 2, D_a = 0.4, c_F = 0.55$.

varying K_a. Specifically, increasing porosity ϕ stabilizes the flows where the moderate long wave perturbations are amplified at the onset, and for larger porosity ϕ the flow becomes more unstable. However, for large long wave solutions (where the wavenumber value is as small as $K \to 0$) the value $R_{e,crit}$ coincides with $R_{e,0}$. Fig. 2.9 illustrate the effect of d, the scaled thickness off the porous substrate, on the neutral stability of long wave. From these results we conclude that increasing the thickness of the substrate stabilizes the flow in long wave. However, as length of wave of flow (moderate long wave) decreases, the stability region is unchanged.

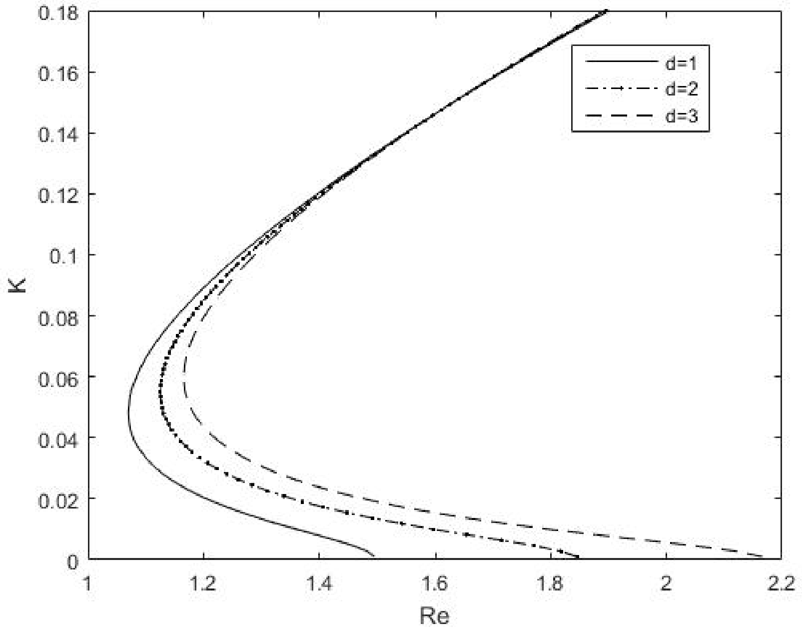

Figure 2.9: Effect of stability of long wave flows for different value of d with $\cot\theta = 1, \phi = 0.01, K_a = 100, \alpha_{BJ} = 2, D_a = 0.4, c_F = 0.55$.

2.6 Conclusion

In this work , we derived out a model for free surface flows over inclined porous media with nonlinear Forchheirmer's law. We investigated and analyzed the stability of the long wave solutions of surface flows affected by fluid properties and porous media parameters; where the infinitesimal perturbations were determined and they would naturally interact with equilibrium steady-state flows. An Orr-Sommerfeld system, from the linearized governing equations and boundary conditions, is solved numerically to get critical condition for the stability of long wave flows. The influences of key parameters $c_F, D_a, \cot\theta, K_a, \alpha_{BJ}$ and ϕ on the stability are studied and analyzed focusing on the long wave solutions.

We compared our results with Darcy's law and obtained an excellent agreement with our model of nonlinear Forchheirmer's law with very small drag constant c_F. The results indicated that the threshold critical Reynolds number is larger than analytic solution ($R_{e,0} = \frac{5}{6}\cot\theta$) in an impermeable inclined plane given in [10]. One notable observation was that the drag constant c_F affects the onset of stability and the smaller drag constant acts to stabilize the long wave flows. We took some ranges of permeability value, higher permeability and concluded that the effect of substrate permeability acts to stabilize the flows as increasing permeability; but at the same time it strongly depends on other parameters such as ϕ , α_{BJ}. Similar results can be observed on the effects of inclination of substrate and Beaver-Josheph parameter, but these parameters affect moving the critical curve from right to left as increasing their values. Our results showed that surface tension and substrate porosity have in general a stabilizing influence upon the moderate long wave flows but there are small effects in large long wave flows.

The important feature of our study is that we obtained results of long wave solutions of free surface flows over porous media flows modelled by nonlinear Forchheimer's law. Our results of critical stability value $R_{e,crit}$ for very small wavenumber K are validated by analytical analyzing in [91] and the marginal stability curve of our nonlinear model is compared- for very small drag constant c_F- to that of Darcy's law [42]. With various drag constant c_F, the critical stability curves $R_e = R_{e,crit}$ and the stable regions of long wave solutions of surface flows are obtained accurately by model of nonlinear Forchheimer's law model. In fact, we obtained and analyzed seven sets of characteristic stability marginal curves and stable and unstable regions based on different fluid properties and porous media parameters. These curves that identified the transitions shift stable and unstable flow regimes can provoke crucial flow stabilization, which is important in fluid mechanics and physical and technical applications. By considering the sets of transitions, we can show a pathway - the long wave surface flows of considered Newtonian fluid flowing down in filtration inclines evolved when above mentioned system parameters were changed. The present study and obtained results will provide the guide on how to tune the stability of long wave flows of the Newtonian fluid flowing over an inclined coupled bottom filtration in a way which is desired or required.

Chapter 3

The mass-preserving solution-flux scheme for multi-layer interface parabolic equations

3.1 Introduction

Time-dependent partial differential equations are widely used in science and engineering. Mathematical models of diffusion in layered materials arise in many industrial, environmental, biological and medical applications, such as heat conduction in composite materials, transport of contamination flow, chemicals and gases in layered porous media, brain tumor growth, heat conduction through skin, transdermal drug delivery and greenhouse gas emissions [16]. Since the physical solution of non-smooth or even discontinuous across the interface, the standard numerical methods often perform poorly for parabolic interface problems. Some efforts have been made for solving elliptic interface equations and parabolic interface equations such as interface FD methods, fictitious-domain methods and MIB schemes in [30, 35, 45, 52, 54, 60, 63, 94, 95] and numerical methods for solving multi-layer diffusion problems in [17, 33, 62, 64, 76]. Mass conservation solutions in such layered problems are important and another challenging work to do. To resolve this issue, in this chapter, we propose a novel mass-preserving solution-flux finite difference method for solving time-dependent multi-layer problems where there are solution-jump conditions and flux-jump conditions along interfaces. The solution and flux schemes are proposed to solve it at regular grid points in each layer or subdomain whereas the whole domain is divided into staggered meshes. But , having the interface jump conditions in each connected layer, it is challenging to define the approximate fluxes at the irregular points next to interfaces for satisfying mass conservation for the scheme across the interfaces. We propose novel corrected approximate fluxes from two sides of the interface (as "+" and "−") at the irregular points by combining with the interface conditions at interfaces, which ensure the developed solution-flux scheme mass conservative while keeping accuracy. We prove the proposed schemes to satisfy conservation of mass in the discrete form for 1D and 2D parabolic interface equations with multi-layers. Section 3.2 is for 1D problem and Section 3.3 is for 2D problem. In Section 3.4, numerical experiments are given for both 1D problems and 2D problems to show mass conservation and convergence orders of our proposed schemes in time and space step sizes. Also, we compute the real applications of the diffusion process with large difference piecewise diffusion coefficients and the heat propagation in the multi-layer media. The conclusions and future work are given in Section 3.5.

3.2 One dimensional multi-point interface parabolic equation and its solution-flux scheme

Consider one-dimensional parabolic equation with m-interface points

$$\frac{\partial u(x,t)}{\partial t} = \beta_k \frac{\partial^2 u(x,t)}{\partial x^2} + f(x,t), \qquad x \in I_k, k = 0, 1, \ldots, m,\ t \in (0, T] \tag{3.1}$$

where the interface points $\Gamma_k,\ k = 1, 2, \ldots, m$, divide the domain $I = [a, b]$ into $m + 1$ sub-domains $I_k,\ k = 0, 1, \ldots, m$.

It satisfies the solution-jump and flux-jump conditions

$$[u]_{\Gamma_k} = u^+_{\Gamma_k} - u^-_{\Gamma_k} = \phi_k(t),\ [\beta u_x]_{\Gamma_k} = \beta_k \frac{\partial u^+_{\Gamma_k}}{\partial x} - \beta_{k-1} \frac{\partial u^-_{\Gamma_k}}{\partial x} = \psi_k(t), \quad k = 1, 2, \ldots, m, \tag{3.2}$$

and the Neumann boundary condition and initial condition

$$\tfrac{\partial u}{\partial x}(a,t) = g_a(t),\ \tfrac{\partial u}{\partial x}(b,t) = g_b(t), \quad t \in (0, T] \tag{3.3}$$

$$u(x, 0) = u_0(x), \quad x \in I. \tag{3.4}$$

Where $u(x,t)$ is the unknown function, β_k are diffusion coefficients in different sub-domains, $f(x,t)$ is a source function, and $T > 0$ is time period. The superscripts "$-$" and "$+$" denote the limiting values of a function from the left side and the right side of interface point respectively.

Let the flux

$$q^x = q^x(x,t) = \beta_k \frac{\partial u}{\partial x}, \quad x \in I_k. \tag{3.5}$$

Then equation (3.1) can be written as

$$\frac{\partial u}{\partial t} - \frac{\partial q^x}{\partial x} = f, \qquad x \in I_k, k = 0, 1, \ldots, m. \tag{3.6}$$

3.2.1 The mass-preserving solution-flux scheme

In the construction of scheme, for preserving mass, we develop the solution-flux scheme on the staggered mesh over subdomains. Let $\Delta x = \frac{b-a}{N_x}$ and $\Delta t = \frac{T}{N_t}$ be the space step size and time step size respectively, N_x and N_t are non-negative integers.

Define

$$x_{i+\frac{1}{2}} = a + i\Delta x,\ i = 0, 1, \ldots, N_x;\ x_i = a + (i - \frac{1}{2})\Delta x,\ i = 1, 2, \ldots, N_x.$$

The time interval $(0, T]$ is discretized uniformly by

$$t^n = n\Delta t, \qquad n = 0, 1, \ldots, N_t.$$

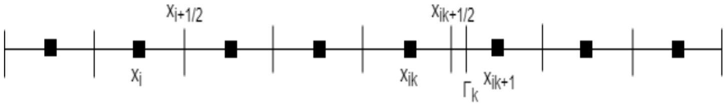

Figure 3.1: The staggered mesh of points x_i and $x_{i+\frac{1}{2}}$.

The $x_{i+\frac{1}{2}}$ and x_i are nodes for the flux q^x_k and the solution u respectively (see Fig.

3.1). Denote $r_k^x = \beta_k \frac{\Delta t}{(\Delta x)^2}$. For grid functions $\{W_i\}$ and $\{W_{i+\frac{1}{2}}\}$, define the space central difference operators as

$$\delta_x W_{i+\frac{1}{2}} = \frac{W_{i+1} - W_i}{\Delta x}, \quad \delta_x W_i = \frac{W_{i+\frac{1}{2}} - W_{i-\frac{1}{2}}}{\Delta x}.$$

On the staggered mesh, we use U_i^n to denote the approximation to solution $u_i^n = u(x_i, t^n)$ and $Q_{i+\frac{1}{2}}^{x,n}$ to denote the approximation to flux $q^x(x_{i+\frac{1}{2}}, t^n)$. The interface point Γ_k can be set as $x_{i_k+\frac{1}{2}} = \Gamma_k$ for some cases and will be within one mesh element $[x_{i_k}, x_{i_k+1}]$ for other cases. A node x_i is regular if it is not next to Γ_k and it is irregular if it is next to Γ_k.

At all regular points in the interiors of subdomains, we approximate the flux by using the central difference operator

$$Q_{i+\frac{1}{2}}^{x,n+1} = \beta_k \delta_x U_{i+\frac{1}{2}}^{n+1}. \tag{3.7}$$

where node x_i is not next to Γ_k.

However, at the irregular points x_{i_k} and x_{i_k+1} which are next to interfaces Γ_k, due to the interface jump conditions, it is very challenging to define the approximation flux in order to satisfy mass conservation for the scheme across the interfaces while keeping accuracy. In the following part, we will propose novel corrected approximate fluxes (3.24)(3.25) below for the irregular points next to interfaces Γ_k.

Let the interface point Γ_k located at α_k be between x_{i_k} and x_{i_k+1}, and $x_{i_k} \in I_{k-1} =$

(Γ_{k-1}, Γ_k) and $x_{i_k+1} \in I_k = (\Gamma_k, \Gamma_{k+1})$, where x_{i_k} and x_{i_k+1} are called the irregular nodes. By the definition of space central difference for $q^x_{i_k+\frac{1}{2}}$ at $x_{i_k+\frac{1}{2}}$, we can define from the left side

$$q^{-,x}_{i_k+\frac{1}{2}} = \beta_{k-1}\frac{u^-_{i_k+1} - u^-_{i_k}}{\Delta x} \tag{3.8}$$

and from the right side

$$q^{+,x}_{i_k+\frac{1}{2}} = \beta_k\frac{u^+_{i_k+1} - u^+_{i_k}}{\Delta x}. \tag{3.9}$$

Equations (3.8) and (3.9) can be written as

$$q^{-,x}_{i_k+\frac{1}{2}} = \frac{1}{\Delta x}\left[\left(\beta_k u^+_{i_k+1} - \beta_{k-1}u^-_{i_k}\right) + \left(\beta_{k-1}u^-_{i_k+1} - \beta_k u^+_{i_k+1}\right)\right] \tag{3.10}$$

$$q^{+,x}_{i_k+\frac{1}{2}} = \frac{1}{\Delta x}\left[\left(\beta_k u^+_{i_k+1} - \beta_{k-1}u^-_{i_k}\right) + \left(\beta_{k-1}u^-_{i_k} - \beta_k u^+_{i_k}\right)\right]. \tag{3.11}$$

Using Taylor's expansions of $u^-_{i_k+1}, u^+_{i_k+1}, u^-_{i_k}$ and $u^+_{i_k}$ about the point α_k, the second terms of the right sides of (3.10)(3.11) can be expressed as

$$\begin{aligned}&\frac{1}{\Delta x}\left(\beta_{k-1}u^-_{i_k+1} - \beta_k u^+_{i_k+1}\right) = \\ &\quad -\frac{1}{\Delta x}\left([\beta u]_{\Gamma_k} + (x_{i_k+1} - \alpha_k)[\beta u_x]_{\Gamma_k} + \frac{1}{2}(x_{i_k+1} - \alpha_k)^2[\beta u_{xx}]_{\Gamma_k}\right) + O(\Delta x^2),\end{aligned}$$

$$\begin{aligned}&\frac{1}{\Delta x}\left(\beta_{k-1}u^-_{i_k} - \beta_k u^+_{i_k}\right) = \\ &\quad -\frac{1}{\Delta x}\left([\beta u]_{\Gamma_k} + (x_{i_k} - \alpha_k)[\beta u_x]_{\Gamma_k} + \frac{1}{2}(x_{i_k} - \alpha_k)^2[\beta u_{xx}]_{\Gamma_k}\right) + O(\Delta x^2).\end{aligned}$$

Thus, we can have the following lemma.

Lemma 1. *Suppose that the interface point Γ_k lies between x_{i_k} and x_{i_k+1}, locating at α_k, and $x_{i_k} \in I_{k-1}$, $x_{i_k+1} \in I_k$. Then the following approximations hold*

$$q^{-,x}_{i_k+\frac{1}{2}} = \frac{\beta_k u_{i_k+1} - \beta_{k-1} u_{i_k}}{\Delta x} + (\chi_x)_{i_k} + O(\Delta x^2) \tag{3.12}$$

$$q^{+,x}_{i_k+\frac{1}{2}} = \frac{\beta_k u_{i_k+1} - \beta_{k-1} u_{i_k}}{\Delta x} + (\chi_x)_{i_k+1} + O(\Delta x^2) \tag{3.13}$$

where

$$(\chi_x)_{i_k} = -\frac{1}{\Delta x}\left([\beta u]_{\Gamma_k} + (x_{i_k+1} - \alpha_k)[\beta u_x]_{\Gamma_k} + \frac{1}{2}(x_{i_k+1} - \alpha_k)^2[\beta u_{xx}]_{\Gamma_k}\right) \tag{3.14}$$

$$(\chi_x)_{i_k+1} = -\frac{1}{\Delta x}\left([\beta u]_{\Gamma_k} + (x_{i_k} - \alpha_k)[\beta u_x]_{\Gamma_k} + \frac{1}{2}(x_{i_k} - \alpha_k)^2[\beta u_{xx}]_{\Gamma_k}\right). \tag{3.15}$$

Remark 1. *If an interface Γ_k lies at the midpoint of x_{i_k} and x_{i_k+1} i.e. $\alpha_k = \frac{x_{i_k}+x_{i_k+1}}{2}$, then the terms $(\chi_x)_{i_k}$ and $(\chi_x)_{i_k+1}$ will be*

$$(\chi_x)_{i_k} = -\tfrac{1}{\Delta x}\left([\beta u]_{\Gamma_k} + \tfrac{\Delta x}{2}[\beta u_x]_{\Gamma_k} + \tfrac{\Delta x^2}{8}[\beta u_{xx}]_{\Gamma_k}\right), \tag{3.16}$$

$$(\chi_x)_{i_k+1} = -\tfrac{1}{\Delta x}\left([\beta u]_{\Gamma_k} - \tfrac{\Delta x}{2}[\beta u_x]_{\Gamma_k} + \tfrac{\Delta x^2}{8}[\beta u_{xx}]_{\Gamma_k}\right). \tag{3.17}$$

In (3.14)(3.15)(3.16)(3.17), there are three jump terms $[\beta u]_{\Gamma_k}, [\beta u_x]_{\Gamma_k}$ and $[\beta u_{xx}]_{\Gamma_k}$ in the corrections $(\chi_x)_{i_k}$ and $(\chi_x)_{i_k+1}$. The jump term $[\beta u]_{\Gamma_k}$ at the interface Γ_k is equivalent to the either $\beta_k\phi_k + (\beta_k - \beta_{k-1})u^-_{\Gamma_k}$ or $\beta_{k-1}\phi_k + (\beta_k - \beta_{k-1})u^+_{\Gamma_k}$. $[\beta u]_{\Gamma_k}$ can then be written as

$$[\beta u]_{\Gamma_k} = \frac{1}{2}\left((\beta_k + \beta_{k-1})\phi_k + (\beta_k - \beta_{k-1})(u^-_{\Gamma_k} + u^+_{\Gamma_k})\right). \tag{3.18}$$

The value of $u^-_{\Gamma_k}$ is explicitly evaluated by extrapolation $E^-_{\Gamma_k}(U)$ using the values U_{i_k-2}, U_{i_k-1} and U_{i_k}. Similarly $u^+_{\Gamma_k}$ is explicitly evaluated as $E^+_{\Gamma_k}(U)$ by using U_{i_k+1}, U_{i_k+2} and U_{i_k+3}. Thus,

$$[\beta u]_{\Gamma_k} \approx \frac{1}{2}\left((\beta_k + \beta_{k-1})\phi_k + (\beta_k - \beta_{k-1})(E^-_{\Gamma_k}(U) + E^+_{\Gamma_k}(U))\right). \tag{3.19}$$

The jump term $[\beta u_x]_{\Gamma_k}$ is the second jump condition of (3.2) given as

$$[\beta u_x]_{\Gamma_k} = \psi_k. \tag{3.20}$$

Further, we consider that diffusion coefficients β_k in (3.1) are constants. From the first equation of (3.1), we can have at interface point Γ_k

$$u^-_t = \beta_{k-1} u^-_{xx} + f^-, \quad x \in I_{k-1} \tag{3.21}$$

and

$$u^+_t = \beta_k u^+_{xx} + f^+, \quad x \in I_k. \tag{3.22}$$

Subtracting from (3.22) to (3.21) and using first jump condition of (3.2), we obtain that

$$[\beta u_{xx}]_{\Gamma_k} = \phi_{kt} - [f]_{\Gamma_k} \tag{3.23}$$

where the suffix t expresses the time derivative, and $[f]_{\Gamma_k} = f^+ - f^-$ at Γ_k.

Therefore, at the irregular points next to interface Γ_k, where Γ_k is located at $x = \alpha_k$, from (3.19)(3.20)(3.23), we can define the corrected approximate fluxes as that

$$Q^{-,x,n+1}_{i_k+\frac{1}{2}} = \frac{\beta_k U^{n+1}_{i_k+1} - \beta_{k-1} U^{n+1}_{i_k}}{\Delta x} + (\bar{\chi}_x)^{n+1}_{i_k}, \tag{3.24}$$

$$Q^{+,x,n+1}_{i_k+\frac{1}{2}} = \frac{\beta_k U^{n+1}_{i_k+1} - \beta_{k-1} U^{n+1}_{i_k}}{\Delta x} + (\bar{\chi}_x)^{n+1}_{i_k+1}, \tag{3.25}$$

where the corrections $(\chi_x)_{i_k}$ and $(\chi_x)_{i_k+1}$ are explicitly defined

$$\begin{aligned}
(\bar{\chi}_x)^{n+1}_{i_k} &= -\frac{1}{\Delta x}\Big(\frac{1}{2}(\beta_k + \beta_{k-1})\phi_k^{n+1} + \frac{1}{2}(\beta_k - \beta_{k-1})(E^-_{\Gamma_k}(U^n) + E^+_{\Gamma_k}(U^n)) \\
&\quad + (x_{i_k+1} - \alpha_k)\psi_k^{n+1} + \frac{1}{2}(x_{i_k+1} - \alpha_k)^2({\phi_k}_t^{n+1} - [f^{n+1}]_{\Gamma_k})\Big), && (3.26) \\
(\bar{\chi}_x)^{n+1}_{i_k+1} &= -\frac{1}{\Delta x}\Big(\frac{1}{2}(\beta_k + \beta_{k-1})\phi_k^{n+1} + \frac{1}{2}(\beta_k - \beta_{k-1})(E^-_{\Gamma_k}(U^n) + E^+_{\Gamma_k}(U^n)) \\
&\quad + (x_{i_k} - \alpha_k)\psi_k^{n+1} + \frac{1}{2}(x_{i_k} - \alpha_k)^2({\phi_k}_t^{n+1} - [f^{n+1}]_{\Gamma_k})\Big). && (3.27)
\end{aligned}$$

Finally, using (3.7) for regular points and using (3.24) and (3.25) for irregular points in subdomains, we can propose the mass-preserving solution-flux scheme for the multipoints interface parabolic equation as

$$\frac{U_i^{n+1} - U_i^n}{\Delta t} - \delta_x Q_i^{x,n+1} = f_i^{n+1}, \qquad x_i \in I_k, \quad k = 0, 1, \ldots, m, \tag{3.28}$$

and for regular point x_i,

$$Q_{i+\frac{1}{2}}^{x,n+1} = \beta_k \delta_x U_{i+\frac{1}{2}}^{n+1}, \tag{3.29}$$

and for the irregular points x_{i_k} and x_{i_k+1} next to interfaces Γ_k,

$$Q_{i_k+\frac{1}{2}}^{-,x,n+1} = \frac{\beta_k U_{i_k+1}^{n+1} - \beta_{k-1} U_{i_k}^{n+1}}{\Delta x} + (\bar{\chi}_x)_{i_k}^{n+1}, \tag{3.30}$$

$$Q_{i_k+\frac{1}{2}}^{+,x,n+1} = \frac{\beta_k U_{i_k+1}^{n+1} - \beta_{k-1} U_{i_k}^{n+1}}{\Delta x} + (\bar{\chi}_x)_{i_k+1}^{n+1}. \tag{3.31}$$

If the interface Γ_k is not located at the middle point $x_{i_k+\frac{1}{2}}$ of x_{i_k} and x_{i_k+1}, i.e. $x_{i_k+\frac{1}{2}} \neq \alpha_k$, then at these two irregular points x_{i_k} and x_{i_k+1}, scheme (3.28) is considered as

$$\frac{U_{i_k}^{n+1} - U_{i_k}^n}{\Delta t} - \delta_x Q_{i_k}^{x,n+1} = f_{i_k}^{n+1} + R_{i_k}^{n+1}, \quad at\ x_{i_k} \tag{3.32}$$

$$\frac{U_{i_k+1}^{n+1} - U_{i_k+1}^n}{\Delta t} - \delta_x Q_{i_k+1}^{x,n+1} = f_{i_k+1}^{n+1} + R_{i_k+1}^{n+1}, \quad at\ x_{i_k+1} \tag{3.33}$$

where $R_{i_k}^{n+1} = -\frac{1}{2\Delta x}(x_{i_k} - \alpha_k)^2 ({\phi_k}_t^{n+1} - [f^{n+1}]_{\Gamma_k})$, $R_{i_k+1}^{n+1} = \frac{1}{2\Delta x}(x_{i_k+1} - \alpha_k)^2 ({\phi_k}_t^{n+1}$ $-[f^{n+1}]_{\Gamma_k})$.

The boundary conditions are provided by

$$Q_{\frac{1}{2}}^{x,n+1} = g_a^{n+1}, \qquad Q_{I+\frac{1}{2}}^{x,n+1} = g_b^{n+1}, \qquad x_{\frac{1}{2}} = a, x_{I+\frac{1}{2}} = b \tag{3.34}$$

and the initial condition is given by

$$U_i^0 = U_0(x_i), \qquad x_i \in I_k,\ k = 0, 1, \ldots, m. \tag{3.35}$$

3.2.2 The Discrete Mass Conservation

We now prove the discrete mass conservation of our solution-flux scheme (3.28)-(3.35).

Theorem 2. *The solution-flux scheme given in (3.28)-(3.35) satisfies the mass conservation in the discrete form over whole domian, i.e.*

$$\begin{aligned}\sum_{i=1}^{N_x} U_i^{n+1}\Delta x + \sum_{k=1}^{m}\sum_{n=0}^{N_t-1}\psi_k^{n+1}\Delta t = \quad & \sum_{i=1}^{N_x} U_i^0\Delta x + \sum_{n=0}^{N_t-1}\sum_{i=1}^{N_x} f_i^{n+1}\Delta x\Delta t \\ & + \sum_{n=0}^{N_t-1}\left(g_b^{n+1} - g_a^{n+1}\right)\Delta t.\end{aligned} \tag{3.36}$$

Proof: If the interfaces Γ_k, $k = 1, 2, \ldots, m$, are located at $x_{i_k+\frac{1}{2}}$, then multiplying the first equation of (3.28) by Δx and summing i from 1 to N_x, we can obtain that

$$\sum_{i=1}^{N_x}\frac{U_i^{n+1} - U_i^n}{\Delta t}\Delta x = \sum_{i=1}^{N_x}\delta_x Q_i^{x,n+1}\Delta x + \sum_{i=1}^{N_x} f_i^{n+1}\Delta x. \tag{3.37}$$

But if there are interfaces Γ_l, $l = 1, 2, \ldots m_1$, that are not located at $x_{i_l+\frac{1}{2}}$, i.e. $x_{i_l+\frac{1}{2}} \neq \alpha_l$, for $l = 1, 2, \ldots m_1$, then multiplying equation (3.28) together with (3.32)

(3.33) by Δx, summing i from 1 to N_x gets to

$$\sum_{i=1}^{N_x} \frac{U_i^{n+1} - U_i^n}{\Delta t} \Delta x = \sum_{i=1}^{N_x} \delta_x Q_i^{x,n+1} \Delta x + \sum_{i=1}^{N_x} f_i^{n+1} \Delta x + \sum_{l=1}^{m_1} (R_{i_l} + R_{i_l+1}) \Delta x \tag{3.38}$$

Since, for that x_i is the regular point,

$$\delta_x Q_i^{x,n+1} = \frac{\left(Q_{i+\frac{1}{2}}^{x,n+1} - Q_{i-\frac{1}{2}}^{x,n+1}\right)}{\Delta x}, \tag{3.39}$$

and $Q_{\frac{1}{2}}^{x,n+1} = g_a^{n+1}, \quad Q_{I+\frac{1}{2}}^{x,n+1} = g_b^{n+1}$, then we have that

$$\sum_{i=1}^{N_x} \delta_x Q_i^{x,n+1} \Delta x = \sum_{k=1}^{m} \frac{\left(Q_{i_k+\frac{1}{2}}^{-x,n+1} - Q_{i_k+\frac{1}{2}}^{+x,n+1}\right)}{\Delta x} \Delta x + \left(g_b^{n+1} - g_a^{n+1}\right). \tag{3.40}$$

Using (3.30) (3.31) and (3.26)(3.27), it further holds that

$$\begin{aligned} \sum_{i=1}^{N_x} \delta_x Q_i^{x,n+1} \Delta x \quad &= \quad -\frac{1}{\Delta x} \sum_{k=1}^{m} \left[{\psi_k}^{n+1} + \frac{1}{2}(x_{i_k+1} + x_{i_k} - 2\alpha_k)({\phi_k}_t^{n+1} - [f^{n+1}]_{\Gamma_k}) \right] \Delta x \\ &\quad + \left(g_b^{n+1} - g_a^{n+1}\right). \end{aligned} \tag{3.41}$$

If the interface Γ_k is located at $x_{i_k+\frac{1}{2}}$, i.e., $\alpha_k = x_{i_k+\frac{1}{2}}$, then $x_{i_k+1} + x_{i_k} - 2\alpha_k = 0$, and thus (3.41) becomes

$$\sum_{i=1}^{N_x} \delta_x Q_i^{x,n+1} \Delta x = -\sum_{k=1}^{m} \psi_k^{n+1} + \left(g_b^{n+1} - g_a^{n+1}\right) \tag{3.42}$$

If there are interfaces Γ_l, $l = 1, 2, \ldots m_1$, that are not located at $x_{i_l+\frac{1}{2}}$, i.e. $x_{i_l+\frac{1}{2}} \neq \alpha_l$, for $l = 1, 2, \ldots m_1$, then (3.41) becomes

$$\begin{aligned}\sum_{i=1}^{N_x} \delta_x Q_i^{x,n+1} \Delta x &= -\sum_{k=1}^{m} \psi_k^{n+1} - \sum_{l=1}^{m_1} \frac{1}{2}(x_{i_l+1} + x_{i_l} - 2\alpha_l)({\phi_l}_t^{n+1} - [f^{n+1}]_{\Gamma_l}) \\ &\quad + \left(g_b^{n+1} - g_a^{n+1}\right). \end{aligned} \tag{3.43}$$

If all interfaces Γ_k are located at the middle points $x_{i_k+\frac{1}{2}} = \alpha_k$, substituting equation (3.42) into (3.37); Otherwise, substituting equation (3.43) into (3.38), and multiplying with Δt and summing n from 0 to $N_t - 1$, we finally get equation (3.36). This ends the proof.

3.3 Two dimensional multi-layer interface parabolic equation and its solution-flux scheme

Consider two-dimensional parabolic equation with multi-layer interfaces. Let $x = \Gamma_k$, $k = 1, 2, \ldots, m$, be the interfaces of domain $\Omega = [a, b] \times [c, d]$, and $\Omega_k = (\Gamma_k, \Gamma_{k+1}) \times (c, d)$, $k = 1, 2, \ldots, m-1$, and $\Omega_0 = (a, \Gamma_1) \times (c, d)$ and $\Omega_m = (\Gamma_m, b) \times (c, d)$. (see Fig. 3.2)

$$\frac{\partial u(x,y,t)}{\partial t} = \beta_k \left(\frac{\partial^2 u(x,y,t)}{\partial x^2} + \frac{\partial^2 u(x,y,t)}{\partial y^2} \right) + f(x,y,t),$$

$$(x, y, t) \in \Omega_k \times (0, T], \;\; k = 0, 1, 2, \ldots, m \tag{3.44}$$

and the solution-jump interface conditions and the flux-jump interface conditions

$$[u]_{\Gamma_k} = u^{+}_{\Gamma_k} - u^{-}_{\Gamma_k} = \phi_k(y,t), \quad y \in (c,d), \ k = 1, 2, \ldots, m, \tag{3.45}$$

$$[\beta u_x]_{\Gamma_k} = \beta_k \frac{\partial u^{+}_{\Gamma_k}}{\partial x} - \beta_{k-1} \frac{\partial u^{-}_{\Gamma_k}}{\partial x} = \psi_k(y,t), \quad y \in (c,d), \ k = 1, 2, \ldots, m \tag{3.46}$$

The boundary condition is considered as the Neumann boundary condition

$$\frac{\partial u(a,y,t)}{\partial x} = g_a(y,t), \quad \frac{\partial u(b,y,t)}{\partial x} = g_b(y,t), \qquad y \in (c,d), t \in (0,T] \tag{3.47}$$

and

$$\frac{\partial u(x,c,t)}{\partial y} = h_c(x,t), \quad \frac{\partial u(x,d,t)}{\partial y} = h_d(x,t), \qquad x \in (a,b), t \in (0,T] \tag{3.48}$$

and the initial condition is

$$u(x,y,0) = u_0(x,y), \qquad (x,y) \in \Omega, \tag{3.49}$$

where $u(x,y,t)$ is the unknown function of interests, β_k, $k = 0, 1, \ldots, m$, are the diffusion constant coefficients, and $f(x,y,t)$ is a source term, and $T > 0$ is the time period. The superscripts " $-$ " and " $+$ " denote the limiting value of a function from the left side and the right side of interfaces respectively.

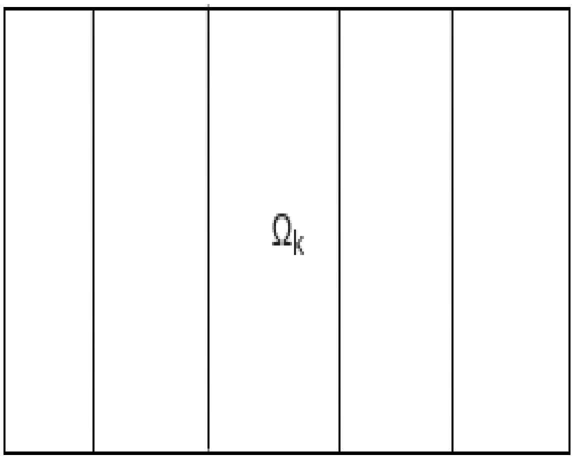

Figure 3.2: The multi-layer domain

Let the x-flux and the y-flux be

$$q^x = \beta_k \frac{\partial u}{\partial x}, \quad (x,y) \in \Omega_k \tag{3.50}$$

$$q^y = \beta_k \frac{\partial u}{\partial y}, \quad (x,y) \in \Omega_k, \tag{3.51}$$

then, equation (3.44) can be written as

$$\frac{\partial u(x,y,t)}{\partial t} - \left(\frac{\partial}{\partial x} q^x + \frac{\partial}{\partial y} q^y \right) = f(x,y,t),\ (x,y) \in \Omega_k,\ k = 0,1,2,\ldots,m. \tag{3.52}$$

3.3.1 The mass-preserving solution-flux scheme in 2D

We introduce the staggered mesh for u , q^x and q^y. Let $\Delta x = \frac{b-a}{N_x}$, $\Delta y = \frac{d-c}{N_y}$ and $\Delta t = \frac{T}{N_t}$ be the space step sizes and time step size respectively. N_x, N_y and N_t are non-negative integers.

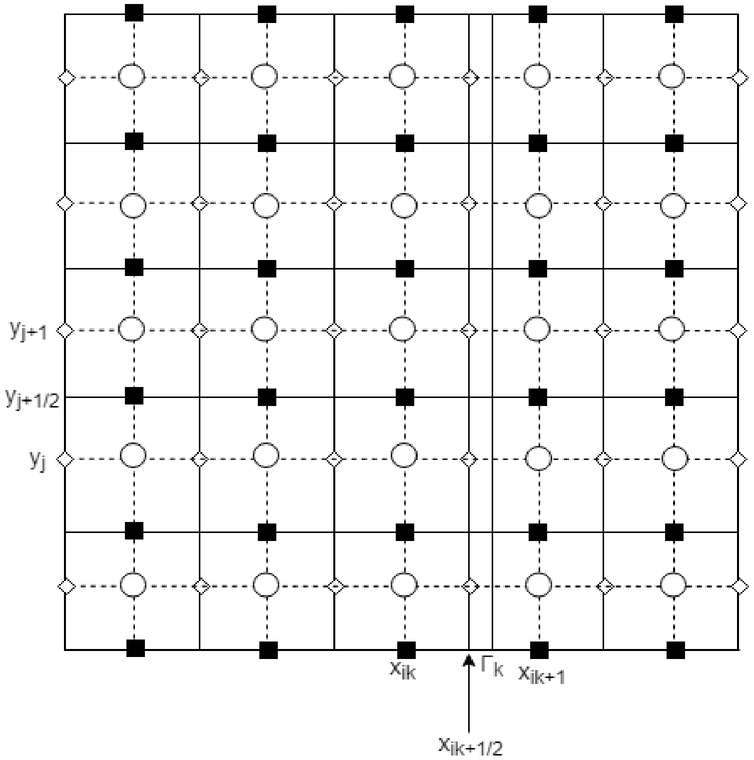

Figure 3.3: The staggered grid: $\circ, \diamond, \blacksquare$ for the points $(i,j), (i+\frac{1}{2},j), (i,j+\frac{1}{2})$

Define,

$$x_{i+\frac{1}{2}} = a + i\Delta x, \quad i = 0, 1, \ldots, N_x, \quad x_i = a + (i - \frac{1}{2})\Delta x, \quad i = 1, 2, \ldots, N_x,$$

$$y_{j+\frac{1}{2}} = c + j\Delta y, \quad j = 0, 1, \ldots, N_y, \quad y_j = c + (j - \frac{1}{2})\Delta y, \quad j = 1, 2, \ldots, N_y.$$

The time interval $(0, T]$ is discretized uniformly by

$$t^n = n\Delta t, \qquad n = 0, 1, 2, \ldots, N_t.$$

The nodes $(x_{i+\frac{1}{2}}, y_j), (x_i, y_{j+\frac{1}{2}})$ and (x_i, y_j) are nodes for the fluxes q^x, q^y and the solution u respectively. Denote $r_k^x = \beta_k \frac{\Delta t}{(\Delta x)^2}$, $r_k^y = \beta_k \frac{\Delta t}{(\Delta y)^2}$. For grid functions $W_{i,j}, W_{i+\frac{1}{2},j}, W_{i,j+\frac{1}{2}}$, define the space center difference operators as

$$\delta_x W_{i+\frac{1}{2},j} = \frac{W_{i+1,j} - W_{i,j}}{\Delta x}, \qquad \delta_x W_{i,j} = \frac{W_{i+\frac{1}{2},j} - W_{i-\frac{1}{2},j}}{\Delta x}$$

$$\delta_y W_{i,j+\frac{1}{2}} = \frac{W_{i,j+1} - W_{i,j}}{\Delta y}, \qquad \delta_y W_{i,j} = \frac{W_{i,j+\frac{1}{2}} - W_{i,j-\frac{1}{2}}}{\Delta y}.$$

On the staggered mesh, let $U^n_{i,j}$ denote the approximation to solution $u^n_{i,j} = u(x_i, y_j, t^n)$, $Q^{x,n}_{i+\frac{1}{2},j}$ to denote the approximation to flux $q^x(x_{i+\frac{1}{2}}, y_j, t^n)$ and $Q^{y,n}_{i,j+\frac{1}{2}}$ to the flux $q^y(x_i, y_{j+\frac{1}{2}}, t^n)$. The interface $x = \Gamma_k$ is not always at the vertical line of the mesh. A grid point x_i is called a regular point if it is not next to $x = \Gamma_k$ and x_{i_k}, $x_{i_{k+1}}$ are called as the irregular points if they are next to $x = \Gamma_k$ (see Fig. 3.3).

At the regular points, the central difference operator is applied to approximate the fluxes. However, at the irregular points, we propose the corrected flux difference operators.

Lemma 3. *Suppose that the interface $x = \Gamma_k$, locating at α_k, lies between (x_{i_k}, y_j) and (x_{i_k+1}, y_j). Then the following approximations hold*

$$q^{-,x}_{i_k+\frac{1}{2},j} = \frac{\beta_k u_{i_k+1,j} - \beta_{k-1} u_{i_k,j}}{\Delta x} + (\chi_x)_{i_k,j} + O(\Delta x^2) \tag{3.53}$$

$$q^{+,x}_{i_k+\frac{1}{2},j} = \frac{\beta_k u_{i_k+1,j} - \beta_{k-1} u_{i_k,j}}{\Delta x} + (\chi_x)_{i_k+1,j} + O(\Delta x^2) \tag{3.54}$$

where

$$(\chi_x)_{i_k,j} = -\frac{1}{\Delta x}\left([\beta u]_{\Gamma_k} + (x_{i_k+1}-\alpha_k)[\beta u_x]_{\Gamma_k} + \frac{1}{2}(x_{i_k+1}-\alpha_k)^2[\beta u_{xx}]_{\Gamma_k}\right)_j$$

$$(\chi_x)_{i_k+1,j} = -\frac{1}{\Delta x}\left([\beta u]_{\Gamma_k} + (x_{i_k}-\alpha_k)[\beta u_x]_{\Gamma_k} + \frac{1}{2}(x_{i_k}-\alpha_k)^2[\beta u_{xx}]_{\Gamma_k}\right)_j .$$

Remark 2. *If the interface $x = \Gamma_k$ lies at the midpoint of (x_{i_k}, y_j) and (x_{i_k+1}, y_j), i.e. $\alpha_k = \frac{x_{i_k}+x_{i_k+1}}{2}$, then the terms $(\chi_x)_{i_k,j}$ and $(\chi_x)_{i_k+1,j}$ will be*

$$\begin{aligned}(\chi_x)_{i_k,j} &= -\frac{1}{\Delta x}\left([\beta u]_{\Gamma_k} + \frac{\Delta x}{2}[\beta u_x]_{\Gamma_k} + \frac{\Delta x^2}{8}[\beta u_{xx}]_{\Gamma_k}\right)_j ,\\ (\chi_x)_{i_k+1,j} &= -\frac{1}{\Delta x}\left([\beta u]_{\Gamma_k} - \frac{\Delta x}{2}[\beta u_x]_{\Gamma_k} + \frac{\Delta x^2}{8}[\beta u_{xx}]_{\Gamma_k}\right)_j .\end{aligned} \tag{3.55}$$

At the irregular points, the corrected approximate fluxes are defined as that

$$Q^{-,x}_{i_k+\frac{1}{2},j} = \frac{\beta_k U_{i_k+1,j} - \beta_{k-1}U_{i_k,j}}{\Delta x} + (\bar{\chi}_x)_{i_k,j} \tag{3.56}$$

$$Q^{+,x}_{i_k+\frac{1}{2},j} = \frac{\beta_k U_{i_k+1,j} - \beta_{k-1}U_{i_k,j}}{\Delta x} + (\bar{\chi}_x)_{i_k+1,j} \tag{3.57}$$

and the corrections $(\chi_x)_{i_k,j}$ and $(\chi_x)_{i_k+1,j}$ are defined by

$$
\begin{aligned}
(\bar{\chi}_x)_{i_k,j} &= -\frac{1}{\Delta x}\Big(\frac{1}{2}(\beta_k+\beta_{k-1})\phi_{k,j}+\frac{1}{2}(\beta_k-\beta_{k-1})(E^-_{\Gamma_k}(U_{\cdot,j})+E^+_{\Gamma_k}(U_{\cdot,j})) \\
&\quad +(x_{i_k+1}-\alpha_k)\psi_{k,j}+\frac{1}{2}(x_{i_k+1}-\alpha_k)^2(\phi^{n+1}_{k_t,j}-[f^{n+1}]_{\Gamma_k,j})\Big), \qquad (3.58) \\
(\bar{\chi}_x)_{i_k+1,j} &= -\frac{1}{\Delta x}\Big(\frac{1}{2}(\beta_k+\beta_{k-1})\phi_{k,j}+\frac{1}{2}(\beta_k-\beta_{k-1})(E^-_{\Gamma_k}(U_{\cdot,j})+E^+_{\Gamma_k}(U_{\cdot,j})) \\
&\quad +(x_{i_k}-\alpha_k)\psi_{k,j}+\frac{1}{2}(x_{i_k}-\alpha_k)^2(\phi_{k_t,j}-[f]_{\Gamma_k},j)\Big), \qquad (3.59)
\end{aligned}
$$

where extrapolation $E^-_{\Gamma_k}(U_{\cdot,j})$ is explicitly evaluated by the previous time level values U_{i_k-2}, U_{i_k-1} and U_{i_k} and extrapolation $E^+_{\Gamma_k}(U_{\cdot,j})$ is explicitly evaluated using the previous time level values U_{i_k+1}, U_{i_k+2} and U_{i_k+3}.

Thus, based on these notations and with $f = f_1 + f_2$, for example, $f_1 = f_2 = \frac{1}{2}f$, we propose the mass-preserving splitting solution-flux scheme for two dimensional multi-layer interface parabolic equation as:

Stage I:

$$\frac{U^*_{i,j}-U^n_{i,j}}{\Delta t}-\delta_x Q^{x,*}_{i,j} = {f_1}^{n+1}_{i,j}, \qquad (x_i, y_j) \in \Omega_k \tag{3.60}$$

for the regular points, x_i

$$Q^{x,*}_{i+\frac{1}{2},j} = \beta_k \delta_x U^*_{i+\frac{1}{2},j}, \qquad (x_{i+\frac{1}{2}}, y_j) \in \Omega_k \tag{3.61}$$

and for the irregular points x_{i_k}, x_{i_k+1}, the points next to Γ_k,

$$Q^{-,x,*}_{i_k+\frac{1}{2},j} = \frac{\beta_k U^*_{i_k+1,j} - \beta_{k-1} U^*_{i_k,j}}{\Delta x} + (\bar{\chi}_x)^{n+1}_{i_k,j} \tag{3.62}$$

$$Q^{+,x,*}_{i_k+\frac{1}{2},j} = \frac{\beta_k U^*_{i_k+1,j} - \beta_{k-1} U^*_{i_k,j}}{\Delta x} + (\bar{\chi}_x)^{n+1}_{i_k+1,j}. \tag{3.63}$$

When the interface $x = \Gamma_k$ is not located at the middle line of $x = x_{i_k}$ and $x = x_{i_k+1}$, i.e. $\alpha_k \neq x_{i_k+\frac{1}{2}}$, then at the irregular points x_{i_k} and x_{i_k+1}, (3.60) is defined as

$$\frac{U^*_{i_k,j} - U^n_{i_k,j}}{\Delta t} - \delta_x Q^{x,*}_{i_k,j} = {f_1}^{n+1}_{i_k,j} + R^{n+1}_{i_k,j}, \qquad (x_{i_k}, y_j) \in \Omega_k \tag{3.64}$$

$$\frac{U^*_{i_k+1,j} - U^n_{i_k+1,j}}{\Delta t} - \delta_x Q^{x,*}_{i_k+1,j} = {f_1}^{n+1}_{i_k+1} + R^{n+1}_{i_k+1,j}, \qquad (x_{i_k+1}, y_j) \in \Omega_{k+1} \tag{3.65}$$

where $R^{n+1}_{i_k,j} = -\frac{1}{2\Delta x}\left(x_{i_k} - \alpha_k\right)^2 (\phi^{n+1}_{kt,j} - [f^{n+1}]_{\Gamma_k,j})$ and $R^{n+1}_{i_k+1,j} = \frac{1}{2\Delta x}\left(x_{i_k+1} - \alpha_k\right)^2 (\phi^{n+1}_{kt,j}$ $-[f^{n+1}]_{\Gamma_k,j})$.

Stage II:

$$\frac{U^{n+1}_{i,j} - U^*_{i,j}}{\Delta t} - \delta_y Q^{y,n+1}_{i,j} = {f_2}^{n+1}_{i,j}, \qquad (x_i, y_j) \in \Omega_k \tag{3.66}$$

$$Q^{y,n+1}_{i,j+\frac{1}{2}} = \beta_k \delta_y U^{n+1}_{i,j+\frac{1}{2}}, \qquad (x_i, y_{j+\frac{1}{2}}) \in \Omega_k. \tag{3.67}$$

The boundary conditions are provided by

$$Q^{x,*}_{\frac{1}{2},j} = g^{n+1}_{a,j}, \quad Q^{x,*}_{I+\frac{1}{2},j} = g^{n+1}_{b,j}, \qquad (x_{\frac{1}{2}}, y_j), (x_{I+\frac{1}{2}}, y_j) \in \partial\Omega \tag{3.68}$$

$$Q^{y,n+1}_{i,\frac{1}{2}} = h^{n+1}_{i,c}, \quad Q^{y,n+1}_{i,J+\frac{1}{2}} = h^{n+1}_{i,d}, \qquad (x_i, y_{\frac{1}{2}}), (x_i, y_{J+\frac{1}{2}}) \in \partial\Omega \tag{3.69}$$

and the initial values are given by

$$U^0_{i,j} = U_0(x_i, y_j), \qquad (x_i, y_j) \in \Omega_k. \tag{3.70}$$

3.3.2 The discrete mass conservation in 2D

We analyze the mass conservation in the discrete form for the two dimensional mass-preserving solution-flux scheme.

Theorem 4. *Scheme (3.60)-(3.70) satisfies mass conservation, i.e.*

$$\begin{aligned}\sum_{i=1}^{N_x}\sum_{j=1}^{N_y} U^{n+1}_{i,j}\Delta x\Delta y + \sum_{k=1}^{m}\sum_{s=0}^{n}\sum_{j=1}^{N_y}\psi^{s+1}_{k,j}\Delta y\Delta t = \sum_{i=1}^{N_x}\sum_{j=1}^{N_y} U^0_{i,j}\Delta x\Delta y + \\ \sum_{s=0}^{n}\Big(\sum_{i=1}^{N_x}\sum_{j=1}^{N_y} f^{s+1}_{i,j}\Delta x\Delta y + \sum_{i=1}^{N_x}(h^{s+1}_{i,d} - h^{s+1}_{i,c})\Delta x + \sum_{j=1}^{N_y}(g^{s+1}_{b,j} - g^{s+1}_{a,j})\Delta y\Big)\Delta t.\end{aligned} \tag{3.71}$$

Proof: If nodes $(x_{i_k+\frac{1}{2}}, y_j), k = 1, 2, \ldots, m$, are located at the interface $x = \Gamma_k$, then multiplying by $\Delta x\Delta y$ to equation (3.60) and summing i, j from 1 to N_x, N_y, we can have

$$\sum_{i=1}^{N_x}\sum_{j=1}^{N_y}\frac{U^*_{i,j} - U^n_{i,j}}{\Delta t}\Delta x\Delta y = \sum_{i=1}^{N_x}\sum_{j=1}^{N_y}\delta_x Q^{x,*}_{i,j}\Delta x\Delta y + \sum_{i=1}^{N_x}\sum_{j=1}^{N_y}{f_1}^{n+1}_{i,j}\Delta x\Delta y \tag{3.72}$$

But if there are points $x_{i_l+\frac{1}{2}} \neq \Gamma_l$, $l = 1, 2, \ldots, m_1$, then multiplying by $\Delta x\Delta y$ to equation (3.60) and equations (3.64)(3.65), and summing i, j from 1 to N_x, N_y, we get

$$\begin{aligned}\sum_{i=1}^{N_x}\sum_{j=1}^{N_y}\frac{U^*_{i,j}-U^n_{i,j}}{\Delta t}\Delta x\Delta y &= \sum_{i=1}^{N_x}\sum_{j=1}^{N_y}\delta_x Q^{x,*}_{i,j}\Delta x\Delta y+\sum_{i=1}^{N_x}\sum_{j=1}^{N_y}{f_1}^{n+1}_{i,j}\Delta x\Delta y\\ &\quad+\sum_{l=1}^{m_1}\sum_{j=1}^{N_y}\frac{1}{2}\left(x_{i_l+1}+x_{i_l}-2\alpha_l\right)\left(\phi_{lt}-[f^{n+1}]_{\Gamma_l}\right)_j\Delta y.\end{aligned} \tag{3.73}$$

Noting that $Q^{x,*}_{\frac{1}{2},j}=g^{n+1}_{a,j}$ and $Q^{x,*}_{I+\frac{1}{2},j}=g^{n+1}_{b,j}$, we can obtain

$$\sum_{i=1}^{N_x}\sum_{j=1}^{N_y}\delta_x Q^{x,*}_{i,j}\Delta x\Delta y=\sum_{k=1}^{m}\sum_{j=1}^{N_y}\frac{Q^{-,x,*}_{i_k+\frac{1}{2},j}-Q^{+,x,*}_{i_k+\frac{1}{2},j}}{\Delta x}\Delta x\Delta y+\sum_{j=1}^{N_y}\left(g^{n+1}_{b,j}-g^{n+1}_{a,j}\right)\Delta y \tag{3.74}$$

If all node $(x_{i_k+\frac{1}{2}}, y_j)$, $k = 1, 2, \ldots, m$, are located on the interfaces $x = \Gamma_k$, $k = 1, 2, \ldots, m$, from Lemma 3, we can further have

$$\sum_{i=1}^{N_x}\sum_{j=1}^{N_y}\delta_x Q^{x,*}_{i,j}\Delta x\Delta y=-\sum_{j=1}^{N_y}\sum_{k=1}^{m}\psi^{n+1}_{k,j}\Delta y+\sum_{j=1}^{N_y}\left(g^{n+1}_{b,j}-g^{n+1}_{a,j}\right)\Delta y. \tag{3.75}$$

If there are points $x_{i_l+\frac{1}{2}}$, $l = 1, 2, \ldots, m_1$, are not located on interfaces $x \neq \Gamma_l$, $l = 1, 2, \ldots, m_1$, then from Lemma 3 we can further get

$$\begin{aligned}\sum_{i=1}^{N_x}\sum_{j=1}^{N_y}\delta_x Q^{x,*}_{i,j}\Delta x\Delta y+\sum_{l=1}^{m_1}\sum_{j=1}^{N_y}\frac{1}{2}\left(x_{i_l+1}+x_{i_l}-2\alpha_l\right)\left(\phi_{lt}-[f^{n+1}]_{\Gamma_l}\right)_j\Delta y\\ =-\sum_{j=1}^{N_y}\sum_{k=1}^{m}\psi^{n+1}_{k,j}\Delta y+\sum_{j=1}^{N_y}\left(g^{n+1}_{b,j}-g^{n+1}_{a,j}\right)\Delta y.\end{aligned} \tag{3.76}$$

Thus, from (3.72) (3.75) and (3.73)(3.76), we have

$$\begin{aligned}\sum_{i=1}^{N_x}\sum_{j=1}^{N_y}\frac{U_{i,j}^{*}-U_{i,j}^{n}}{\Delta t}\Delta x\Delta y =&\sum_{i=1}^{N_x}\sum_{j=1}^{N_y}{f_1}_{i,j}^{n+1}\Delta x\Delta y\\ &-\sum_{j=1}^{N_y}\sum_{k=1}^{m}\psi_{k,j}^{n+1}\Delta y+\sum_{j=1}^{N_y}\left(g_{b,j}^{n+1}-g_{a,j}^{n+1}\right)\Delta y.\end{aligned}\tag{3.77}$$

Similarly, multiplying by $\Delta x\Delta y$ to equation (3.66) and summing i, j from 1 to N_x, N_y, we can have

$$\sum_{i=1}^{N_x}\sum_{j=1}^{N_y}\frac{U_{i,j}^{n+1}-U_{i,j}^{*}}{\Delta t}\Delta x\Delta y=\sum_{i=1}^{N_x}\sum_{j=1}^{N_y}\delta_y Q_{i,j}^{y,n+1}\Delta x\Delta y+\sum_{i=1}^{N_x}\sum_{j=1}^{N_y}{f_2}_{i,j}^{n+1}\Delta x\Delta y.\tag{3.78}$$

Using $Q_{i,\frac{1}{2}}^{y,n+1}=h_{i,c}^{n+1}$ and $Q_{i,N_y+\frac{1}{2}}^{y,n+1}=h_{i,d}^{n+1}$ and equation (3.67), we have

$$\sum_{i=1}^{N_x}\sum_{j=1}^{N_y}\delta_y Q_{i,j}^{y,n+1}\Delta x\Delta y=\sum_{i=1}^{N_x}\left(h_{i,d}^{n+1}-h_{i,c}^{n+1}\right)\Delta x.\tag{3.79}$$

Thus, we can get

$$\sum_{i=1}^{N_x}\sum_{j=1}^{N_y}\frac{U_{i,j}^{n+1}-U_{i,j}^{*}}{\Delta t}\Delta x\Delta y=\sum_{i=1}^{N_x}\sum_{j=1}^{N_y}{f_2}_{i,j}^{n+1}\Delta x\Delta y+\sum_{i=1}^{N_x}\left(h_{i,d}^{n+1}-h_{i,c}^{n+1}\right)\Delta x.\tag{3.80}$$

From equations (3.77)(3.80), it follows the theorem.

3.4 Numerical Experiments

In this section, we will conduct a number of numerical experiments to investigate the accuracy, mass conservation and stability of our proposed scheme for solving multi-layer interface parabolic problems. Piece-wisely defined analytical solutions will be constructed in examples with interfaces. The initial values and Neumann boundary conditions are chosen according the analytical solutions in all examples.

3.4.1 One dimensional case

Let $u(x, t^{n+1})$ be the exact solution of problem and U_i^{n+1} be the approximation solution, then we compute errors in discrete norms as

$$Err_{l_2} = (\sum_i \Delta x \left(u(x_i, t^{n+1}) - U_i^{n+1}\right)^2)^{\frac{1}{2}}, \quad Err_{l_\infty} = \max_i |u(x_i, t^{n+1}) - U_i^{n+1}|.$$

The order of convergence in space is calculated by

$$log\left(\frac{Err_{l_r,\Delta x_1}}{Err_{l_r,\Delta x_2}}\right)\left[log\left(\frac{\Delta x_1}{\Delta x_2}\right)\right]^{-1}, \qquad r = 2, \infty$$

when very small time step size Δt is taken in computation. Similarly, the order of convergence in time can be calculated. And mass as

$$
\begin{aligned}
Mass_n &= \sum_{i=1}^{N_x} U_i^n \Delta x + \Delta t \sum_{l=1}^{n} \psi^l - \Delta t \sum_{l=1}^{n} \sum_{i=1}^{N_x} f_i^l \Delta x - \Delta t \sum_{l=1}^{n} \left(g_b^l - g_a^l \right), \\
Mass_0 &= \sum_{i=1}^{N_x} U_i^0 \Delta x,
\end{aligned}
$$

and the error of mass is defined as $Mass - Error = |Mass_n - Mass_0|$, where Δx is the space step size and Δt is the time step size.

Example 3.1. We first consider the interface parabolic equation with zero-jump interface conditions, where at the interface point $\Gamma : x = 0.5$ in domain $\Omega = [0, 1]$, the jump conditions at $x = 0.5$ are $[u]_\Gamma = 0, [\beta u_x]_\Gamma = 0$, and the piecewise diffusion coefficients are β_1 for $x \in [0, 0.5)$ and β_2 for $x \in (0.5, 1]$ respectively.

The analytical solution is designed to be

$$
u(x,t) = \begin{cases} x^8 e^{-t} & \text{if } x \le 0.5 \\ \frac{1}{2}\left(\frac{1}{256} + x^8\right) e^{-t} & \text{if } x > 0.5 \end{cases}
$$

The right side function is then given by

$$
f(x,t) = \begin{cases} -\left(x^8 + 56\beta_1 x^6\right) e^{-t} & \text{if } x \le 0.5 \\ -\frac{1}{2}\left(\frac{1}{256} + x^8 + 56\beta_2 x^6\right) e^{-t} & \text{if } x > 0.5 \end{cases}
$$

Table 3.1: Errors and orders in space step size for the problem of Example 3.1

(a) Space order convergence for the problem with $\beta_2 = 2$, $\beta_1 = 1$, $\Delta t = 10^{-5}$, $T = 2$

N_x	Err_{l_2}	Order	Err_{L_∞}	Order
25	1.935E-2	–	1.961E-2	–
50	4.843E-3	1.997	4.901E-3	2.000
100	1.213E-3	1.996	1.225E-3	1.999
200	3.051E-4	1.989	3.077E-4	1.991
400	7.610E-5	2.004	7.618E-5	2.019

(b) Space order convergence for the problem with $\beta_2 = 0.05$, $\beta_1 = 0.025$, $\Delta t = 10^{-5}$, $T = 1$

N_x	Err_{l_2}	Order	Err_{l_∞}	Order
25	4.364E-4	–	6.975E-4	–
50	1.058E-4	2.062	1.675E-4	2.058
75	4.899E-5	1.898	7.845E-5	1.871
100	2.597E-5	2.207	4.001E-5	2.340
150	1.159E-5	1.989	1.848E-5	1.905

Table 3.2: Errors and orders in time step size for the problem of Example 3.1

(a) Time order convergence for the problem with $\Delta x = \frac{1}{200}$, $\beta_2 = 2$, $\beta_1 = 1$, $T = 2$

Δt	Err_{l_2}	Order	Err_{l_∞}	Order
$\frac{1}{20}$	1.300E-3	–	2.824E-3	–
$\frac{1}{40}$	6.568E-4	0.985	1.423E-4	0.989
$\frac{1}{60}$	4.405E-4	0.986	9.516E-4	0.992
$\frac{1}{80}$	3.319E-4	0.983	7.154E-4	0.992
$\frac{1}{100}$	2.667E-4	0.981	5.634E-4	1.071

(b) Time order convergence for the problem with $\Delta x = \frac{1}{160}$, $\beta_2 = 0.05$, $\beta_1 = 0.025$, $T = 1$

Δt	Err_{l_2}	Order	Err_{l_∞}	Order
$\frac{1}{20}$	1.858E-3	–	6.434E-3	–
$\frac{1}{40}$	9.331E-4	0.993	3.232E-3	0.993
$\frac{1}{60}$	6.230E-4	0.996	2.158E-3	0.997
$\frac{1}{80}$	4.676E-4	0.997	1.619E-3	0.999
$\frac{1}{100}$	3.743E-4	0.998	1.295E-3	0.999

Table 3.3: Mass errors of problem of Example 3.1 with different time step Δt and space step $\Delta x = \frac{1}{N_x}$ and $\beta_2 = 0.05, \beta_1 = 0.025, T = 1$

$\Delta t \setminus N_x$	20	40	80	160	320
$\frac{1}{20}$	4.684E-17	1.5613E-17	5.2042E-18	1.5092E-16	8.1532E-17
$\frac{1}{40}$	1.3618E-16	5.1174E-17	5.8113E-17	7.3726E-17	5.1174E-17
$\frac{1}{60}$	1.5728E-18	9.7145E-17	3.8164E-16	1.8041E-16	8.1185E-16
$\frac{1}{80}$	3.3177E-16	1.5396E-16	9.5843E-17	1.1232E-16	1.7477E-16
$\frac{1}{100}$	2.7756E-16	6.9389E-17	8.3267E-17	8.3267E-16	3.8752E-16

We first examine the spatial accuracy. A small enough $\Delta t = 10^{-5}$ is taken so that the temporal error can be neglected in this example. The numerical errors of the proposed scheme with different mesh size and different diffusion coefficients are listed in Table 3.1(a) and Table 3.1(b). Numerical results achieve the second order of accuracy in space step size in both l_2 and l_∞ norms. For the temporal convergence, we take $\Delta x = \frac{1}{N_x}$ as $\frac{1}{200}$ and $\frac{1}{160}$ and numerical errors are generated by using different Δt as shown in Table 3.2(a) and Table 3.2(b). Numerical results confirm that the scheme is of first order convergence in time step size. Table 3.3 is performed to illustrate the errors of mass. From Table 3.3, the errors of mass reach the accuracy at least 10^{-15}, which show that it preserves mass over the whole domain Ω.

Example 3.2. We next consider an interface parabolic problem with interface jump conditions of solution and flux at interface. The interface Γ is defined at $x = \frac{\pi}{4}$ and the domain size is $\Omega = [0, \frac{\pi}{2}]$. The piecewise diffusion coefficients are chosen as β_1 for $x \in [0, \frac{\pi}{4})$ and β_2 for $x \in (\frac{\pi}{4}, \frac{\pi}{2}]$. The jump conditions are $[u]_\Gamma = \left(\sin(k\frac{\pi}{4}) - \cos(k\frac{\pi}{4})\right)\cos(t)$ and $[\beta u_x]_\Gamma = k\left(\beta_2\cos(k\frac{\pi}{4}) + \beta_1\sin(k\frac{\pi}{4})\right)\cos(t)$. The analytical solution is given as

$$u(x,t) = \begin{cases} \cos(kx)\ cos(t) & \text{if } x \le \frac{\pi}{4} \\ \sin(kx)\ cos(t) & \text{if } x > \frac{\pi}{4} \end{cases}$$

and the right side function is

$$f(x,t) = \begin{cases} (k^2\beta_1 \cos(t) - \sin(t))\cos(kx) & \text{if } x \leq \frac{\pi}{4} \\ \\ (k^2\beta_2 \cos(t) - \sin(t))\sin(kx) & \text{if } x > \frac{\pi}{4} \end{cases}$$

where the wavenumber is chosen as $k = 1$.

Table 3.4: Errors and orders in space step size for the problem of Example 3.2

(a) Space order convergence for the problem with $\beta_2 = 100, \beta_1 = 1, \Delta t = 10^{-5}, T = 1$

(b) Space order convergence for the problem with $\beta_2 = 1, \beta_1 = 15, \Delta t = 10^{-5}, T = 1$

N_x	Err_{l_2}	Order	Err_{l_∞}	Order	N_x	Err_{l_2}	Order	Err_{l_∞}	Order
20	1.241E-2	–	1.086E-2	–	20	1.968E-3	–	1.733E-3	–
40	3.118E-3	1.989	2.809E-3	1.989	40	4.972E-4	1.979	4.501E-4	1.925
60	1.404E-3	1.968	1.326E-3	1.852	60	2.258E-4	1.702	1.838E-4	1.838
80	8.101E-4	1.912	8.073E-4	1.724	80	1.315E-4	1.878	1.311E-4	1.699
100	5.200E-4	2.065	5.075E-4	2.079	100	8.454E-5	1.980	8.682E-5	1.845

Table 3.5: Errors and orders in time step size for the problem of Example 3.2

(a) Time order convergence for the problem with$\Delta x = \pi/640, \beta_2 = 1, \beta_1 = 100, T = 1$

(b) Time order convergence for the problem with $\Delta x = \pi/640, \beta_2 = 15, \beta_1 = 1, T = 1$

Δt	Err_{l_2}	Order	Err_{l_∞}	Order	Δt	Err_{l_2}	Order	Err_{l_∞}	Order
$\frac{1}{20}$	3.145E-1	–	3.433E-1	–	$\frac{1}{20}$	1.117E-1	–	1.245E-1	–
$\frac{1}{40}$	2.364E-1	0.665	2.497E-1	0.687	$\frac{1}{40}$	6.042E-2	0.924	6.59E-2	0.945
$\frac{1}{80}$	1.580E-1	0.752	1.605E-1	0.778	$\frac{1}{80}$	3.138E-2	0.963	3.378E-2	0.975
$\frac{1}{160}$	9.240E-2	0.850	9.168E-2	0.875	$\frac{1}{160}$	1.598E-2	0.982	1.709E-2	0.989
$\frac{1}{320}$	5.004E-2	0.923	4.870E-2	0.941	$\frac{1}{320}$	7.960E-3	1.004	8.487E-3	1.007

The spatial accuracy of Example 3.2 is studied in Tables 3.4(a) and 3.4(b) in different meshes. Two different diffusion coefficients β_1 and β_2 are considered. Small temporal

Table 3.6: Mass errors of the problem of Example 3.2 with different time step Δt and space step $\Delta x = \frac{\pi}{2N_x}$ and $\beta_2 = 1, \beta_1 = 15, T = 1$

$\Delta t \setminus N_x$	20	40	80	160
$\frac{1}{20}$	1.9539E-12	8.6991E-14	3.8187E-13	1.8479E-13
$\frac{1}{40}$	5.3342E-14	2.4920E-14	4.7601E-13	3.2325E-13
$\frac{1}{80}$	5.1348E-16	1.5936E-14	2.8370E-14	6.4832E-13
$\frac{1}{160}$	1.4159E-14	1.2617E-13	2.8604E-13	9.3786E-13
$\frac{1}{320}$	1.0607E-14	3.9028E-14	2.5752E-13	5.6792E-14

step size $\Delta t = 10^{-5}$ is used to check the spatial convergence rates of the proposed scheme (where $\Delta x = \frac{\pi}{2N_x}$). We can see that the spatial orders of convergence are two in both discrete L_2 and L_∞ norms even the problem has the time dependent interface jump conditions. Taking the uniformly spatial step size $\Delta x = \frac{\pi}{640}$, the orders of convergence in time step size are shown in Tables 3.5(a) and 3.5(b) by varying time step sizes. In this example, the temporal convergent pattern is a little lower than the previous example however as time step size refines it is of first order convergence in both discrete L_2 and L_∞ norms. Table 3.6 presents the errors of mass at time $T = 1$ for different space and time step sizes (where $\Delta x = \frac{\pi}{2N_x}$, which clearly shows that our scheme satisfies conservation of mass where the errors of mass have still reached within machine accuracy 10^{-13}.

Example 3.3. In this example, we consider the parabolic equation with two interface points. The domain is $\Omega = [0, \pi]$, where two interfaces $\Gamma_k, k = 1, 2$, are defined at $x = \frac{\pi}{4}$ and $x = \frac{\pi}{2}$. The piecewise diffusion coefficients are chosen as β_1 for $x < \frac{\pi}{4}$, β_2 for $\frac{\pi}{4} < x < \frac{\pi}{2}$ and β_3 for $x > \frac{\pi}{2}$. The jump conditions are $[u]_{\Gamma_1} = 0, [\beta u_x]_{\Gamma_1} = \frac{1}{\sqrt{2}}(\beta_1 + \beta_2)\cos(t)$

and $[u]_{\Gamma_2} = -\cos(t), [\beta u_x]_{\Gamma_2} = -\beta_3 \cos(t)$ at $\Gamma_1 : x = \frac{\pi}{4}$ and $\Gamma_2 : x = \frac{\pi}{2}$ respectively. The analytical solution of the two interface point problem is considered as

$$u(x,t) = \begin{cases} \cos(x)\ cos(t) & \text{if } x \le \frac{\pi}{4} \\ \sin(x)\ cos(t) & \text{if } \frac{\pi}{4} < x \le \frac{\pi}{2} \\ \cos(x)\ cos(t) & \text{if } x > \frac{\pi}{2} \end{cases}$$

The source term is then given by

$$f(x,t) = \begin{cases} (\beta_1 \cos(t) - \sin(t)) \cos(x) & \text{if } x \le \frac{\pi}{4} \\ (\beta_2 \cos(t) - \sin(t)) \sin(x) & \text{if } \frac{\pi}{4} < x \le \frac{\pi}{2} \\ (\beta_3 \cos(t) - \sin(t)) \cos(x) & \text{if } x > \frac{\pi}{2} \end{cases}$$

Table 3.7: Errors and orders in space step size for the problem of Example 3.3

(a) Space order convergence with $\beta_1 = 1, \beta_2 = 5, \beta_3 = 10, \Delta t = 10^{-5}, T = 1$

(b) Space order convergence with $\beta_1 = 10^2, \beta_2 = 20, \beta_3 = 1, \Delta t = 10^{-5}, T = 1$

N_x	Err_{l_2}	Order	Err_{l_∞}	Order	N_x	Err_{l_2}	Order	Err_{l_∞}	Order
20	3.088E-3	–	2.617E-3	–	20	4.415E-2	–	3.157E-2	–
40	7.741E-4	1.995	6.603E-4	1.982	40	1.104E-2	1.999	7.902E-3	1.997
80	1.940E-4	1.995	1.690E-4	1.954	80	2.773E-3	1.990	2.006E-3	1.969
120	8.677E-5	1.985	7.789E-5	1.910	120	1.244E-3	1.978	9.153E-4	1.935
160	4.852E-5	2.021	4.399E-5	1.986	160	7.012E-4	1.992	5.136E-4	2.008

Table 3.8: Errors and orders in time step size for the problem of Example 3.3

(a) Time order convergence with $\Delta x = \frac{\pi}{160}, \beta_1 = 1, \beta_2 = 5, \beta_3 = 10, T = 1$

Δt	Err_{l_2}	Order	Err_{l_∞}	Order
$\frac{1}{20}$	5.213E-2	–	6.009E-2	–
$\frac{1}{40}$	2.643E-2	0.986	3.035E-2	0.989
$\frac{1}{80}$	1.330E-2	0.994	1.526E-2	0.995
$\frac{1}{160}$	6.667E-3	0.998	7.657E-3	0.996
$\frac{1}{320}$	3.333E-3	1.000	3.842E-3	0.997

(b) Time order convergence with $\Delta x = \frac{\pi}{400}, \beta_1 = 100, \beta_2 = 20, \beta_3 = 1, T = 1$

Δt	Err_{l_2}	Order	Err_{l_∞}	Order
$\frac{1}{20}$	5.202E-2	–	6.008E-2	–
$\frac{1}{40}$	2.637E-2	0.986	3.034E-2	0.990
$\frac{1}{80}$	1.328E-2	0.993	1.524E-2	0.995
$\frac{1}{160}$	6.661E-3	0.997	7.641E-3	0.997
$\frac{1}{320}$	3.335E-3	0.999	3.826E-3	0.998

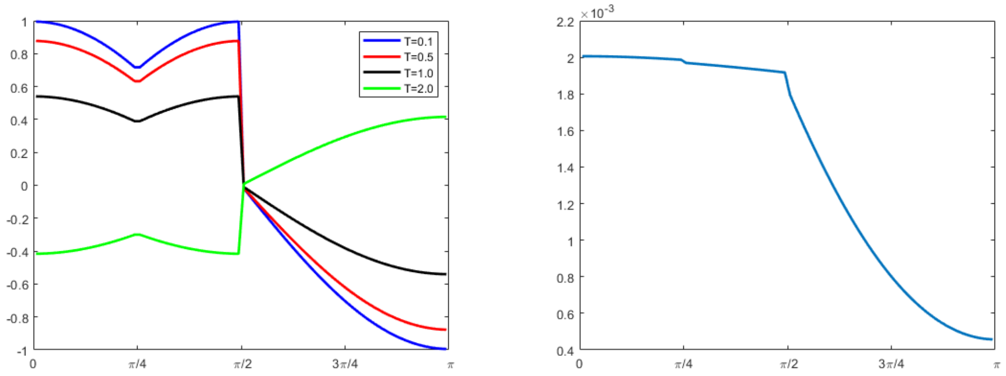

(a) Numerical solutions at different time levels

(b) Numerical error at $t = 1$

Figure 3.4: The piecewise diffusion coefficients $\beta_1 = 100, \beta_2 = 20$ and $\beta_3 = 1$ for Example 3.3

Table 3.9: Mass errors of the problem of Example 3.3 with different time step Δt and space and $\beta_1 = 1, \beta_2 = 5, \beta_3 = 10, T = 1$

$\Delta t \setminus N_x$	20	40	80	120	160
$\frac{1}{20}$	7.9936E-15	7.1054E-15	1.3323E-13	4.7073E-14	2.8155E-13
$\frac{1}{40}$	2.5757E-14	8.8818E-15	4.6185E-14	8.8817E-15	3.3751E-14
$\frac{1}{80}$	1.7764E-15	2.4869E-14	2.3093E-14	9.4147E-14	1.0925E-13
$\frac{1}{160}$	1.2434E-14	9.7699E-15	1.5099E-14	1.5365E-13	2.9310E-13
$\frac{1}{320}$	7.1942E-14	1.0125E-13	6.2172E-14	7.1054E-15	2.4869E-14

Three sub-domains are studied and different piecewise diffusion coefficients $(\beta_1, \beta_2, \beta_3)$ are taken. From Tables 3.7(a) and 3.7(b) (where $\Delta x = \frac{\pi}{2N_x}$), the second order of convergence in space step size is found in both discrete L_2 and L_∞ norms for the problem with the time-dependent jump conditions at two interface points. Varying time step sizes from $\frac{1}{20}$ to $\frac{1}{320}$, Tables 3.8(a) and 3.8(b) show the temporal convergence rate to be first order in both discrete L_2 and L_∞ norms. Fig. 3.4 shows numerical solutions at different time level and numerical error at $t = 1$. Table 3.9 presents the errors of mass with different space and time step sizes, from which we can see clearly that the scheme satisfies conservation of mass where mass errors have reached with accuracy of 10^{-13}.

Example 3.4: Further, we take three interface points problem with general interface jump conditions. The domain is $\Omega = [-\frac{1}{2}, \frac{1}{2}]$. The interfaces $\Gamma_k, k = 1, 2, 3$, are defined at $x = -\frac{1}{4}$, $x = 0$ and $x = \frac{1}{4}$, and four sub-domains are $\Omega_1 = (-\frac{1}{2}, -\frac{1}{4})$, $\Omega_2 = (-\frac{1}{4}, 0)$, $\Omega_3 = (0, \frac{1}{4})$ and $\Omega_4 = (\frac{1}{4}, \frac{1}{2})$. The piecewise diffusion coefficients are chosen as β_1 in sub-domain Ω_1 , β_2 in sub-domain Ω_2 , β_3 sub-domain Ω_3 and β_4 in sub-domain Ω_4. The interface jump conditions are $[u]_{\Gamma_1} = \left(\frac{3}{2\sqrt{2}} + \frac{1}{2}\right) e^t$, $[\beta u_x]_{\Gamma_1} = \pi \frac{\beta_2 - 2\beta_1}{2\sqrt{2}} e^t$ at $x = -\frac{1}{4}$, $[u]_{\Gamma_2} = -e^t, [\beta u_x]_{\Gamma_2} = \beta_3 e^t$ at $x = 0$ and $[u]_{\Gamma_3} = \left(\frac{3}{16} - \sin\left(\frac{1}{4}\right)\right) e^t, [\beta u_x]_{\Gamma_3} = \left(\frac{\beta_4}{2} - \beta_3 \cos\left(\frac{1}{4}\right)\right) e^t$ at $x = \frac{1}{4}$.

Three analytical solution is given as

$$u(x,t) = \begin{cases} \sin(\pi x)e^t & \text{if } x < -\frac{1}{4} \\ \frac{\cos(\pi x)+1}{2}e^t & \text{if } -\frac{1}{4} \leq x < 0 \\ \sin(x)e^t & \text{if } 0 \leq x < \frac{1}{4} \\ x(1-x)e^t & \text{if } x \geq \frac{1}{4} \end{cases}$$

and the right side function is given by

$$f(x,t) = \begin{cases} (1+\beta_1\pi^2)\sin(\pi x)e^t & \text{if } x < -\frac{1}{4} \\ \left[(1+\beta_2\pi^2)\cos(\pi x)+1\right]\frac{e^t}{2} & \text{if } -\frac{1}{4} \leq x < 0 \\ (1+\beta_3)\sin(x)e^t & \text{if } 0 \leq x < \frac{1}{4} \\ (2\beta_4 + x - x^2)\,e^t & \text{if } x \geq \frac{1}{4} \end{cases}$$

Table 3.10: Errors and orders in space step size for the problem of Example 3.4

(a) Space order convergence with$\beta_1 = 1, \beta_2 = 5, \beta_3 = 10, \beta_4 = 20, T = 1$

N_x	Err_{l_2}	Order	Err_{l_∞}	Order
20	6.004E-3	–	6.473E-3	–
40	1.499E-3	2.002	1.614E-3	2.006
80	3.746E-4	2.001	4.027E-4	2.004
160	9.355E-5	2.004	1.003E-4	2.007
320	2.335E-5	2.003	2.642E-5	1.974

(b) Space order convergence with$\beta_1 = 1, \beta_2 = 0.1, \beta_3 = 10^{-2}, \beta_4 = 10^{-3}, T = 1$

N_x	Err_{l_2}	Order	Err_{l_∞}	Order
20	5.291E-3	–	9.596E-3	–
40	1.314E-3	2.013	2.356E-3	2.036
80	3.278E-4	2.005	5.832E-4	2.020
160	8.191E-5	2.001	1.436E-4	2.031
320	1.869E-5	2.191	3.646E-5	1.968

Table 3.11: Errors and orders in time step size for the problem of Example 3.4

(a) Time order convergence for the problem with $\beta_1 = 1, \beta_2 = 5, \beta_3 = 10, \beta_4 = 20, T = 1$

Δt	Err_{l_2}	Order	Err_{l_∞}	Order
$\frac{1}{40}$	4.712E-2	–	8.453E-2	–
$\frac{1}{80}$	2.373E-2	0.993	4.254E-2	0.993
$\frac{1}{160}$	1.191E-2	0.996	2.134E-2	0.997
$\frac{1}{320}$	5.964E-3	0.998	1.069E-2	0.998
$\frac{1}{640}$	2.685E-3	1.111	5.153E-3	1.037

(b) Time order convergence for the problem with $\beta_1 = 1, \beta_2 = 0.1, \beta_3 = 10^{-2}, \beta_4 = 10^{-3}, T = 1$

Δt	Err_{l_2}	Order	Err_{l_∞}	Order
$\frac{1}{40}$	7.417E-2	–	1.678E-1	–
$\frac{1}{80}$	3.792E-2	0.978	8.633E-2	0.972
$\frac{1}{160}$	1.917E-2	0.989	4.379E-2	0.986
$\frac{1}{320}$	9.638E-3	0.994	2.205E-2	0.993
$\frac{1}{640}$	4.833E-3	0.997	1.106E-2	0.997

Table 3.12: Mass errors of the problem of Example 3.4 in different time step Δt and space step Δx and $\beta_1 = 1, \beta_2 = 5, \beta_3 = 10, \beta_4 = 20, T = 1$

$\Delta t \backslash \mathrm{N}_x$	20	40	80	160	320
$\frac{1}{20}$	1.0658E-14	7.1054E-15	1.5987E-13	4.2633E-14	1.8829E-13
$\frac{1}{40}$	4.6185E-14	5.3291E-14	5.6843E-14	5.7199E-13	7.8758E-13
$\frac{1}{80}$	7.1054E-15	7.1054E-15	6.3949E-14	5.6488E-13	8.7397E-13
$\frac{1}{160}$	1.2434E-16	1.9895E-15	1.4211E-14	2.1316E-14	2.2382E-13
$\frac{1}{320}$	7.1054E-15	1.7764E-13	1.8829E-13	8.5265E-13	2.0748E-13

The spatial errors and convergence orders are reported in Tables 3.10(a) and 3.10(b) for this three interface point problem (where $\Delta x = \frac{1}{N_x}$). The scheme clearly achieves second order in space step size in both discrete L_2 and L_∞ . The scheme delivers the first order of accuracy in time step size in Tables 3.11(a) and 3.11(b). Table 3.12 delivers the errors of mass at time $T = 1$ with different space and time step sizes. It is clear that our scheme satisfies conservation of mass and meets with machine accuracy of 10^{-13}. Fig. 3.5 shows the numerical solutions compared with exact solution of this three interface point parabolic equation.

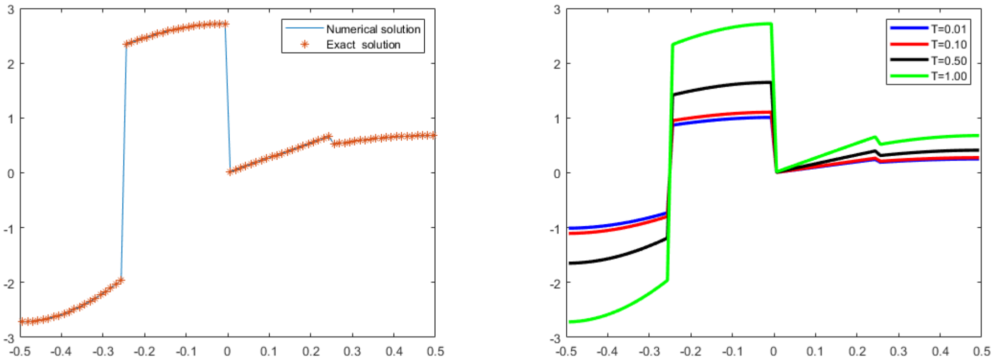

(a) Numerical solution and exact solution at $t = 1$ (b) Numerical solutions at different time levels

Figure 3.5: The piecewise diffusion coefficients $\beta_1 = 1, \beta_2 = 5, \beta_3 = 10$ and $\beta_4 = 20$ for Example 3.4.

3.4.2 Two dimensional case

In this subsection, we present numerical experiments of $2D$ multi-layer interface problems to illustrate the performance of our proposed scheme. Let $u(x, y, t^{n+1})$ be the exact solution and $U_{i,j}^{n+1}$ be the numerical solutions. The numerical errors in discrete norms are defined as

$$Err_{l_2} = \sqrt{\sum_{i,j} \left(u(x_i, y_j, t^n) - U_{i,j}^n\right)^2 \Delta x \Delta y}, \quad Err_{l_\infty} = \max_{i,j} |u(x_i, y_j, t^n) - U_{i,j}^n|.$$

The order of convergence in time are calculated by

$$log\left(\frac{Err_{l_r,\Delta t_1}}{Err_{l_r,\Delta t_2}}\right)\left[log\left(\frac{\Delta t_1}{\Delta t_2}\right)\right]^{-1}, \qquad r = 2, \infty$$

when very small space step size Δx and Δy are taken in computation. Similarly, the order of convergence in space can be calculated. The mass and error of mass are as

$$\begin{aligned}
Mass_n &= \sum_{i=1}^{N_x}\sum_{j=1}^{N_y} U_{i,j}^n \Delta x \Delta y - \sum_{l=1}^{n}\sum_{i=1}^{N_x}\sum_{j=1}^{N_y} f_{i,j}^l \Delta x \Delta y \Delta t + \sum_{k=1}^{r}\sum_{l=1}^{n}\sum_{j=1}^{N_y} \psi_{k,j}^n \Delta y \Delta t \\
&\quad - \sum_{l=1}^{n}\sum_{i=1}^{N_x} \left(h_{i,d}^l - h_{i,c}^l\right) \Delta x \Delta t - \sum_{l=1}^{n}\sum_{j=1}^{N_y} \left(g_{b,j}^l - g_{a,j}^l\right) \Delta y \Delta t, \\
Mass_0 &= \sum_{i=1}^{N_x}\sum_{j=1}^{N_y} U_{i,j}^0 \Delta x \Delta y
\end{aligned}$$

and $Error - Mass = |Mass_n - Mass_0|$, where $\Delta x, \Delta y$ are the space step sizes and Δt is the time step size.

Example 3.5. We consider the $2D$ parabolic equation with two interfaces $\Gamma_k, k = 1, 2$, and different interface jump conditions. The domain is $\Omega = [0, \pi] \times [0, \pi]$, where the interfaces are at $\Gamma_1 : x = \frac{\pi}{4}$ and $\Gamma_2 : x = \frac{\pi}{2}$. The piecewise diffusion coefficient is $\beta_1 = 1/160, \beta_2 = 1/10, \beta_3 = 1/100$ on each layer respectively. The interface conditions are $[u]_{\Gamma_1} = -\sin(\pi^2/4)\sin(\pi y)e^{-2\beta_1\pi^2 t}$, $[\beta u_x]_{\Gamma_1} = -\left[\pi\cos(\pi^2/2)\sin(\pi y)e^{-2\beta_1\pi^2 t} + 2\sin(y)e^{-5\beta_2 t}\right]$ at $x = \frac{\pi}{4}$, and $[u]_{\Gamma_2} = \sin(y)\left(e^{-5\beta_2 t} + e^{-2\beta_3 t}\right)$, $[\beta u_x]_{\Gamma_2} = 0$ at $x = \frac{\pi}{2}$. The exact solution is given as

$$u(x, y, t) = \begin{cases} \sin(\pi x)\sin(\pi y)e^{-2\beta_1\pi^2 t} & \text{if } x < \frac{\pi}{4} \\ \cos(2x)\sin(y)e^{-5\beta_2 t} & \text{if } \frac{\pi}{4} \le x < \frac{\pi}{2} \\ \sin(x)\sin(y)e^{-2\beta_3 t} & \text{if } x \ge \frac{\pi}{2} \end{cases}$$

and the right side function $f(x, y, t)$ is zero.

Table 3.13: Errors and convergence orders in space and time step sizes for the problem of Example 3.5 with $\beta_1 = 1/160, \beta_2 = 1/10, \beta_3 = 1/100, T = 1$ where $N_x = N_y$

(a) Space order convergence for the problem with $(\Delta x = \Delta y)$ and $\Delta t = 10^{-6}$

N_x	Err_{l_2}	Order	Err_{l_∞}	Order
40	1.097E-3	–	2.196E-3	–
60	4.981E-4	1.946	1.059E-3	1.799
80	2.821E-4	1.977	6.172E-4	1.878
100	1.809E-4	1.988	4.027E-4	1.914
120	1.258E-4	1.995	2.830E-4	1.935

(b) Time order convergence for the problem with $\Delta x = \Delta y = \frac{\pi}{320}$

Δt	Err_{l_2}	Order	Err_{l_∞}	Order
$\frac{1}{20}$	1.705E-2	–	3.733E-2	–
$\frac{1}{40}$	8.557E-3	0.996	1.843E-2	1.013
$\frac{1}{80}$	4.282E-3	0.999	9.143E-3	0.979
$\frac{1}{160}$	2.137E-3	1.002	4.538E-3	1.007
$\frac{1}{320}$	1.005E-3	1.005	2.245E-3	1.017

Table 3.14: Mass errors of the problem of Example 3.5 in different time step Δt and space step $\Delta x = \Delta y$ and $\beta_1 = 1/160, \beta_2 = 1/10, \beta_3 = 1/100, T = 1$

$\Delta t \setminus (N_x = N_y)$	20	40	80	160	320
$\frac{1}{20}$	2.7658E-13	8.1054E-13	1.1433E-14	3.2336E-13	1.0688E-12
$\frac{1}{40}$	6.1458E-13	1.5923E-14	7.8758E-13	1.0719E-14	5.6843E-13
$\frac{1}{80}$	4.1074E-14	5.9263E-14	6.3949E-14	5.6488E-13	8.7397E-13
$\frac{1}{160}$	3.2434E-13	9.9895E-14	4.2421E-14	6.0131E-13	7.5038E-12
$\frac{1}{320}$	5.1752E-14	7.6764E-13	1.9280E-12	6.6268E-13	2.0918E-13

We choose $\Delta x = \Delta y$ (where $\Delta x = \frac{1}{N_x}, \Delta y = \frac{1}{N_y}$ and $N_x = N_y$) and vary its value from $\frac{\pi}{40}$ to $\frac{\pi}{120}$ for checking the convergence rate in space step size where the small time step size is taking as $\Delta t = 10^{-6}$. Numerical errors in discrete norms and rate of convergence at time $T = 1$ are listed in Table 3.13 (a). It is clearly shown that our scheme is of second order convergence in discrete L_2 norm as well as discrete L_∞ norm. We then fix $\Delta x = \Delta y = \frac{\pi}{320}$ and use different time step size Δt, numerical errors and orders of convergence in time step size are shown in the Table 3.13 (b), which confirms that our scheme is of first order convergence in time step size. Table 3.14 further shows the

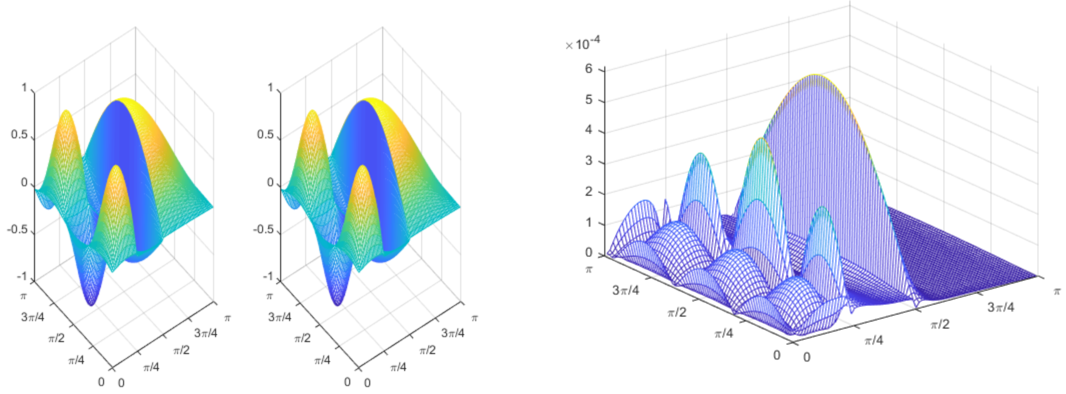

(a) Numerical solution (left) and exact solution (right) (b) Numerical error between exact and numerical solutions

Figure 3.6: The piecewise diffusion coefficients $\beta_1 = 1/160, \beta_2 = 1/10$ and $\beta_3 = 1/100$ for Example 3.5.

errors of mass with different space and time step sizes. From Table 3.14, we can see that mass errors reach around 10^{-13} which is close to machine accuracy for different time and space step size. Thus, it shows that the scheme preserves mass over the whole domain Ω. Finally, Fig. 3.6 shows the comparison of numerical solution and exact solution, and numerical errors at $t = 1$.

Example 3.6. We now consider interface parabolic equation of the diffusion process with large difference piecewise diffusion. The domain is $\Omega = [-1, 1] \times [-1, 1]$ with two interfaces $\Gamma_k, k = 1, 2$, which has $y-$ direction diffusion constant and is piecewise constant β_1, β_2 and β_3 along $x-$direction with large difference among $\beta_1 = 1, \beta_2 = 1000$ and $\beta_3 = 1$. The interface conditions are at Γ_1 : at $x = -\frac{1}{2}$ and at Γ_2 :$x = \frac{1}{2}$. The exact

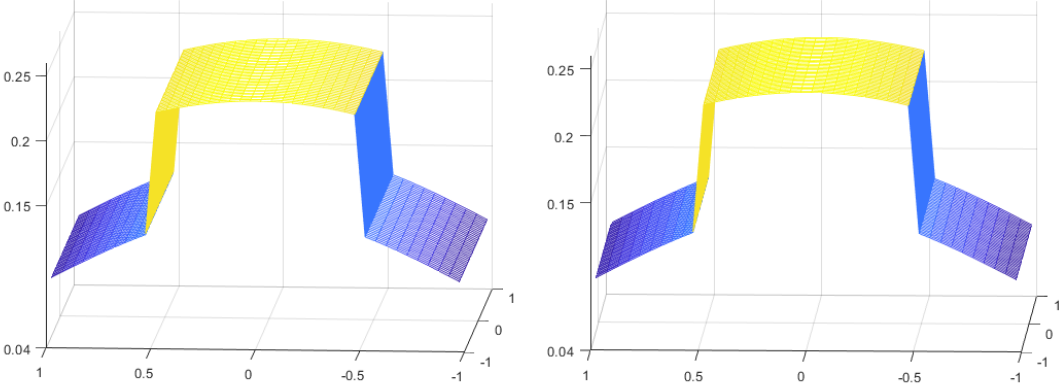

(a) Numerical Solution at $t = 0.1$ (b) Exact Solution at $t = 0.1$

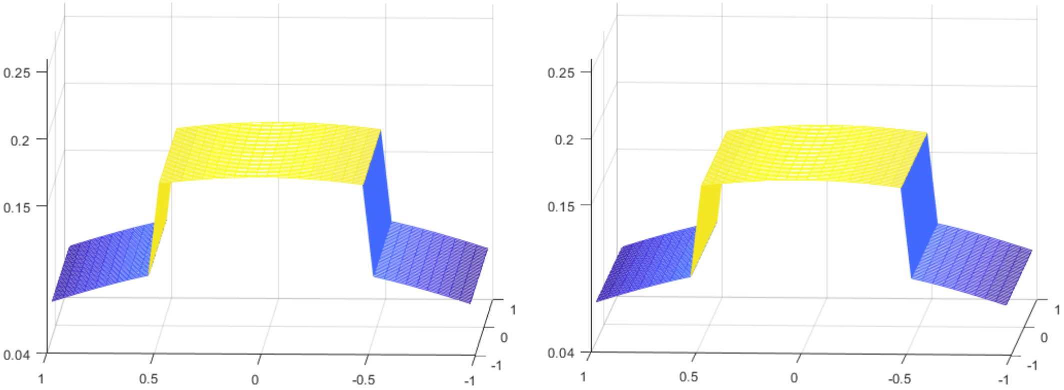

(c) Numerical Solution at $t = 0.5$ (d) Exact Solution at $t = 0.5$

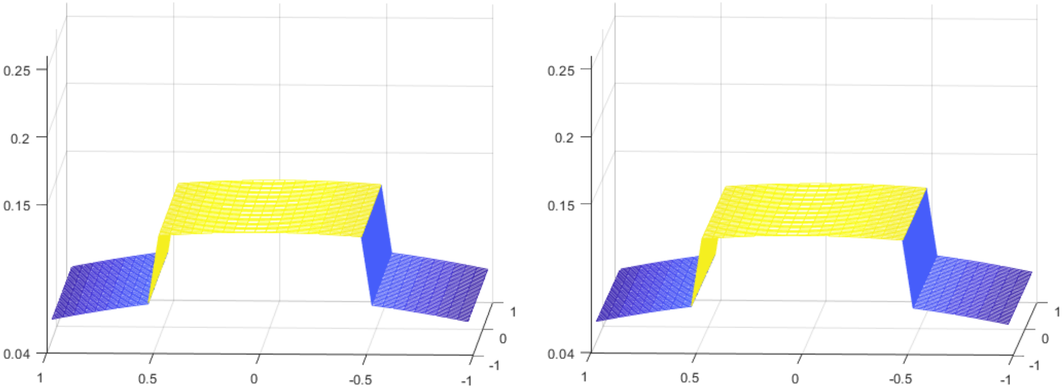

(e) Numerical Solution at $t = 1.0$ (f) Exact Solution at $t = 1.0$

Figure 3.7: The piecewise diffusion coefficients: $\beta_1 = 1, \beta_2 = 1000$ and $\beta_3 = 1$ and time step size $\Delta t = 10^{-5}$ and space step sizes $\Delta x = \Delta y = \frac{1}{40}$.

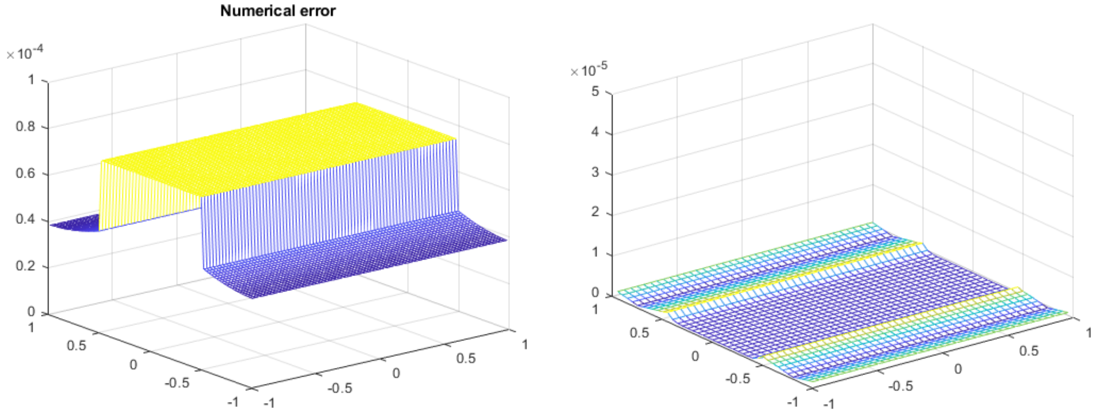

(a) $\beta_1 = 1, \beta_2 = 10^3$, $\beta_3 = 1$, $\Delta x = \Delta y = \frac{1}{40}$ (b) $\beta_1 = 0.1, \beta_2 = 10^{-3}$, $\beta_3 = 0.1$, $\Delta x = \Delta y = \frac{1}{20}$

Figure 3.8: Numerical errors with different piecewise diffusion coefficients values and step sizes space with $\Delta t = 10^{-5}$for the solutions of problems of Example 3.6 at $T = 1$.

solution is given as

$$u(x, y, t) = \begin{cases} 4\frac{e^{-\frac{x^2}{5(t+1)}}}{5\pi(t+1)} & \text{if } x < -\frac{1}{2} \\ \frac{e^{-\frac{x^2}{2(t+1)}}}{2\pi(t+1)} & \text{if } -\frac{1}{2} \leq x \leq \frac{1}{2} \\ 4\frac{e^{-\frac{x^2}{5(t+1)}}}{5\pi(t+1)} & \text{if } x > \frac{1}{2} \end{cases}$$

Numerical solutions and exact solution are shown in Fig. 3.7 (a) - (f), where space mesh sizes are $\Delta x = \Delta y = \frac{1}{40}$. Numerical errors of numerical solutions with different set of piecewise diffusion coefficients are shown in Fig 3.8 at $T = 1$ and it clearly shows the numerical errors are high accuracy. Table 3.15 shows that our scheme is of second order convergence in discrete L_2 norm as well as discrete L_∞ norm. Also, the mass errors of numerical solutions in the long time computing upto $T = 100$, where space step sizes are $\Delta x = \Delta y = \frac{1}{20}$ and time step size $\Delta t = 10^{-3}$, are shown in Fig. 3.9 by using different piecewise diffusion values. This clearly shows that the proposed scheme satisfies mass conservation over long time simulation.

Table 3.15: Errors and convergence orders in space for the problem of Example 3.6 with $\beta_1 = 1, \beta_2 = 1000, \beta_3 = 1, T = 1, \Delta t = 10^{-5}$ where $N_x = N_y$

N_x	Err_{l_2}	Order	Err_{l_∞}	Order
20	1.806E-3	–	9.786E-4	–
40	4.544E-4	1.987	2.867E-4	1.706
80	1.196E-4	1.899	7.440E-5	1.927
100	8.030E-5	1.906	5.273E-5	1.806
120	5.436E-5	2.052	3.753E-5	1.951

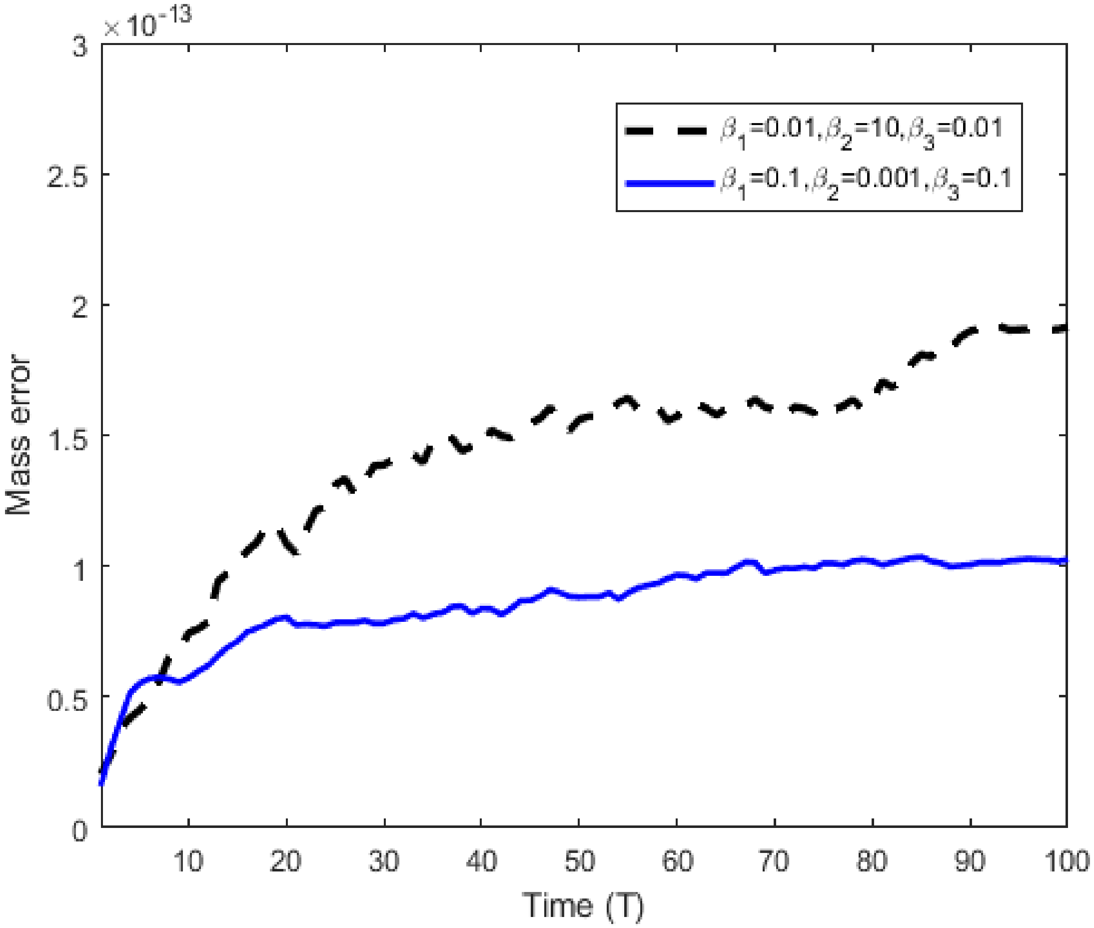

Figure 3.9: Long time mass error plot with $\Delta x = \Delta y = \frac{1}{20}, \Delta t = 10^{-3}$

Example 3.7. Finally, we compute the heat propagation in the multi-layer media. The domain is $\Omega = [0,1]\times[0,1]$ with three layers of $\Omega_1 = [0,\frac{2}{5})\times[0,1]$, $\Omega_2 = [\frac{2}{5},\frac{3}{5})\times[0,1]$ and $\Omega_3 = (\frac{3}{5},1]\times[0,1]$. The piecewise diffusion coefficient is as $\beta_1 = 10^{-2}, \beta_2 = 10^{-1}$ and $\beta_3 = 10^{-2}$ on these three layers respectively, and the right side function is zero. We consider four different cases of interface jump conditions at the interfaces $x = \frac{2}{5}$ and $x = \frac{3}{5}$. The first case is that the jump conditions are continuous along interfaces, i.e. $[u]_{x=\frac{2}{5}} = [\beta u_x]_{x=\frac{2}{5}} = [u]_{x=\frac{3}{5}} = [\beta u_x]_{x=\frac{3}{5}} = 0$. In this case, the initial heat distribution is given as 1 at 4-specific points in sub-domains Ω_1 and Ω_3 and 0 for all other points in Ω_1 and Ω_3 as well as in Ω_2. The other three cases are that the no-zero jump conditions $[u]_\Gamma$ and $[\beta u_x]_\Gamma$ are provided at interfaces, and the initial heat distribution is given as 1 at four specific points in sub-domains Ω_1 and Ω_3 and 0 for other points in Ω_1 and Ω_3 but the initial heat distribution is 10^{-3} in all points of sub-domainΩ_2. In computation, we take time step size $\Delta t = 10^{-5}$ and space step sizes $\Delta x = \Delta y = \frac{1}{100}$.

Figs. 3.10 - 3.13 show the heat distribution at different time for the four cases with different solution and flux jump conditions at the interfaces, where Figs. 3.10 - 3.13 (a)(c)(e) are the contours of heat distribution and Fig. 3.10 - 3.13 (b)(d)(f) are the plots of heat distribution along line $y = \frac{1}{5}$. From the figures, we can see clearly how the heat propagates and how the interface conditions affect the propagation of heat cross the interfaces $x = \frac{2}{5}$ and $x = \frac{3}{5}$. The highest heats at initial gradually decrease and propagate smoothly in all directions as time increases. But, the shapes of heat distribution oscillate when heat propagation crosses the interfaces of layers. We can see that the mass-preserving solution- flux scheme works excellently for the multi-layer heat

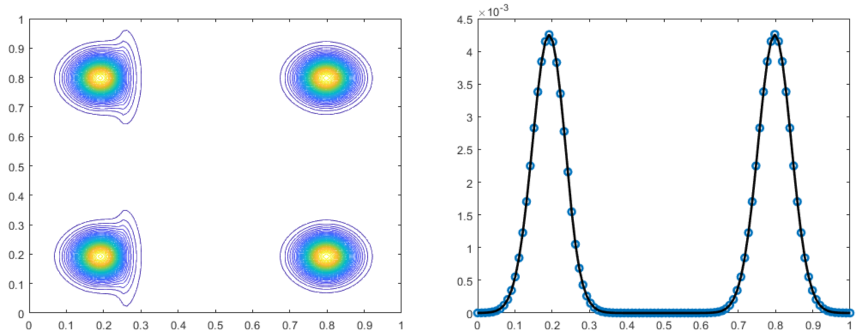

(a) Contour at $t = 0.1$ (b) Plot at $t = 0.1$

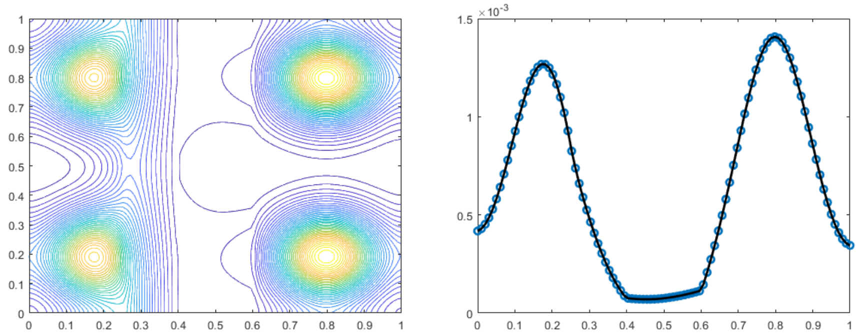

(c) Contour at $t = 0.5$ (d) Plot at $t = 0.5$

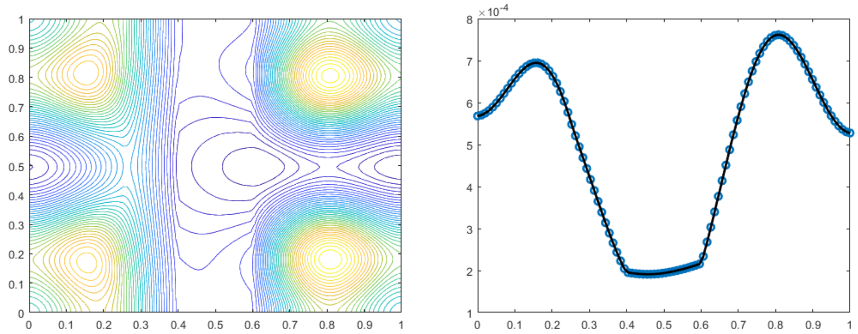

(e) Contour at $t = 1.0$ (f) Plot at $t = 1.0$

Figure 3.10: Heat distribution of Case 1: Both zero solution and flux jump conditions at both interfaces, $[u] = 0,\ [\beta u_x] = 0$.

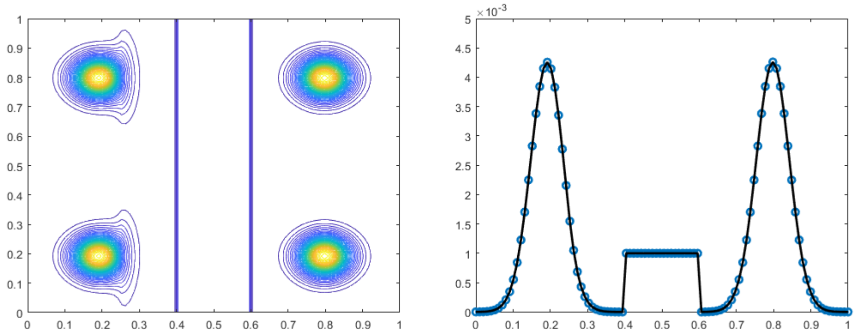

(a) Contour at $t = 0.1$ (b) Plot at $t = 0.1$

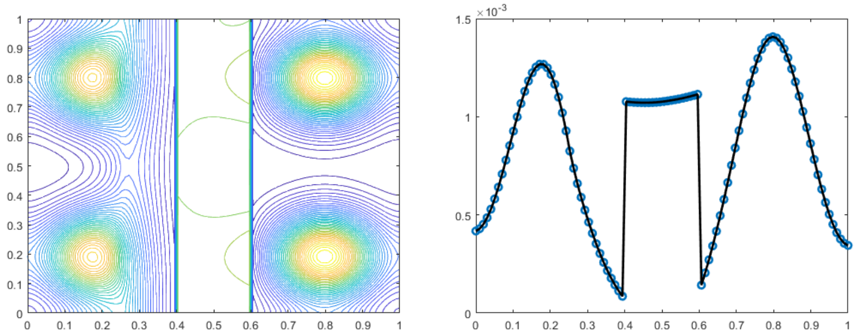

(c) Contour at $t = 0.5$ (d) Plot at $t = 0.5$

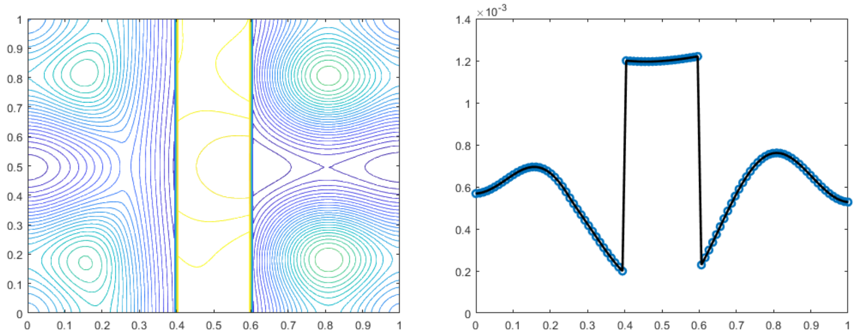

(e) Contour at $t = 1.0$ (f) Plot at $t = 1.0$

Figure 3.11: Heat distribution of Case 2: Two solution jump conditions $[u]_{x=\frac{2}{5}} = \frac{(1+0.01t)}{10^3}$ and $[u]_{x=\frac{3}{5}} = -\frac{(1+0.01t)}{10^3}$, but two flux jump conditions are zero, $[\beta u_x] = 0$.

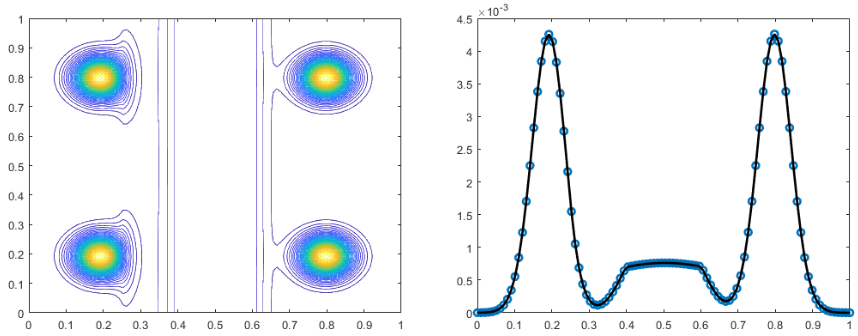

(a) Contour at $t = 0.1$ (b) Plot at $t = 0.1$

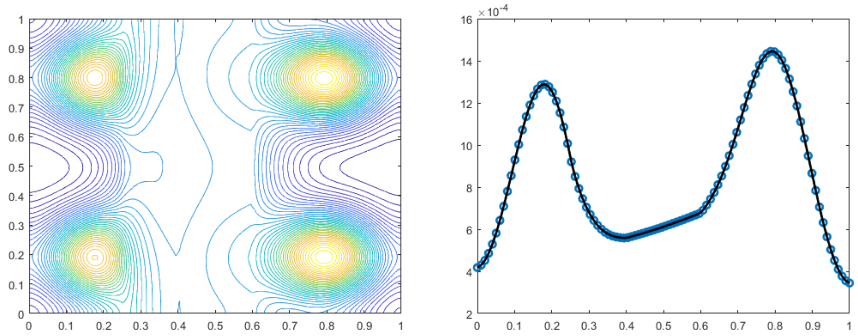

(c) Contour at $t = 0.5$ (d) Plot at $t = 0.5$

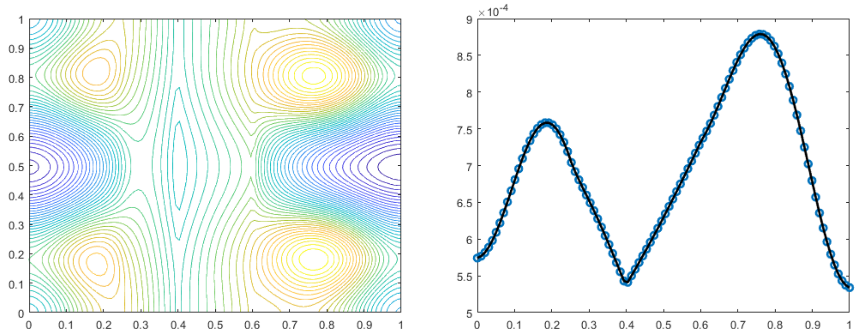

(e) Contour at $t = 1.0$ (f) Plot at $t = 1.0$

Figure 3.12: Heat distribution of Case 3: Two solution jump conditions are zero $[u] = 0$, but two flux jump conditions are $[\beta u_x]_{x=\frac{2}{5}} = \frac{t}{10^4}$ and $[\beta u_x]_{x=\frac{3}{5}} = -\frac{t}{10^4}$.

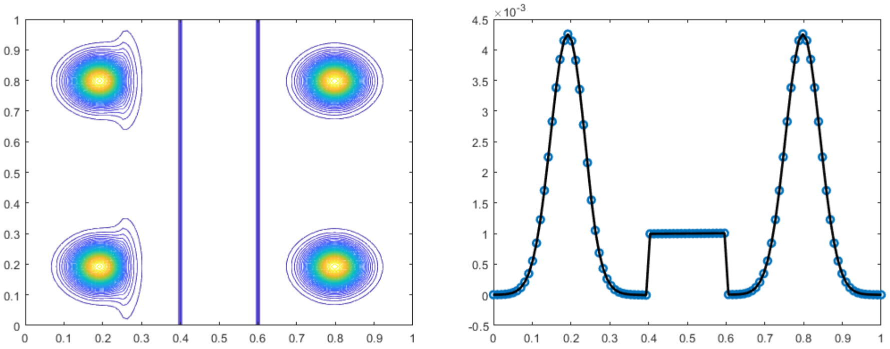

(a) Contour at $t = 0.1$ (b) Plot at $t = 0.1$

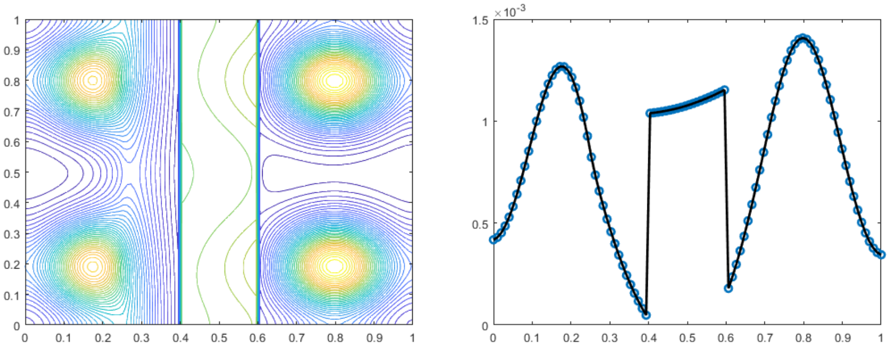

(c) Contour at $t = 0.5$ (d) Plot at $t = 0.5$

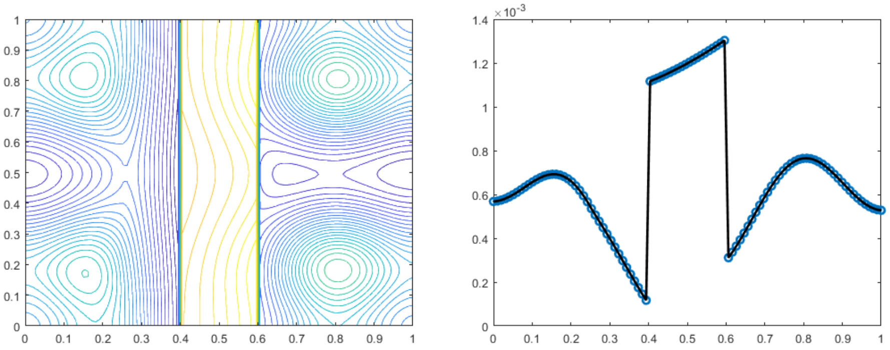

(e) Contour at $t = 1.0$ (f) Plot at $t = 1.0$

Figure 3.13: Heat distribution of Case 4: Two solution jump conditions are $[u]_{x=\frac{2}{5}} = \frac{(1+0.01t)}{10^3}$ and $[u]_{x=\frac{3}{5}} = -\frac{(1+0.01t)}{10^3}$; two flux jump conditions are $[\beta u_x]_{x=\frac{2}{5}} = \frac{t}{10^4}$ and $[\beta u_x]_{x=\frac{3}{5}} = -\frac{t}{10^4}$.

propagation problem as shown in these figures.

3.5 Conclusion

This work has developed a novel mass-preserving solution-flux finite difference scheme for solving time-dependent multi-layer problems with external BCs and internal BCs at the interfaces between adjacent layers. We apply the staggered mesh discritization to solve the multi-layers interface parabolic equations. The solution and flux scheme was established at regular grid points in each layer or subdomain. But at irregular points next to interfaces, we developed corrected approximation fluxes from two sides of the interface by combining with the interface conditions at interfaces. We proved the our schemes to satisfy conservation of mass in the discrete form for 1D and 2D parabolic interface equations with multi-layers. Numerical solutions in 1D and 2D problems showed mass conservation and convergence orders in time and space step sizes. Moreover, the numerical simulation for real applications of the diffusion process with large difference piecewise diffusion and heat propagation in the multi-layer media showed the excellent performance. As far as our understanding, this is the first work towards the solution of multi-layer which maintain to preserve the mass. Thus, the major contribution of this work is preserving mass while keeping accuracy in layered problems which will be very useful in many applications like heat conduction in composite materials, transport of contamination, chemicals and gases in layered porous media, brain tumor growth, heat conduction through skin. Although, this scheme is designed for 1D and 2D problems, extension to 3D problems can be done. Moreover, it opens for study in curve interface problems in this regards in the late future.

Chapter 4

Efficient Conservative Pressure-Velocity Scheme for the Coupled Free and Porous Media Flow Systems

4.1 Introduction

Fluid flows and species and energy transports in coupled free flow and porous medium systems appear in a wide spectrum of environmental settings, industrial and biological applications. The free flow system is termed so, because it contains only fluids, while the porous medium system contains one or more fluids and a solid, and the fluids flow through the porous medium. Among environmental applications, we can mention river, lake or wetland interactions with the vadose zone, evaporation of water from the soil system influenced by wind and transport of water vapor to the atmosphere, precipitation of salts in drying porous media, and surface water/groundwater contamination. Design of filters, insulators and oxygen sensors, industrial wood drying, modeling of flows in blood vessels and natural tissues, and transport of drugs and nutrients are only a few examples of industrial and biological applications. Several numerical methods have been studied for solving the problems such as finite volume method [78], finite element method and finite difference method [50, 55]. However, there are significantly less efforts to develop conservative numerical methods for the free and porous media flow systems. The mass conservation is an important physical law in coupling surface and porous media flows. To preserve the mass over the whole domain is important for developing numerical methods to solve the time-dependent coupled system of free and porous media flows, especially for long term simulations.

In this part of thesis, we develop an efficient conservative pressure-velocity scheme for the coupled Stokes-Darcy flows with interface conditions in sharp interface. The whole coupled Stokes-Darcy domain is partitioned into staggered meshes where free flow velocities, Darcy velocities and pressures in both regions are defined over staggered grid framework [83]. Based on the projection techniques in free flow, and proposing the efficient treating of interface conditions, we construct a time-splitting discretization scheme for the system. Further, applying the staggered finite difference operators, we develop a conservative pressure-velocity scheme for the coupled free and porous media flow system. The important features of the developed scheme are that it is mass conservative and it is decoupled in computation. We theoretically prove that the scheme satisfies mass conservation over the whole domain of free and porous media flows. Two model problems for numerical experiments are first given to show mass conservation and the convergence of proposed algorithm in time and space sizes. Then, we solve by using our scheme two famous problems in fluid flow lid driven cavity and inflow-outflow to show mass conservation and the reliability of computation. At last, we compute a realistic problem in inflow-outflow setting where porous media has two layers to verify the effectiveness of scheme. Numerical results show numerically our proposed scheme performs excellently.

The rest of this part is organized as follows. In Section 4.2, we describe the flow systems of interest which include the surface flow and porous media flow; and interface conditions at the fluid-porous media interface as well as the boundary conditions. Section 4.3 is devoted to propose conservative pressure-velocity scheme for the coupled systems and prove the scheme to satisfy mass conservation. In Section 4.4, numerical experiments are presented to analyze convergence of the scheme and show the performance of the scheme for some popular real model problems existed in this coupled systems. The conclusions are given in Section 4.5.

4.2 Governing equations with interface and boundary conditions

Depending on the application, the porous medium system can contain single or multiple fluid phases, and the phases in both flow domains can be composed of single or multiple chemical species (components). we consider a single fluid in the free flow domain (gas or water) which can be composed of several chemical species. For the porous medium, we consider the pore space is fully saturated/unsaturated with the same fluid as in the free flow domain.

4.2.1 Governing equations

We consider the same fluid in a model of problem consisting of an incompressible flow in the free flow region Ω_f with the boundary $\partial\Omega_f$ that the momentum balance is described by the Stokes equations and a Darcy flow in the porous medium Ω_p with the boundary $\partial\Omega_p$. The bounded regions Ω_f and $\Omega_p \subset \Re^2$ are interconnected and separated by an interface Γ (see Fig. 4.1).

In the fluid region Ω_f, two dimensional incompressible Stokes equations in free flow are given by

$$\frac{\partial \mathbf{u}}{\partial t} = -\nabla p + \nu \nabla^2 \mathbf{u} + \mathbf{F}, \qquad (x, y, t) \in \Omega_f \times (0, T] \tag{4.1}$$

$$\nabla.\mathbf{u} = 0, \qquad (x, y, t) \in (\Omega_f \times (0, T] \tag{4.2}$$

Where p is the pressure, $\mathbf{u} = (u, v)$ the velocity of flow, $\mathbf{F} = (f_u, f_v)$ the external force, and ν kinematic viscosity.

The porous medium region Ω_p, where the fluid and solid occupy with whole region on the macroscopic scale is a homogeneous continuum domain. If the porous media is weakly compressible [58, 77], then we can have

$$c_p \frac{\partial p_p}{\partial t} + \nabla.(\mathbf{u}_p) = f_p, \qquad (x, y, t) \in \Omega_p \times (0, T] \tag{4.3}$$

and the Darcy's law with no gravitational acceleration is given by

$$\mathbf{u}_p = -\frac{\kappa}{\mu} \nabla p_p, \qquad (x, y, t) \in \Omega_p \times (0, T] \tag{4.4}$$

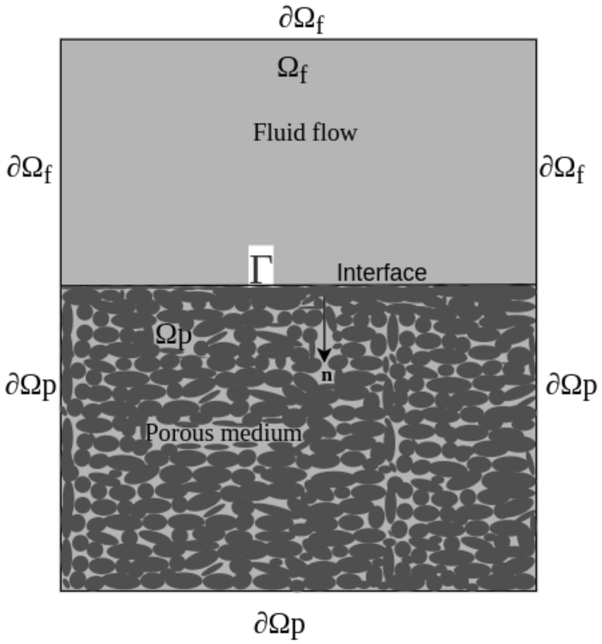

Figure 4.1: Schematic model of coupled Stokes-Darcy system.

Where p_p is the pressure, $\mathbf{u}_p = (u_p, v_p)$ is the velocity of flow in porous medium, f_p is source (sink) term, $c_p = \frac{\partial(\phi\rho)}{\partial p_p}$ is the compressibility parameter, κ is the permeability and μ is dynamic viscosity.

4.2.2 Interface conditions of flow at fluid and porous medium

Across the interface Γ, the governing equations have to couple appropriate conditions [51]. First, the conservation of mass aross the interface requires the mass flux leaving the free flow region to be equal to mass flux entering the porous medium which can be written as

$$[\mathbf{u}.n] = -[\mathbf{u}_p.n_p],$$

where n is the unit normal vector outward from free flow region at the interface and $n_p = -n$. After simplified for the problem in Fig. 4.1, we get

$$v = v_p, \qquad (x, y, t) \in \Gamma \times (0, T] \tag{4.5}$$

Second, the normal stress for Newtonian fluids at the interface from the free flow side is given by

$$[n.T(\mathbf{u}, p).n] = [n.(2\nu D(\mathbf{u}) - pI).n],$$

where $D(\mathbf{u}) = \frac{1}{2}(\nabla\mathbf{u} + (\nabla\mathbf{u})^T)$ is the deformation tensor. In the porous medium, slow flow is assumed and Darcys law is used, thus viscous stress is not treated explicitly, it is already accounted for in the permeability [78]. Therefore, pressure is the only force acting on the interface that has to be taken into account from the porous medium domain $[n.T(\mathbf{u}, p).n] = -p_p$. Therefore, the balance of normal forces across the interface can be formulated as

$$p - 2\nu\frac{\partial v}{\partial y} = p_p, \qquad (x, y, t) \in \Gamma \times (0, T] \tag{4.6}$$

Lastly, since the fluid model is viscous, a condition on the tangential fluid velocity on interface Γ must be given. In general, the simplest assumption of no slippage along the interface Γ is invalid due to large deviation from experimental measurements [51]. Therefore Beavers-Josep-Saffman (BTS) interface condition [8, 80] is applied which is stated as

$$\left[\mathbf{u}.\tau + \frac{2\sqrt{\kappa}}{\alpha} n.D(\mathbf{u}).\tau\right] = 0,$$

where τ is the unit tangent vector along the interface Γ and α is the positive Bevers-Joseph parameter. After simplified we get for the problem in Fig.1.

$$u + \frac{\sqrt{\kappa}}{\alpha}\left(\frac{\partial v}{\partial x} + \frac{\partial u}{\partial y}\right) = 0, \qquad (x, y, t) \in \Gamma \times (0, T] \tag{4.7}$$

Further, in this whole continuum 2D domain, the interface line Γ divides free flow region Ω_f and porous medium region Ω_p.

4.2.3 Boundary conditions

Since velocity and pressure in the free flow are primitive variables but in porous media , the only pressure would be a primary variable. In this work, Dirichlet boundary conditions for the velocity field in free flow will be considered. Also our model of equations will be based on two dimensions only. In the solid surfaces, most solid surfaces are impermeable to fluid and the fluid sticks to their surface. Hence, there is no slip and no penetration, and the fluid particles on the wall move with the velocity of the wall:

$$\mathbf{u} = \mathbf{G} \qquad (x, y, t) \in \partial\Omega_f \times (0, T] \tag{4.8}$$

where $\mathbf{G} = (g_u, g_v)$ is known velocity of the impermeable wall. In fact, where the walls are stationary we have

$$\mathbf{u} = \mathbf{0} \qquad (x, y, t) \in \partial\Omega_f \times (0, T] \tag{4.9}$$

On the other case, many applications we are only interested in the behavior in a small region.For instances, if we want to study the ventilation in a room; it would be only model the room and treat its interaction with the rest of the world via treat its inflow boundary conditions e.g. by prescribing the wind velocity through an open window. Hence at inflow (or outflow) boundaries we prescribe the velocity, i.e.

$$\mathbf{u.n} = \mathbf{W} \qquad (x, y, t) \in \partial\Omega_f \times (0, T] \tag{4.10}$$

where $\mathbf{W} = (w_u, w_v)$ is a prescribe function.

In porous media, we assume Neumann boundary conditions i.e.

$$\frac{\partial p_p}{\partial n_p} = g_p \qquad (x, y, t) \in \partial\Omega_p \times (0, T] \tag{4.11}$$

where n_p is the unit normal vector outward from porous medium region at the boundary.

4.3 Conservative Pressure-Velocity Scheme for Coupled Free and Porous Media Flow Systems

4.3.1 Staggered grid and time discretization

The whole domain Ω is the union of free flow domain Ω_f and porous medium domain Ω_p together with fluid-porous interface Γ i.e. $\Omega = \Omega_f \bigcup \Gamma \bigcup \Omega_p$. Ω is divided into the staggered mesh (see Fig. 4.2). For simplicity of description, let the middle points of cell faces be $(x_{i+\frac{1}{2}}, y_j)$ and $(x_i, y_{j+\frac{1}{2}})$; and let cell center points be (x_i, y_j). Let $\Delta x = \frac{b-a}{I}, \Delta y = \frac{c-d}{J}$ are the positive integers. Define

$\mathrm{x}_{i+\frac{1}{2}} = a + i\Delta x, i = 0, 1, 2, ..., I, x_i = a + (i - \frac{1}{2})\Delta x, i = 1, 2, ..., I$, and

$\mathrm{y}_{j+\frac{1}{2}} = c + j\Delta y, j = 0, 1, 2, ..., J, y_j = c + (j - \frac{1}{2})\Delta y, j = 1, 2, ..., J,$

Nodes $(x_{i+\frac{1}{2}}, y_j)$ and $(x_i, y_{j+\frac{1}{2}})$ are the nodes for horizontal velocity (u, u_p) and vertical velocity (v, v_p) respectively ; and (x_i, y_j) are the nodes for pressure (p, p_p). (U, U_p), (V, V_p) be numerical solutions of (u, u_p) and (v, v_p) respectively. And (P, P_p) is the numerical solution of (p, p_p) (see in Fig. 4.2).

Let $\Delta t = \frac{T}{N}$ and $t^n = n\Delta t, n = 0, 1, ..., N$. Let $w_{i,j}, w_{i+\frac{1}{2},j}, w_{i,+\frac{1}{2}j}$ be the values of $w(x, y)$ defined at the nodes $(x_i, y_j), (x_{i+\frac{1}{2}}, y_j)$ and $(x_i, y_{j+\frac{1}{2}})$. Define space center difference operators as

$$\delta_x w_{i+\frac{1}{2},j} = \frac{w_{i+1,j} - w_{i,j}}{\Delta x}, \delta_y w_{i,j+\frac{1}{2}} = \frac{w_{i,j+1} - w_{i,j}}{\Delta y}$$

$$\delta_x w_{i,j} = \frac{w_{i+\frac{1}{2},j} - w_{i-\frac{1}{2},j}}{\Delta x}, \delta_y w_{i,j} = \frac{w_{i,j+\frac{1}{2}} - w_{i,j-\frac{1}{2}}}{\Delta y}$$

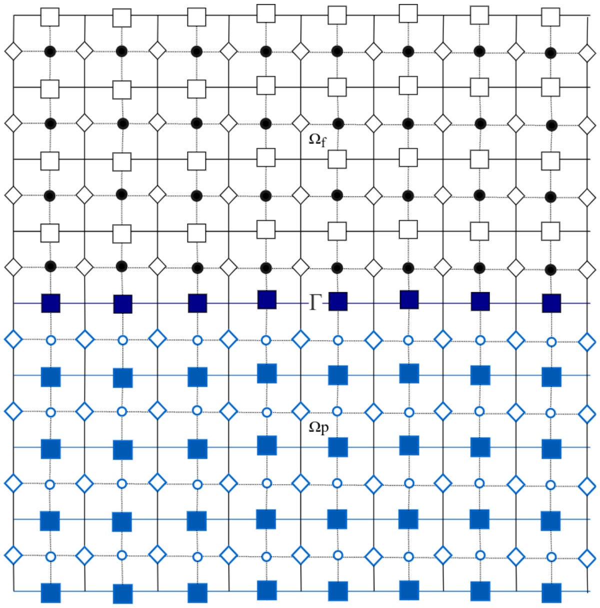

Figure 4.2: Staggered grid for finite difference scheme; ◇ : U velocity in free flow, □ : V velocity in free flow, ◇ : U_p velocity in porous medium, ■ : V_p velocity in porous medium, ● : P pressure in free flow ○ : P_p pressure in porous medium.

4.3.2 Time-splitting discretization scheme

We will develop the time-splitting discretization scheme. We first calculate the vertical velocity of coupled system at the middle cell edges along horizontal line together with fluid-porous interface Γ. For doing this, from the limiting approach in (4.1), the y momentum equation of free flow can have at interface Γ

$$\frac{\partial v}{\partial t}_{\Gamma} = -\frac{\partial p}{\partial y}_{\Gamma} + \nu \left(\frac{\partial^2 v}{\partial x^2}_{\Gamma} + \frac{\partial^2 v}{\partial y^2}_{\Gamma} \right) + f_{v_{\Gamma}} \tag{4.12}$$

which will be used in the time-splitting discritization scheme. The time-splitting projection method for a temporal discretization is developed to calculate numerically the primitive variables (U, V) and (P, P_p) at the time level $n+1$ on the staggered grid. The projection method begins from a temporal discretization of the Stokes-Darcy equations which decouples the computation of velocity and pressure in Stokes equations.

$$\frac{\mathbf{U}^* - \mathbf{U}^n}{\Delta t} = \nu \nabla^2 \mathbf{U}^* + \mathbf{F}^{n+1}, \tag{4.13}$$

$$\frac{\mathbf{U}^{n+1} - \mathbf{U}^*}{\Delta t} = -\nabla P^{n+1}. \tag{4.14}$$

In free flow, we can see a key feature of the projection method by a time splitting discretization that the system decouples the computation of velocity and pressure. In the first step, an intermediate velocity field is computed using the momentum equation and ignoring the incompressible constraint. In the second step, the intermediate velocity is projected to the space of divergence free vector fields to get the next update of velocity and pressure. This procedure ensures that it is locally conservative approach [92].

Firstly, at Step I, we propose a predictor intermediate vertical velocity V^* at the interface Γ. Then, predictor intermediate vertical velocity V^* and intermediate horizontal velocity U^* are calculated. At Step II, the pressure Poisson equation of free flow can be calculated by taking the divergence of (4.14) and using the fact that $\nabla . \mathbf{U}^{n+1} = 0$. Then, the calculated pressure value can be substituted in (4.14) to get interior corrector value of velocity $\mathbf{U}^{n+1}$. Pressure and velocity in porous media by coupling the interface vertical velocity value are calculated after solved free flow system. Finally, corrected vertical velocity V^{n+1} at interface Γ is calculated. The time-splitting scheme to the system is given as in $[t^n, t^{n+1}]$.

Step I:

$$\frac{\mathbf{U}^* - \mathbf{U}^n}{\Delta t} = \nu \nabla^2 \mathbf{U}^* + \mathbf{F}^{n+1}, \qquad (x,y) \in \Omega_f \tag{4.15}$$

$$\mathbf{U}^* = \mathbf{G}^{n+1} \quad \vee \quad \mathbf{W}^{n+1}, \qquad (x,y) \in \partial\Omega_f \tag{4.16}$$

$$U^* + \frac{\sqrt{\kappa}}{\alpha}\left(\frac{\partial V^*}{\partial x} + \frac{\partial U^*}{\partial y}\right) = 0, \qquad (x,y) \in \Gamma \tag{4.17}$$

$$\frac{V^* - V^n}{\Delta t} = \nu \frac{\partial^2 V^*}{\partial x^2}_{\Gamma} + \nu \frac{\partial^2 V^*}{\partial y^2}_{\Gamma} + f_{v_\Gamma}^{n+1}, \qquad (x,y) \in \Gamma \tag{4.18}$$

Step II:

$$\frac{\mathbf{U}^{n+1} - \mathbf{U}^*}{\Delta t} = -\nabla P^{n+1}, \qquad (x,y) \in \Omega_f \tag{4.19}$$

$$\nabla . \mathbf{U}^{n+1} = 0, \qquad (x,y) \in \Omega_f \tag{4.20}$$

$$\mathbf{U}^{n+1} = \mathbf{G}^{n+1} \quad \vee \quad \mathbf{W}^{n+1}, \qquad (x,y) \in \partial\Omega_f \tag{4.21}$$

$$c_p \frac{\partial P_p^{n+1}}{\partial t} + \nabla . (\mathbf{U}_p^{n+1}) = \mathbf{f}_p^{n+1}, \qquad (x,y) \in \Omega_p \tag{4.22}$$

$$\mathbf{U}_p^{n+1} = -\frac{\kappa}{\mu} \nabla P_p^{n+1}, \qquad (x,y) \in \Omega_p \tag{4.23}$$

$$\frac{V^{n+1} - V^*}{\Delta t} = \nu \frac{\partial^2 V^{n+1}}{\partial x^2}_{\Gamma} + \nu \frac{\partial^2 V^{n+1}}{\partial y^2}_{\Gamma} + f_{v_\Gamma}^{n+1}, \quad , \quad (x,y) \in \Gamma \tag{4.24}$$

$$V^{n+1} = V_p^{n+1}, \quad (x,y) \in \Gamma \tag{4.25}$$

$$P^{n+1} - 2\nu \frac{\partial V^{n+1}}{\partial y} = P_p^{n+1}, \quad (x,y) \in \Gamma \tag{4.26}$$

$$\frac{\partial P_p^{n+1}}{\partial n_p} = g_p^{n+1} \qquad (x,y) \in \partial\Omega_p \tag{4.27}$$

In Step II, for solving the pressure of free flow, taking the divergence in equation (4.19) and substituting from equation (4.20) lead to

$$\frac{\partial^2 P^{n+1}}{\partial x^2} + \frac{\partial^2 P^{n+1}}{\partial y^2} = \frac{1}{\Delta t}\left(\frac{\partial U^*}{\partial x} + \frac{\partial V^*}{\partial y}\right), \qquad (x,y) \in \Omega_f \tag{4.28}$$

In the staggered grid, the pressure are calculated in cell center (see figure 4.2). In the projection method, the pressure in equation (4.28) is provided Neumann boundary conditions to avoid ghost cell, interpolation or extrapolation in over all external boundaries [74]. According to [71, 74], the pressure P has a solution upto an arbitrary constant when the equation (4.28) satisfies compatibility condition. Thus, the equation (4.19) and the compatibility condition in equation (4.28) provides Neumann condition for P on $\partial\Omega_f$ to be zero, i.e.

$$\frac{\partial P^{n+1}}{\partial n} = 0 \qquad (x,y,t) \in \partial\Omega_f \times (0,T], \tag{4.29}$$

and zero for Neumann boundary condition on the interface Γ [50].

4.3.3 The conservative pressure-velocity scheme for the system

We further propose the space discritization to the system over staggered mesh. Let $U_{i+\frac{1}{2},j}, V_{i,j+\frac{1}{2}}$ and $P_{i,j}$ be denoted the discrete approximations of the flow velocity $u(x_{i+\frac{1}{2}}, y_j)$, $v(x_i, y_{j+\frac{1}{2}})$ and $p(x_i, y_j)$ respectively. let $U_{pi+\frac{1}{2},j}, V_{pi,j+\frac{1}{2}}$ and $P_{pi,j}$ be denoted the discrete approximations of the flow velocity $u_p(x_{i+\frac{1}{2}}, y_j), v_p(x_i, y_{j+\frac{1}{2}})$ and $p_p(x_i, y_j)$ respectively. We consider interface Γ at the grid line $y = y_{j_0+\frac{1}{2}}$. Therefore, the conservative pressure-velocity scheme for the system of free and porous media flow is proposed as

Stage I:

(a) The predictor intermediate values for V^* on the interface Γ from the equation (4.12), are computed by semi-implicit scheme,

$$\begin{aligned}\frac{{V^*}_{i,j_0+\frac{1}{2}} - V^n_{i,j_0+\frac{1}{2}}}{\Delta t} &= \frac{\nu}{\Delta x^2}\left(V^n_{i-1,j_0+\frac{1}{2}} - 2{V^*}_{i,j_0+\frac{1}{2}} + V^n_{i+1,j_0+\frac{1}{2}}\right) \\ &\quad + \frac{\nu}{\Delta y^2}\left(\widehat{V}^n_{i,j_0-\frac{1}{2}} - 2{V^*}_{i,j_0+\frac{1}{2}} + V^n_{i,j_0+\frac{3}{2}}\right) + {f_v}^{n+1}_{i,j_0+\frac{1}{2}}, \qquad 1 \le i \le I\end{aligned} \tag{4.30}$$

From (4.6), we have

$$P^n_{i,j_0+\frac{1}{2}} - 2\nu\frac{\left(V^n_{i,j_0+\frac{3}{2}} - \widehat{V}^n_{i,j_0-\frac{1}{2}}\right)}{2\Delta y} = P^n_{p_{i,j_0+\frac{1}{2}}} \tag{4.31}$$

where $\widehat{V}^n_{i,j_0-\frac{1}{2}}$ is the fictitious value at $(x_i, y_{j_0-\frac{1}{2}}$(i.e. it lies outside of domain Ω_f). We substitute the value of $\widehat{V}^n_{i,j_0-\frac{1}{2}}$ from the equation (4.31) into (4.30) where $P^n_{i,j_0+\frac{1}{2}}$ is replaced by P^n_{i,j_0+1}; and $P^n_{p_{i,j_0+\frac{1}{2}}}$ by $P^n_{p_{i,j_0}}$.

(b) The intermediate variables $\{V^*_{i,j+\frac{1}{2}}\}$ and $\{U^*_{i+\frac{1}{2},j}\}$ in the interior of domain Ω_f are computed by the implicit scheme,

$$\frac{V^*_{i,j+\frac{1}{2}} - V^n_{i,j+\frac{1}{2}}}{\Delta t} = \nu\delta_x^2 V^*_{i,j+\frac{1}{2}} + \nu\delta_y^2 V^*_{i,j+\frac{1}{2}} + f^{\,n+1}_{v_{i,j+\frac{1}{2}}}, \qquad 1 \le i \le I, \quad j_0 + \frac{3}{2} \le j \le J-1 \tag{4.32}$$

$$V^*_{a,j+\frac{1}{2}} = g^{n+1}_{v_{a,j+\frac{1}{2}}}, \quad V^*_{b,j+\frac{1}{2}} = g^{n+1}_{v_{b,j+\frac{1}{2}}}, \quad V^*_{i,d} = g^{n+1}_{v_{i,d}} \qquad 1 \le i \le I, \tag{4.33}$$

In a approximation of $\delta_x^2 V^*_{1,j+\frac{1}{2}}$, the value of $V^*_{-1,j+\frac{1}{2}}$ is obtained by averaging i.e. $V^*_{-1,j+\frac{1}{2}} = 2g^{n+1}_{v_{a,j+\frac{1}{2}}} - V^*_{1,j+\frac{1}{2}}$; and similar for $V^*_{I+1,j+\frac{1}{2}} = 2g^{n+1}_{v_{b,j+\frac{1}{2}}} - V^*_{I,j+\frac{1}{2}}$ in $\delta_x^2 V^*_{I,j+\frac{1}{2}}$.

$$\frac{U^*_{i+\frac{1}{2},j} - U^n_{i+\frac{1}{2},j}}{\Delta t} = \nu\delta_x^2 U^*_{i+\frac{1}{2},j} + \nu\delta_y^2 U^*_{i+\frac{1}{2},j} + f^{\,n+1}_{u_{i+\frac{1}{2},j}}, \quad 1 \le i + \frac{1}{2} \le I-1, j_0+2 \le j \le J \tag{4.34}$$

In the discretization of $\delta_y^2 U^*_{i+\frac{1}{2},j_0+1} = \frac{\delta_y U^*_{i+\frac{1}{2},j_0+\frac{3}{2}} - \delta_y U^*_{i+\frac{1}{2},j_0+\frac{1}{2}}}{\Delta y}$, the value of $\delta_y U^*_{i+\frac{1}{2},j_0+\frac{1}{2}}$ can be obtained from the interface condition.

$$U^*_{i+\frac{1}{2},j_0+\frac{1}{2}} + \frac{\sqrt{\kappa}}{\alpha}\left(\delta_x V^*_{i+\frac{1}{2},j_0+\frac{1}{2}} + \delta_y U^*_{i+\frac{1}{2},j_0+\frac{1}{2}}\right) = 0, \tag{4.35}$$

And from the Taylor expansion, we get $U^*_{i+\frac{1}{2},j_0+\frac{1}{2}} = \frac{3U^*_{i+\frac{1}{2},j_0+1} - U^*_{i+\frac{1}{2},j_0+2}}{2}$, Thus, at $j =$

$j_0 + 1$ and $1 \leq i + \frac{1}{2} \leq I - 1$ we have

$$\frac{U^*_{i+\frac{1}{2},j_0+1} - U^n_{i+\frac{1}{2},j_0+1}}{\Delta t} = \nu \delta_x^2 U^*_{i+\frac{1}{2},j} + \frac{\nu}{\Delta y}\left(\delta_y U^*_{i+\frac{1}{2},j_0+\frac{3}{2}} + \frac{\alpha}{\sqrt{\kappa}}\left(\frac{3U^*_{i+\frac{1}{2},j_0+1} - U^*_{i+\frac{1}{2},j_0+2}}{2}\right) + \delta_x \widetilde{V}_{i+\frac{1}{2},j_0+\frac{1}{2}}\right) + f_{u_{i+\frac{1}{2},j_0+1}}^{n+1} \tag{4.36}$$

$$U^*_{a,j} = g^{n+1}_{u_{a,j}}, \quad U^*_{b,j} = g^{n+1}_{u_{b,j}}, \quad U^*_{i,d} = g^{n+1}_{u_{i,d}} \qquad 1 \leq i + \frac{1}{2} \leq I, \quad j_0 + 2 \leq j \leq J \tag{4.37}$$

In the approximation of $\delta_y^2 U^*_{i+\frac{1}{2},J}$, as above the value of $U^*_{i+\frac{1}{2},J+1}$ is obtained by averaging i.e. $U^*_{i+\frac{1}{2},J+1} = 2g^{n+1}_{u_{i+\frac{1}{2},d}} - U^*_{j+\frac{1}{2},J}$.

Stage II:

(a) The pressure $\{P^{n+1}_{i,j}\}$ can be solved by

$$\delta_x^2 P^{n+1}_{i,j} + \delta_y^2 P^{n+1}_{i,j} = \frac{1}{\Delta t}\left(\delta_x U^*_{i,j} + \delta_y V^*_{i,j}\right), \qquad 1 \leq i \leq I, \quad j_0 + 1 \leq j \leq J \tag{4.38}$$

$$\delta_x P^{n+1}_{a,j} = \delta_x P^{n+1}_{b,j} = \delta_y P^{n+1}_{i,j_0+\frac{1}{2}} = \delta_y P^{n+1}_{i,d} = 0, \qquad 1 \leq i \leq I, \quad j_0 + 1 \leq j \leq J \tag{4.39}$$

(b) Then, the $\{U^{n+1}_{i+\frac{1}{2},j}, V^{n+1}_{i,j+\frac{1}{2}}\}$ is solved by

$$\frac{V^{n+1}_{i,j+\frac{1}{2}} - V^*_{i,j+\frac{1}{2}}}{\Delta t} = -\delta_y P^{n+1}_{i,j+\frac{1}{2}}, \qquad 1 \leq i \leq I, \quad j_0 + \frac{3}{2} \leq j \leq J - 1 \tag{4.40}$$

$$\frac{U^{n+1}_{i+\frac{1}{2},j} - U^*_{i+\frac{1}{2},j}}{\Delta t} = -\delta_x P^{n+1}_{i+\frac{1}{2},j}, \qquad 1 \leq i + \frac{1}{2} \leq I - 1, \quad j_0 + 1 \leq j \leq J \tag{4.41}$$

$$U^{n+1}_{a,j} = g^{n+1}_{u_{a,j}}, \quad U^{n+1}_{b,j} = g^{n+1}_{u_{b,j}}, \qquad j_0 + 2 \leq j \leq J \tag{4.42}$$

(c) The correction values of $\{V^{n+1}_{i,j_0+\frac{1}{2}}\}$ at the interface Γ are approximated as

$$\begin{aligned}\frac{V^{n+1}_{i,j_0+\frac{1}{2}} - V^{*}_{i,j_0+\frac{1}{2}}}{\Delta t} &= \frac{\nu}{\Delta x^2}\left(V^{n+1}_{i-1,j_0+\frac{1}{2}} - 2V^{n+1}_{i,j_0+\frac{1}{2}} + V^{n+1}_{i+1,j_0+\frac{1}{2}}\right) \\ &+ \frac{\nu}{\Delta y^2}\left(\widehat{V}^{n+1}_{i,j_0-\frac{1}{2}} - 2V^{n+1}_{i,j_0+\frac{1}{2}} + V^{n+1}_{i,j_0+\frac{3}{2}}\right) + {f_v}^{n+1}_{i,j_0+\frac{1}{2}}, \qquad 1 \le i \le I\end{aligned} \tag{4.43}$$

where, the values of $\widehat{V}^{n+1}_{i,j_0-\frac{1}{2}}$ is substituted from the interface condition (4.6).

$$P^{n+1}_{i,j_0+\frac{1}{2}} - 2\nu\frac{\left(V^{n+1}_{i,j_0+\frac{3}{2}} - \widehat{V}^{n+1}_{i,j_0-\frac{1}{2}}\right)}{2\Delta y} = P^{n}_{p_{i,j_0+\frac{1}{2}}} \tag{4.44}$$

$$V^{n+1}_{i,d} = g^{n+1}_{v_{i,d}}, \qquad 1 \le i \le I, \tag{4.45}$$

(d) The $\{P^{n+1}_{p_{i,j}}, U^{n+1}_{p_{i+\frac{1}{2},j}}, V^{n+1}_{p_{i,j+\frac{1}{2}}}\}$ will be solved by

$$c_p\frac{P^{n+1}_{p_{i,j}} - P^{n}_{p_{i,j}}}{\Delta t} + \delta_x U^{n+1}_{p_{i,j}} + \delta_y V^{n+1}_{p_{i,j}} = \mathbf{f}^{n+1}_{p_{i,j}} \qquad 1 \le i \le I, \quad 1 \le j \le j_0 \tag{4.46}$$

$$U^{n+1}_{p_{i+\frac{1}{2},j}} = -\frac{\kappa}{\mu}\delta_x P^{n+1}_{p_{i+\frac{1}{2},j}}, \qquad 0 \le i + \frac{1}{2} \le I, \quad 1 \le j \le j_0 \tag{4.47}$$

$$V^{n+1}_{p_{i,j+\frac{1}{2}}} = -\frac{\kappa}{\mu}\delta_y P^{n+1}_{p_{i,j+\frac{1}{2}}}, \qquad 1 \le i \le I, \quad 0 \le j \le j_0 - \frac{1}{2} \tag{4.48}$$

with the interface condition (4.5)

$$V^{n+1}_{p_{i,j_0+\frac{1}{2}}} = V^{n+1}_{i,j_0+\frac{1}{2}} \qquad 1 \le i \le I \tag{4.49}$$

and boundary conditions

$$\frac{\partial P_{p_{a,j}}^{n+1}}{\partial x} = g_{p_{a,j}}^{n+1}, \quad \frac{\partial P_{p_{b,j}}^{n+1}}{\partial x} = g_{p_{b,j}}^{n+1}, \quad 1 \le j \le j_0 \tag{4.50}$$

$$\frac{\partial P_{p_{i,c}}^{n+1}}{\partial y} = g_{p_{i,c}}^{n+1}, \qquad 1 \le i \le I. \tag{4.51}$$

For the whole system of scheme, the initial values are provided by

$$V_{i,j+\frac{1}{2}}^{0} = V_{0_{i,j+\frac{1}{2}}}, \quad U_{i+\frac{1}{2},j}^{0} = U_{0_{i+\frac{1}{2},j}}, \quad P_{p_{i,j}}^{0} = P_{p0_{i,j}} \tag{4.52}$$

4.3.4 Mass Conservation

For the scheme (4.32) - (4.52), we have the following mass conservation to the coupled Stokes-Darcy system in discrete form.

Theorem 5. *The scheme (4.32)- (4.52) satisfies the mass conservation, i.e.*

$$\delta_x U_{i,j}^{n+1} + \delta_y V_{i,j}^{n+1} = 0, \quad \forall i,j, \quad 1 \le i \le I, \quad j_0 + 1 \le j \le J \tag{4.53}$$

and

$$\begin{aligned} c_p \sum_{i=1}^{I}\sum_{j=1}^{j_0} P_{p_{i,j}}^{n+1} \Delta x \Delta y = c_p \sum_{i=1}^{I}\sum_{j=1}^{j_0} P_{p_{i,j}}^{0} \Delta x \Delta y + \sum_{n=0}^{N-1} \Bigg(\frac{\kappa}{\mu} \sum_{j=1}^{j_0} \left(g_{p_{b,j}}^{n+1} - g_{p_{a,j}}^{n+1} \right) \Delta y \\ - \sum_{i=1}^{I} \left(V_{i,j_0+\frac{1}{2}}^{n+1} + \frac{\kappa}{\mu} g_{p_{i,c}}^{n+1} \right) \Delta x + \sum_{i=1}^{I}\sum_{j=1}^{j_0} f_{p_{i,j}}^{n+1} \Delta x \Delta y \Bigg) \Delta t \end{aligned} \tag{4.54}$$

Where the nodes $(x_i, y_{j_0+\frac{1}{2}})$ *are on the interface* Γ

Proof. From (4.40) and (4.41), we can have

$$\frac{V^{n+1}_{i,j+\frac{1}{2}} - V^{n+1}_{i,j-\frac{1}{2}}}{\Delta y} = \frac{V^{*}_{i,j+\frac{1}{2}} - V^{*}_{i,j-\frac{1}{2}}}{\Delta y} - \Delta t \left(\frac{\delta_y P^{n+1}_{i,j+\frac{1}{2}} - \delta_y P^{n+1}_{i,j-\frac{1}{2}}}{\Delta y} \right), \tag{4.55}$$

$$\frac{U^{n+1}_{i+\frac{1}{2},j} - U^{n+1}_{i-\frac{1}{2},j}}{\Delta x} = \frac{U^{*}_{i+\frac{1}{2},j} - U^{*}_{i-\frac{1}{2},j}}{\Delta x} - \Delta t \left(\frac{\delta_x P^{n+1}_{j+\frac{1}{2},j} - \delta_x P^{n+1}_{i-\frac{1}{2},j}}{\Delta x} \right). \tag{4.56}$$

Adding (4.55) and (4.56), we obtain that

$$\delta_x U^{n+1}_{i,j} + \delta_y V^{n+1}_{i,j} = \left[\left(\delta_x U^{*}_{i,j} + \delta_y V^{*}_{i,j} \right) - \Delta t \left(\delta_x^2 P^{n+1}_{i,j} + \delta_y^2 P^{n+1}_{i,j} \right) \right] \tag{4.57}$$

Thus, from (4.38), it follows that

$$\delta_x U^{n+1}_{i,j} + \delta_y V^{n+1}_{i,j} = 0, \qquad \forall (i,j) \tag{4.58}$$

Summing i from 1 to I, j_0, j from 1 to j_0 in the equation (4.46) and multiplying by $\Delta x \Delta y$, we can have

$$c_p \sum_{i=1}^{I} \sum_{j=1}^{j_0} \frac{P^{n+1}_{p_{i,j}} - P^{n}_{p_{i,j}}}{\Delta t} = -\sum_{i=1}^{I} \sum_{j=1}^{j_0} \left(\delta_x U^{n+1}_{p_{i,j}} + \delta_y V^{n+1}_{p_{i,j}} - f^{n+1}_{p_{i,j}} \right) \Delta x \Delta y \tag{4.59}$$

and from (4.47) (4.48), using (4.59), we get

$$c_p \sum_{i=1}^{I} \sum_{j=1}^{j_0} \frac{P^{n+1}_{p_{i,j}} - P^{n}_{p_{i,j}}}{\Delta t} = \sum_{i=1}^{I} \sum_{j=1}^{j_0} \left(\frac{\kappa}{\mu} \delta_x^2 P^{n+1}_{p_{i,j}} + \frac{\kappa}{\mu} \delta_y^2 P^{n+1}_{p_{i,j}} + f^{n+1}_{p_{i,j}} \right) \Delta x \Delta y \tag{4.60}$$

Applying the flux difference in the second order derivatives of pressure P_p and using the boundary conditions $\frac{\partial P_{p_{\frac{1}{2},j}}^{n+1}}{\partial x} = g_{p_{a,j}}^{n+1}$, $\frac{\partial P_{p_{I+\frac{1}{2},j}}^{n+1}}{\partial x} = g_{p_{b,j}}^{n+1}$, $\frac{\partial P_{p_{i,\frac{1}{2}}}^{n+1}}{\partial y} = g_{p_{i,c}}^{n+1}$ and $\frac{\kappa}{\mu}\frac{\partial P_{p_{i,j_0+\frac{1}{2}}}^{n+1}}{\partial y} = -V_{p_{i,j_0+\frac{1}{2}}}^{n+1}$ in (4.60), then it gets

$$\begin{aligned} c_p \sum_{i=1}^{I}\sum_{j=1}^{j_0} \frac{P_{p_{i,j}}^{n+1} - P_{p_{i,j}}^{n}}{\Delta t} &= \frac{\kappa}{\mu}\sum_{j=1}^{j_0}\left(g_{p_{b,j}}^{n+1} - g_{p_{a,j}}^{n+1}\right)\Delta y - \sum_{i=1}^{I}\left(V_{p_{i,j_0+\frac{1}{2}}}^{n+1} + \frac{\kappa}{\mu} g_{p_{i,c}}^{n+1}\right)\Delta x \\ &+ \sum_{i=1}^{I}\sum_{j=1}^{j_0} f_{p_{i,j}}^{n+1}\Delta x \Delta y \end{aligned} \tag{4.61}$$

Using interface condition (4.51), multiplying with Δt and summing n from 0 to $N-1$; we get (4.54). This ends the proof. □

4.4 Numerical Simulations

In this section, we take numerical experiments to show the convergence of the proposed scheme and effectiveness of scheme from several realistic problems.

4.4.1 Model Problem

To verify the numerical convergence of our purposed numerical scheme (4.43)-(4.52), we solve model problems by the scheme. The numerical errors in L_2 norm are defined by

$$\|u - U\|_2 = \left(\sum_{i=0}^{I}\sum_{j=j_0+1}^{J}\left(u_{i+\frac{1}{2},j}^{n+1} - U_{i+\frac{1}{2},j}^{n+1}\right)^2 \Delta x \Delta y\right)^{\frac{1}{2}}$$

,

$$\|v-V\|_2=\left(\sum_{i=1}^{I}\sum_{j=j_0}^{J}\left(v_{i,j+\frac{1}{2}}^{n+1}-V_{i,j+\frac{1}{2}}^{n+1}\right)^2\Delta x\Delta y\right)^{\frac{1}{2}},$$

$$\left\|u_{p-U_p}\right\|_2=\left(\sum_{i=0}^{I}\sum_{j=1}^{j_0}\left(u_{p_{i+\frac{1}{2},j}}^{n+1}-U_{p_{i+\frac{1}{2},j}}^{n+1}\right)^2\Delta x\Delta y\right)^{\frac{1}{2}},$$

$$\|v_p-V_p\|_2=\left(\sum_{i=1}^{I}\sum_{j=0}^{j_0-1}\left(v_{p_{i,j+\frac{1}{2}}}^{n+1}-V_{p_{i,j+\frac{1}{2}}}^{n+1}\right)^2\Delta x\Delta y\right)^{\frac{1}{2}},$$

$$\|p-P\|_2=\left(\sum_{i=1}^{I}\sum_{j=j_0+1}^{J}\left(p_{i,j}^{n+1}-P_{i,j}^{n+1}\right)^2\Delta x\Delta y\right)^{\frac{1}{2}},$$

and

$$\|p_p-P_p\|_2=\left(\sum_{i=1}^{I}\sum_{j=0}^{j_0}\left(p_{p_{i,j}}^{n+1}-P_{p_{i,j}}^{n+1}\right)^2\Delta x\Delta y\right)^{\frac{1}{2}},$$

where u, v, p, u_p, v_p, p_p are exact solutions, U, V, P, U_p, V_p, P_p are numerical solutions.

Example 4.1: Consider the Stokes flow in $-0.5 \leq x \leq 0.5, 0 \leq y \leq 1$ and the Darcy flow in $-0.5 \leq x \leq 0.5, -1 \leq y \leq 0$, the exact solution is given by

$$u(x,y,t)=-\cos(\pi x)\sin(\pi y)e^t,$$

$$v(x,y,t)=\sin(\pi x)\cos(\pi y)e^t$$

$$p(x,y,t)=\frac{1}{2}\sin(\pi x)\cos(\pi y)e^t,$$

$$p_p(x,y,t)=\frac{1}{2}\ln\left[e^{(e^t(1-y)\sin(\pi x))}-2y^2e^t\sin(\pi x)\right] \tag{4.62}$$

with parameters $\mu = \frac{1}{4}, \nu = 1, c_p = 1, \kappa = \frac{1}{2}$ and $\alpha = \sqrt{\frac{1}{2}}$. The appropriate external forces in free flow can be derived by substituting exact solutions into the momentum equation (4.1)

$$f_u(x, y, t) = \cos(\pi x) \left(\frac{\pi}{2} \cos(\pi y) - (1 + 2\pi^2\nu) \sin(\pi y) \right) e^t,$$

and

$$f_v(x, y, t) = \sin(\pi x) \left((1 + 2\pi^2\nu) \cos(\pi y) - \frac{\pi}{2} \sin(\pi y) \right) e^t$$

Similarly, the source term in porous media can be obtained by substituting exact solution of p_p into the equation (4.3).

Table 4.1: Space discretization of the fluid horizontal velocity U, vertical velocity V and V_Γ in free flow at $\Delta t = \frac{1}{2}\Delta x^2, T = 1, N_y = 2N_x$.

N$_x$	$\|u - U\|_2$	Rate	$\|v - V\|_2$	Rate	$\|v_\Gamma - V_\Gamma\|_2$	Rate
40	2.1331E-03	-	1.9988E-03	-	4.7664E-03	-
80	6.0852E-04	1.7527	5.8197E-04	1.7173	1.3668E-03	1.7436
160	1.6310E-04	1.8655	1.6117E-04	1.8055	3.7042E-04	1.8449
200	9.5096E-05	1.9295	9.4897E-05	1.9107	2.1925E-04	1.9007
240	6.7004E-05	1.9712	6.7998E-05	1.9383	1.5839E-04	1.9226

The exact solution given in Example 4.1 satisfies the interface conditions equations (4.5)-(4.7). The interface is at $y = 0$, also we consider Dirichlet boundary condition at the external boundary of the domain which is obtained from the analytical solution. The convergent tests are carried out for all primary variables U, V, P and P_p as well as U_p and V_p. Uniform step size with $\Delta x = \Delta y$ (where $\Delta x = \frac{1}{N_x}, \Delta y = \frac{2}{N_y}$) in space

Table 4.2: Space discretization of the fluid horizontal velocity U_p and vertical velocity V_p in porous media at $\Delta t = \frac{1}{2}\Delta x^2, T = 1, N_y = 2N_x$

N$_x$	$\|u_p - U_p\|_2$	Rate	$\|v_p - V_p\|_2$	Rate
40	2.2352E-02	-	1.5596E-02	-
80	5.9594E-03	1.8754	4.0219E-03	1.9389
160	1.5431E-03	1.9340	1.0049E-03	2.0011
200	9.0936E-04	1.9090	6.0076E-04	1.8818
240	6.3678E-04	1.9834	4.2765E-04	1.9511

Table 4.3: Space discretization of pressure P in free flow and pressure P_p in porous media at $\Delta t = \frac{1}{2}\Delta x^2, T = 1, N_y = 2N_x$

N$_x$	$\|p - P\|_2$	Rate	$\|p_p - P_p\|_2$	Rate
40	5.4438E-02	-	2.2857E-03	-
80	2.7408E-02	0.9931	5.8914E-04	1.9398
160	1.3763E-02	0.9957	1.4591E-04	2.0188
200	1.0982E-02	1.0026	8.5968E-05	1.9094
240	9.1895E-03	0.9985	6.0394E-05	1.9770

Table 4.4: Time discretization of the fluid horizontal velocity U, vertical velocity V and pressure P in free flow at $\Delta x = \Delta y = \frac{1}{320}, T = 1$.

Δt	$\|u - U\|_2$	Rate	$\|v - V\|_2$	Rate	$\|v_\Gamma - V_\Gamma\|_2$	Rate
1.00×10^{-2}	3.4154E-01	-	2.3032E-01	-	9.2458E-01	-
5.00×10^{-3}	1.9787E-01	0.8631	1.3379E-01	0.8607	5.5291E-01	0.8361
2.25×10^{-3}	1.1044E-01	0.9477	7.0925E-02	0.9432	2.9986E-01	0.9219
1.25×10^{-3}	5.3083E-02	0.9833	3.6311E-02	0.9766	1.5570E-01	0.9629
6.25×10^{-4}	2.6661E-02	0.9955	1.8331E-02	0.9904	7.9213E-02	0.9828

discretization is considered in all refinement with time step size $\Delta t = \frac{1}{2}\Delta x^2$. The grid refinement starts the step size from $\frac{1}{40}$ and decreases up to $\frac{1}{240}$ in space discretization. The computations of time are performed up to time at $T = 1$. In addition, errors and convergent rate in L_2 norm for $(U, V, V_\Gamma), (U_p, V_p)$ and (P, P_p) are summarized in Tables

Table 4.5: Time discretization of the fluid horizontal velocity U_p, vertical velocity V_p and pressure P_p in porous media at $\Delta x = \Delta y = \frac{1}{320}, T = 1$.

Δt	$\|u_p - U_p\|_2$	Rate	$\|v_p - V_p\|_2$	Rate	$\|p_p - P_p\|_2$	Rate
1.00×10^{-2}	4.4932E-01	-	3.851E-01	-	3.9816E-02	-
5.00×10^{-3}	2.5233E-01	0.8904	2.2920E-01	0.8402	2.1386E-02	0.9309
2.50×10^{-3}	1.3698E-01	0.9211	1.2927E-01	0.8865	1.1196E-02	0.9550
1.25×10^{-3}	7.2229E-02	0.9482	6.9808E-02	0.9254	5.7522E-03	0.9732
6.25×10^{-4}	3.7090E-02	0.9737	3.6339E-02	0.9605	2.8247E-03	1.0182

Table 4.6: Mass error for pressure in porous media at $\Delta x = \Delta y = \frac{1}{40}, \Delta t = \frac{1}{4}\Delta x^2, \kappa = 0.5, \alpha = \frac{1}{\sqrt{2}}, \mu = 0.25$.

T\\c_p	0.01	0.05	0.10	0.50	1.00
$T = 0.10$	6.3838E-16	1.5266E-15	2.5258E-15	1.8318E-15	8.0491E-16
$T = 0.25$	1.7486E-15	4.1078E-15	7.1332E-15	4.9960E-15	2.5258E-15
$T = 0.50$	3.8858E-15	9.2149E-15	1.7319E-14	1.2212E-14	6.6058E-15
$T = 0.75$	6.1062E-15	1.3323E-14	3.2752E-14	1.9540E-14	1.0547E-14
$T = 1.00$	7.7716E-15	2.0428E-14	5.2847E-14	2.9421E-14	1.8540E-14

Table 4.7: Total mass error at the interface where $\Delta x = \Delta y = \frac{1}{40}, \Delta t = \frac{1}{4}\Delta x^2, \kappa = 0.5, \alpha = \frac{1}{\sqrt{2}}, \mu = 0.25$

T\\c_p	0.01	0.05	0.10	0.50	1.00
$T = 0.10$	3.4694E-15	5.1547E-16	6.9936E-16	4.9519E-15	5.3612E-15
$T = 0.25$	6.9388E-15	3.9039E-15	7.2240E-15	8.9390E-15	9.2307E-15
$T = 0.50$	9.2287E-15	2.1966E-14	6.2889E-15	4.2539E-15	1.9660E-14
$T = 0.75$	2.9837E-14	3.7243E-15	4.3786E-15	3.7868E-14	5.4297E-15
$T = 1.00$	2.3939E-14	3.5371E-14	8.4799E-15	1.8396E-14	4.7992E-14

4.1, 4.2, and 4.3 respectively. These results demonstrate second-order convergence in space for velocity and pressure in porous media and second-order convergence in space for velocity in free flow, however, the pressure in free flow is of first-order convergence in space.

To test the convergence in time, the space size is taken small enough as $\Delta x = \Delta y = \frac{1}{320}$; and the computations are with different time step sizes $\Delta t = 0.01, 0.005, 0.0025, 0.00125$ and 0.000625. The errors and convergent rate in L_2 norm of (U, V, P) and (U_p, V_p, P_p) are summarized in Tables 4.4 and 4.5 at $T = 1$. Results show first order convergent in time. Table 4.6 shows the errors of pressure mass in porous medium with different time level and compressibility parameter values, it clearly shows that our scheme satisfies conservation of mass where the errors of mass have reached within accuracy 10^{-14} which reaches the machine precision. Having conservation of mass at interface, the sum of mass flow $\sum\sum V^{n+1}_{i,j_0+\frac{1}{2}}\Delta x\Delta t$ across interface must be zero due to the boundary conditions of free flow in this example. Table 4.7 justifies that sum of mass at interface Γ is upto the machine accuracy (at least 10^{-14}) by taking different time level and compressibility parameter values.

Example 4.2: Consider the stokes flow in $0 \le x \le 1, 0 \le y \le 1$ and the Darcy flow in $0 \le x \le 1, -1 \le y \le 0$, the exact solution is given by

$$u(x, y, t) = \left[8(x^4 - 2x^3 + x^2)(4y^3 - 3y^2)\right] e^{-t},$$

$$v(x, y, t) = -\left[8(4x^3 - 6x^2 + 2x)(y^4 - y^3)\right] e^{-t},$$

$$p(x, y, t) = \left[(x(x-1))^2(y(y-1))^2 - 1\right] e^{-t},$$

$$p_p(x, y, t) = \left[(x(x-1))^2y^2 + \frac{y^3}{3} - 1\right] e^{-t} \tag{4.63}$$

with parameters $\nu = 1, c_p = 1, \kappa = 1$ and $\alpha = 1$. The appropriate external forces in free flow can be derived by substituting exact solutions into the momentum equation (4.1)

$$f_u(x, y, t) = -\big[8\{(x^4 - 2x^3 + x^2) + 2\nu(6x^2 - 6x + 1)\}(4y^3 - 3y^2) +$$

$$48\nu(x^4 - 2x^3 + x^2)(4y - 1) - (4x^3 - 6x^2 + 2x)(y^4 - 2y^3 + y^2)]e^{-t}$$

and

$$f_v(x, y, t) = \big[16\{(2x^3 - 3x^2 + x) + 6\nu(2x - 1)\}(y^4 - y^3) +$$

$$96\nu(2x^3 - 3x^2 + x)(2y^2 - y) + (x^4 - 2x^3 + x^2)(4y^3 - 6y^2 + 2y)]e^{-t}$$

Similarly, the source term in porous media can be obtained by substituting exact solution of p_p into the equation (4.3).

$$f_p(x, y, t) = -\left[c_p\{(x(x-1))^2 y^2 + \frac{y^3}{3} - 1\} + 2\kappa\{(6x^2 - 6x + 1)y^2 + (x(x-1))^2 + y\}\right] e^{-t}.$$

The analytic solution of Example 4.2 satisfies the interface conditions given in (4.5)-(4.7). The interface is at $y = 0$, and we consider Dirichlet boundary condition at the external boundary of the domain. The spatial accuracy for all primitive variables U, V, P and P_p and the variables U_p and V_p of Example of 4.2 is studied in Tables 4.8, 4.9, 4.10 in different meshes with uniform step size $\Delta x = \Delta y$ (where $\Delta x = \frac{1}{N_x}, \Delta y = \frac{2}{N_y}$ and $N_y = 2N_x$)and time step size $\Delta t = \Delta x^2$. The grid refinement starts from the step size $\frac{1}{20}$

Table 4.8: Space discretization of the fluid horizontal velocity U, vertical velocity V and V_Γ in free flow at $\Delta t = \Delta x^2, T = 1, N_y = 2N_x$

N$_x$	$\|u - U\|_2$	Rate	$\|v - V\|_2$	Rate	$\|v_\Gamma - V_\Gamma\|_2$	Rate
20	3.4900E-04	-	4.0431E-04	-	5.4941E-04	-
40	8.7407E-05	2.0041	9.7141E-05	2.0810	1.1731E-04	2.3586
80	2.1840E-05	2.0012	2.3497E-05	2.0671	2.5834E-05	2.2705
160	5.4749E-06	1.9946	6.0907E-06	1.9289	5.6285E-06	2.2981
320	1.3726E-06	1.9943	1.5389E-06	1.9789	1.3904E-06	2.0240

Table 4.9: Space discretization of the fluid horizontal velocity U_p and vertical velocity V_p in porous media at $\Delta t = \Delta x^2, T = 1, N_y = 2N_x$.

N$_x$	$\|u_p - U_p\|_2$	Rate	$\|v_p - V_p\|_2$	Rate
20	3.0829E-04	-	3.6554E-04	-
40	7.6830E-05	2.0063	8.5734E-05	2.1318
80	1.9090E-05	2.0123	2.0897E-05	2.0513
160	4.7551E-06	2.0074	5.4478E-06	1.9179
320	1.1876E-06	2.0020	1.3966E-06	1.9504

Table 4.10: Space discretization of pressure P in free flow and pressure P_p in porous media at $\Delta t = \Delta x^2, T = 1.N_y = 2N_x$

N$_x$	$\|p - P\|_2$	Rate	$\|p_p - P_p\|_2$	Rate
20	9.7015E-03	-	1.6007E-03	-
40	3.8687E-03	1.2538	3.6806E-04	2.1745
80	1.3915E-03	1.3901	9.0373E-05	2.0003
160	5.2671E-04	1.3209	2.4968E-05	1.8098
320	2.0713E-04	1.2714	6.6521E-06	1.8767

and decreases up to $\frac{1}{320}$ in space discretization. The computations of time are performed up to time at $T = 1$. We can see that the spatial orders of convergence are of second order in L_2 norms except in pressure in free flow. For the temporal convergence, we take small enough to $\Delta x = \Delta y = \frac{1}{320}$ and numerical errors are generated by using different

Table 4.11: Time discretization of the fluid horizontal velocity U, vertical velocity V and pressure P in free flow at $\Delta x = \Delta y = \frac{1}{320}, T = 1$.

Δt	$\|u - U\|_2$	Rate	$\|v - V\|_2$	Rate	$\|v_\Gamma - V_\Gamma\|_2$	Rate
2.00×10^{-2}	6.7776E-03	-	3.7735E-03	-	3.6992E-04	-
1.00×10^{-2}	3.5668E-03	0.9501	2.1770E-03	0.8667	1.8170E-04	1.0179
5.00×10^{-3}	1.8356E-03	0.9716	1.1927E-03	0.9126	9.0331E-05	1.0057
2.50×10^{-3}	9.3179E-04	0.9850	6.2981E-04	0.9469	4.4237E-05	1.0210
1.25×10^{-4}	4.6955E-04	0.9922	3.2477E-04	0.9696	2.0311E-05	1.0879

Table 4.12: Time discretization of the fluid horizontal velocity U_p, vertical velocity V_p and pressure P_p in porous media at $\Delta x = \Delta y = \frac{1}{320}, T = 1$.

Δt	$\|u_p - U_p\|_2$	Rate	$\|v_p - V_p\|_2$	Rate	$\|p_p - P_p\|_2$	Rate
2.00×10^{-2}	2.0726E-03	-	1.6317E-04	-	6.5106E-03	-
1.00×10^{-2}	1.0394E-03	0.9970	6.5053E-5	1.2541	3.3225E-03	0.9798
5.00×10^{-3}	5.2069E-04	0.9981	2.8576E-05	1.1382	1.6786E-03	0.9897
2.50×10^{-3}	2.6062E-04	0.9989	1.3392E-05	1.0669	8.4375E-04	0.9947
1.25×10^{-3}	1.3038E-04	0.9995	6.4905E-06	1.0317	4.2299E-04	0.9974

Table 4.13: Mass error for pressure in porous media at $\Delta x = \Delta y = \frac{1}{60}, \Delta t = \frac{1}{4}\Delta x^2, \kappa = 1, \alpha = 1, \mu = 1$.

T\ c_p	0.001	0.01	0.05	0.1	1.00
$T = 0.10$	7.5806E-16	1.9608E-15	1.9050E-15	1.8979E-15	1.8918E-15
$T = 0.25$	6.2924E-15	4.8364E-15	4.7068E-15	4.6905E-15	4.6759E-15
$T = 0.50$	1.1797E-14	9.2005E-15	8.9695E-15	8.9406E-15	8.9147E-15
$T = 0.75$	1.6616E-14	1.3133E-14	1.2822E-14	1.2783E-14	1.4538E-14
$T = 1.00$	2.0901E-14	1.6726E-14	2.3354E-14	1.5307E-14	1.6265E-14

Δt as shown in Table 4.11 and Table 4.12. Numerical results of L_2 norm of (U, V, P) and (U_p, V_p, P_p) confirm that the scheme is of first order convergent in time. The pressure mass errors in porous media with different time and compressibility parameter values are shown in Table 4.13. It shows that our proposed scheme preserves mass; where the

Table 4.14: Total mass error at the interface where $\Delta x = \Delta y = \frac{1}{60}, \Delta t = \frac{1}{4}\Delta x^2, \kappa = 1, \alpha = 1, \mu = 1$.

T\\c_p	0.001	0.01	0.05	0.1	1.00
$T = 0.10$	8.5927E-15	1.9867E-14	1.9351E-14	1.9276E-14	1.9221E-14
$T = 0.25$	2.3654E-14	1.8438E-14	1.8042E-14	1.7962E-14	1.7885E-14
$T = 0.50$	2.0506E-14	1.6536E-14	1.6194E-14	1.6145E-14	1.6046E-14
$T = 0.75$	1.8143E-14	3.7925E-14	2.4564E-14	2.7598E-14	4.3297E-14
$T = 1.00$	1.6239E-14	1.3748E-14	1.3530E-14	1.3542E-14	1.3426E-14

errors of mass have reached at least accuracy of 10^{-14}. Since conservation of mass across the interface requires the mass flux leaving the free flow region to be equal to the mass flux entering the porous medium region. Thus, as equation (4.5), the sum of mass flow $\sum\sum V^{n+1}_{i,j_0+\frac{1}{2}}\Delta x\Delta t$ across interface must be zero due to the boundary conditions of free flow. Mass errors at the interface are listed in Table 4.14 where we presents in various time level and compressibility parameter values.

4.4.2 Real Model

Experiment 1 (Lid driven cavity problem)

The lid driven cavity is among the most popular problem in fluid flow systems which is extensively investigated because of certain flow features like boundary layer on the wall, separation and attachment of flow, vortices and bubbles. Here, Stokes-Darcy equations are solved in square domain where the upper boundary moves with a uniform tangential velocity $(u = U = 10, v = 0)$. The no-slip boundary conditions are applied in left and right side $(u = 0, v = 0)$ in free flow. At left, right and bottom boundaries of the porous

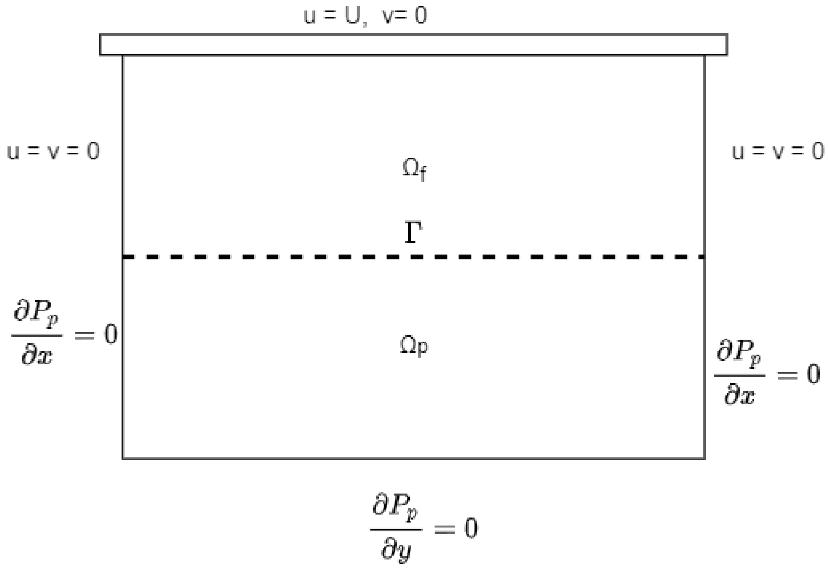

Figure 4.3: Lid driven cavity problem.

medium domain, the no flow condition $\frac{\partial p_p}{\partial n} = 0$ is considered. The boundary conditions are described in Fig. 4.3. The initial velocities and pressure of Ω_f and Ω_p are zero.

Our proposed scheme is applied and the computation is done in different time-marching $T = 1, 10$ and 50, starting the initial condition using mesh size of $\Delta x = \Delta y = \frac{1}{40}$ and time step $\Delta t = \frac{\Delta x^2}{2}$. Since velocities values of porous medium are much smaller comparing to surface flow velocities. Thus we enlarge sufficiently so that it can be visible in plotting of velocity vector field. Fig. 4.4 depict the comparison of the flow vector field using permeability $\kappa = 0.1$, and Figure 4.5 using permeability $\kappa = 1$.

To clarify further the vector velocity field, we plot both horizontal and vertical velocity separately at different time level in different parts of region Ω. Horizontal velocity (U or U_p) along x-axis and y-axis is shown in Fig. 4.6. Along x-axis at $y = 1.5125$ (almost middle part of free flow region) and at $y = 0.5125$ (almost middle part porous medium

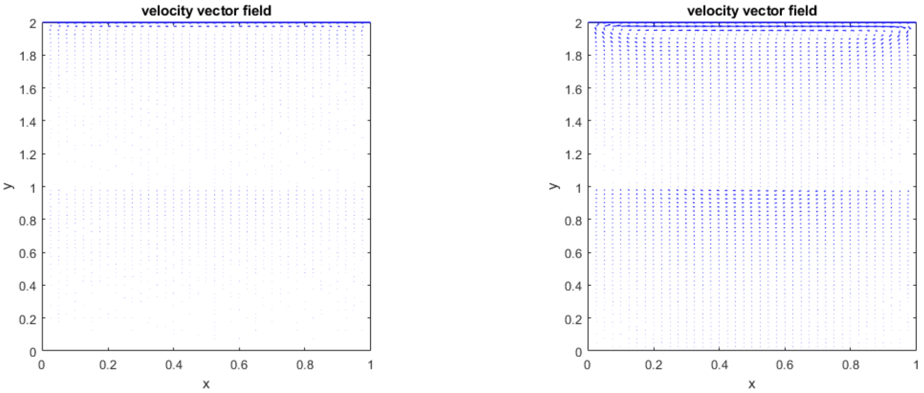

(a) T=1

(b) T=10

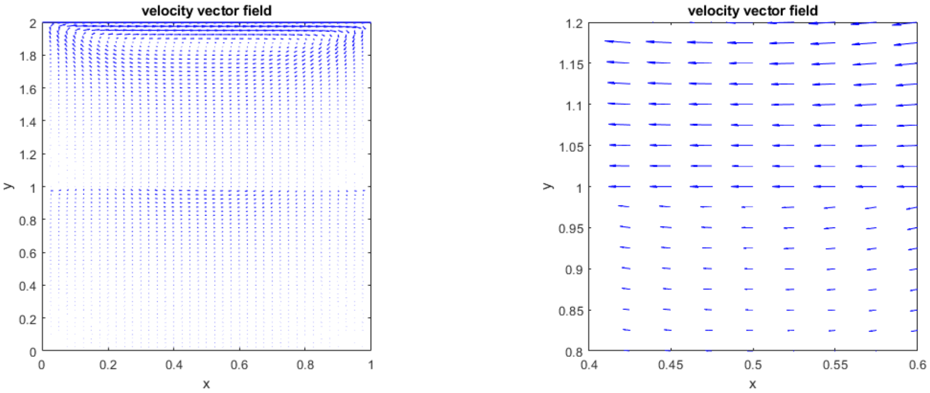

(c) T=50

(d) T=50

Figure 4.4: Velocity field in different time level lid driven cavity problem with $\rho = 10^3, \mu = 10^{-1}, \kappa = 10^{-1}, c_p = 10^{-4}$ and $\alpha = 1$

region), the value of (U or U_p) is negative i.e. fluid is moving from right to left (see Fig 4.6 a and c). But at $y = 1.9375$ (near moving wall where main vortex is appeared), the value of velocity is positive except near left and right wall (see Fig 4.6 b). Fig 4.6 d is the horizontal velocity at $x = 0.5$ which is middle part of region Ω along y-axis. Since in each level of given time, the direction of fluid flow is same; however, as time increases the absolute value of velocity (U) increases in free flow region and decreases the velocity (U_p) in porous medium region along x-axis. Also vertical velocity (V or V_p) along x-axis and y-axis is shown in Fig.4.7. The vertical velocity plot in various time level along

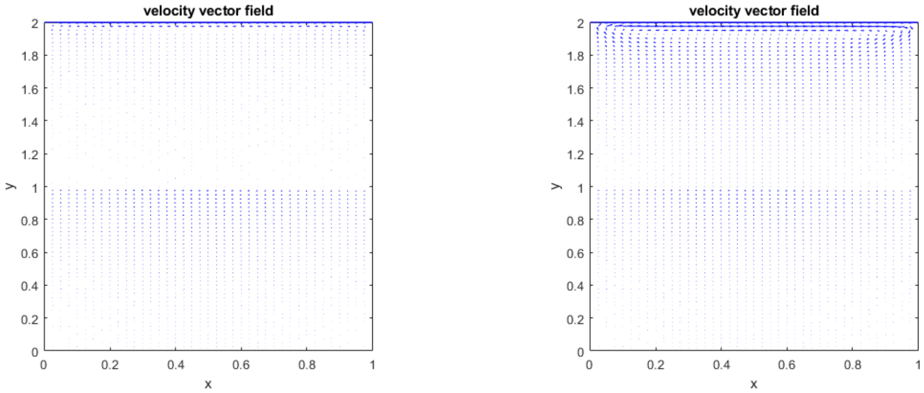

(a) T=1 (b) T=10

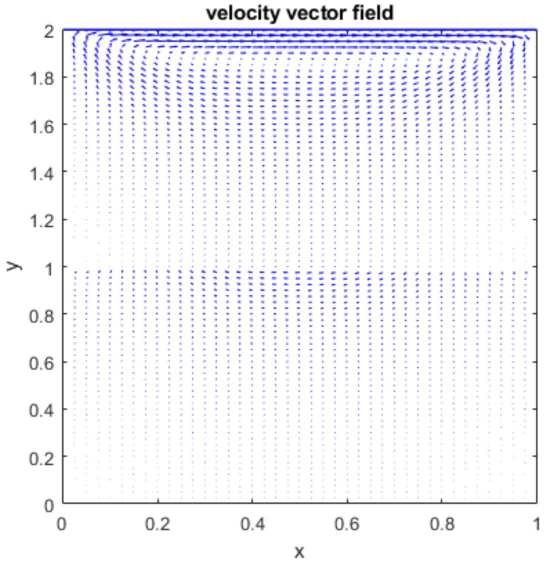

(c) T=50

Figure 4.5: Velocity field in different time level lid driven cavity problem with $\rho = 10^3, \mu = 10^{-1}, \kappa = 1, c_p = 10^{-4}$ and $\alpha = 0.1$

x-axis at $y = 1.5$ (middle part of Ω_f), $y = 0.5$ (middle part of Ω_p) and $y = 1.925$ (near moving wall) show that the fluid is entering from free flow region to porous medium region in right side and from porous medium region to free flow region in left side from half part of domain Ω (see Fig 4.7 a, b and c). At $x = 0.5125$ (almost middle part of Ω), the value of vertical velocity is close to 10^{-6} or smaller in all time level (see Fig 4.7 d). Thus, the fluid from surface region Ω_f flows into the porous medium region Ω_p

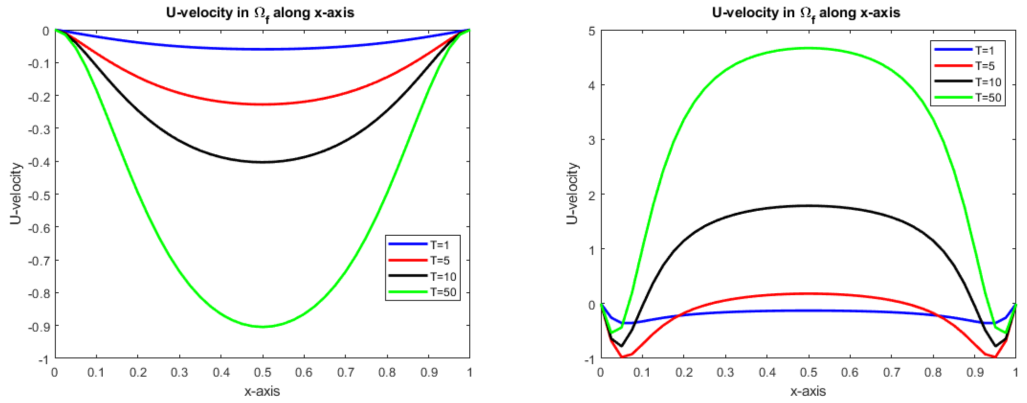

(a) At y=1.5125 (b) At y=1.9375

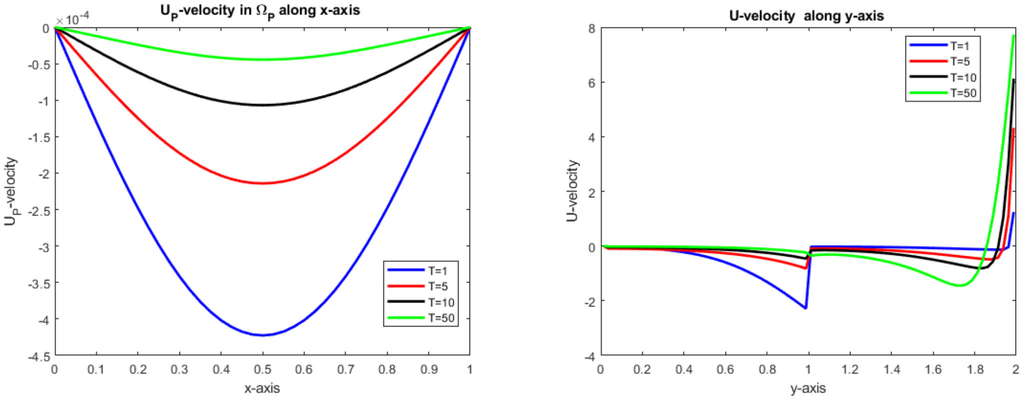

(c) At y=0.5125 (d) At x=0.5

Figure 4.6: Horizontal velocities plot in different time level in different parts of regions Ω_f, Ω_p and Ω along x-axis and y-axis with $\rho = 10^3, \mu = 10^{-1}, \kappa = 10^{-1}, c_p = 10^{-4}$ and $\alpha = 1$

from right side and out from porous medium to surface region from left side; and the flow also forms a vortex near the moving wall. Further, Table 4.15 shows the errors of pressure mass in the porous medium with different time level and permeability values which we can see clearly that the scheme satisfies conservation of mass where mass errors have reached within 10^{-16}. For conservation of mass, the sum of the mass flow across interface must be zero. Table 4.16 shows that our scheme ensures the discrete mass balance errors $\sum\sum V^{n+1}_{i,j_0+\frac{1}{2}}\Delta x\Delta t$ across the interface Γ almost upto machine accuracy

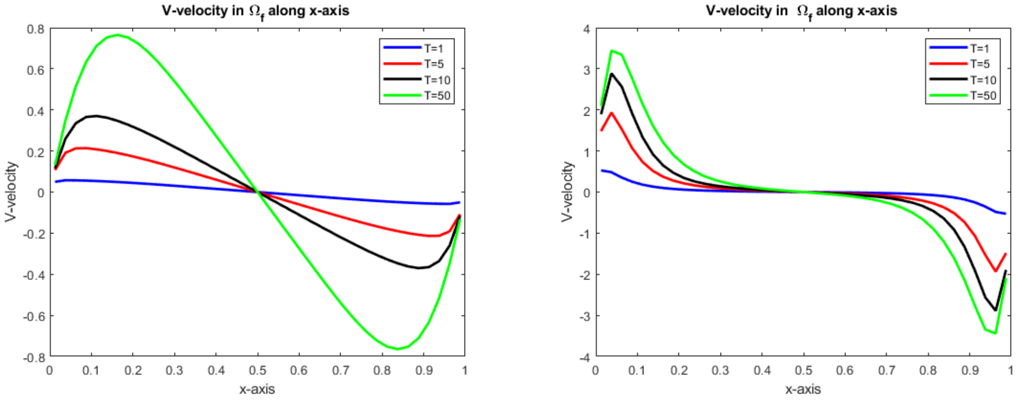

(a) At y=1.5 (b) At y=1.925

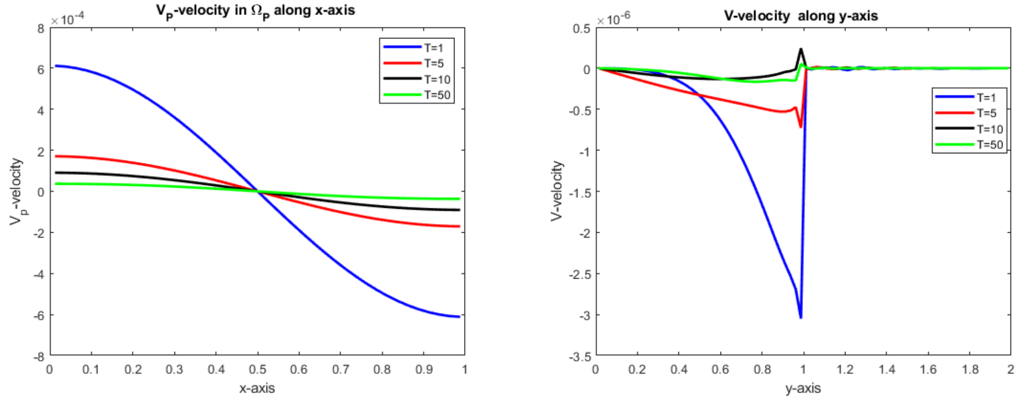

(c) At y=0.5 (d) At x=0.5125

Figure 4.7: Vertical velocities plot in different time level different parts of regions Ω_f, Ω_p and Ω along x-axis and y-axis with $\rho = 10^3, \mu = 10^{-1}, \kappa = 10^{-1}, c_p = 10^{-4}$ and $\alpha = 1$

Table 4.15: Mass error for pressure in porous media at $\Delta x = \Delta y = \frac{1}{40}, \Delta t = \frac{1}{4}\Delta x^2, c_P = 10^{-4}, \alpha = 1, \mu = 10^{-4}$.

T\ κ	10^{-4}	10^{-3}	10^{-2}	10^{-1}	10^{0}
$T = 0.10$	1.4867E-18	1.5468E-18	1.4262E-18	1.4962E-18	1.2925E-17
$T = 1.00$	1.4361E-18	1.3639E-18	9.6617E-18	6.0906E-18	6.0413E-18
$T = 5.00$	5.7793E-19	1.7347E-18	2.9739E-18	3.4451E-18	3.5687E-18
$T = 10.00$	4.6115E-18	6.6861E-18	7.9399E-18	8.4378E-18	8.6683E-18
$T = 20.00$	1.0883E-16	1.6529E-17	1.7830E-17	1.8405E-17	1.8731E-17

which is also confirmed by Fig.4.8 (symmetry curve axis at $y = 0$).

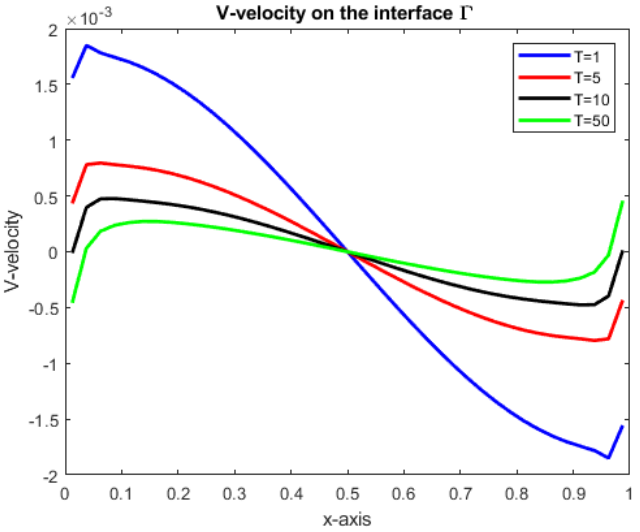

Figure 4.8: Vertical velocity at the interface Γ with different time level with $\rho = 10^3, \mu = 10^{-1}, \kappa = 10^{-1}, c_p = 10^{-4}$ and $\alpha = 1$.

Table 4.16: Total mass at interface Γ where $\Delta x = \Delta y = \frac{1}{40}, \Delta t = \frac{1}{4}\Delta x^2, c_P = 10^{-4}, \alpha = 1, \nu = 10^{-4}$.

T\\κ	10^{-4}	10^{-3}	10^{-2}	10^{-1}	10^{0}
$T = 0.10$	1.5263E-18	1.5849E-18	1.4592E-18	1.5237E-18	1.3272E-18
$T = 1.00$	1.5421E-18	1.5382E-18	1.5232E-18	1.5473E-18	1.5568E-18
$T = 5.00$	1.5396E-18	1.5463E-18	1.5523E-18	1.5398E-18	1.5481E-18
$T = 10.00$	1.3916E-18	1.5432E-18	1.5443E-18	1.5500E-18	1.5407E-18
$T = 20.00$	2.1938E-16	1.5391E-18	1.5577E-18	1.5413E-18	1.5446E-18

Experiment 2 (Inflow-outflow problem)

Another commonly utilized benchmark problem is inflow-outflow problem in order to observe whether proposed numerical scheme is working properly when surface flow is coupled with porous medium flow. A physical model is given in Fig. 4.9. We consider $\Omega_f = [0, 8] \times [1, 2], \Omega_p = [0, 8] \times [0, 1]$ and interface $\Gamma = (0, 8) \times \{1\}$. The no-slip boundary condition $(u = 0, v = 0)$ is applied in the top side of free flow $\partial\Omega_f = [0, 8] \times \{2\}$. The

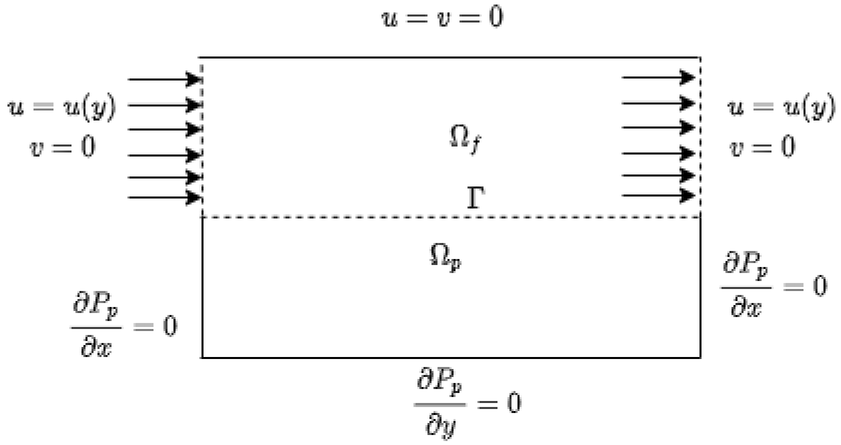

Figure 4.9: Inflow outflow problem.

inflow boundary condition at the left side of free flow region $\partial\Omega_f = \{0\} \times [1, 2]$ is given by

$$u = U(1 - 4(y - 1.5)^2), \qquad v = 0 \tag{4.64}$$

where $U = 10$ in this case. The outflow condition is prescribed as inflow at the right boundary. The remaining boundaries of the porous region ; the no-flux boundary condition $\nabla p_p.n = 0$ is imposed. The initial velocities and pressure of Ω_f and Ω_p are set to be zero.

The computation is done in different time-marching $T = 1, 10$ and 50, starting the initial condition using mesh size of $\Delta x = \Delta y = \frac{1}{40}$ and time step $\Delta t = \frac{\Delta x^2}{2}$. Fig. 4.10 shows the comparison of the flow vector field using permeability $\kappa = 1$, special storage coefficient $c_p = 10^{-4}$, kinematic viscosity $\nu = 10^{-4}$ and Beavers-Joseph parameter $\alpha = 1$. In each time level cases, the fluid from surface region Ω_f flows into the porous medium region Ω_p from left side and out from porous medium to surface region from right side

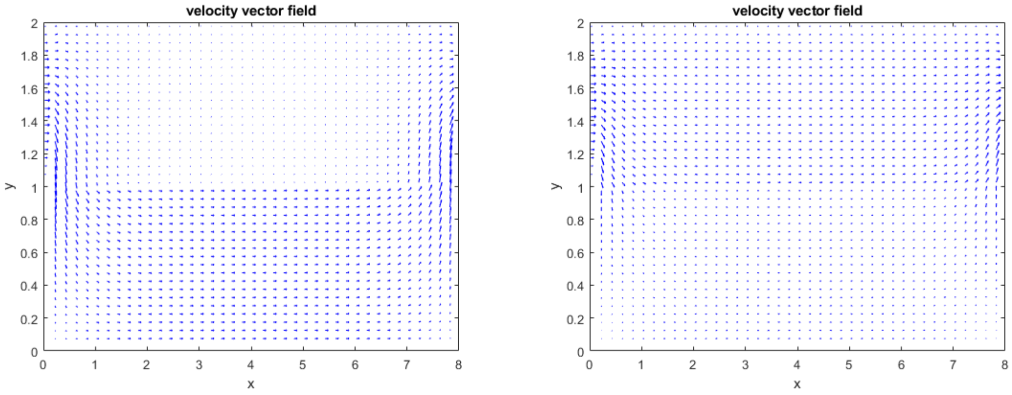

(a) T=1

(b) T=10

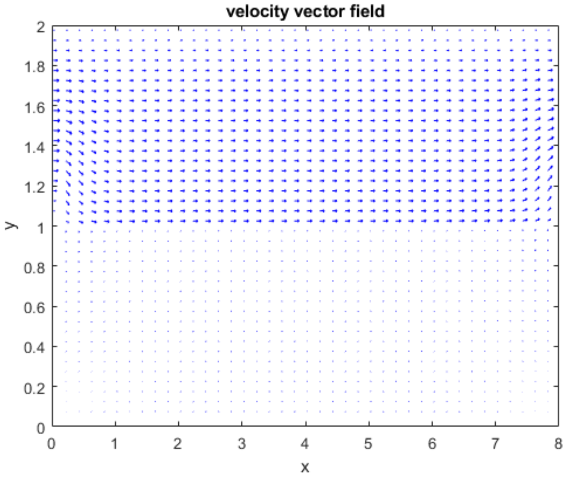

(c) T=50

Figure 4.10: Velocity field in different time level in inflow-outflow problem with $\nu = 10^{-3}, \kappa = 1, c_p = 10^{-4}$ and $\alpha = 1$.

as the natural flow nature. Moreover, when flow is in unsteady state (at beginning level of time), the main stream of flow appear towards porous medium but as flows reach at steady state (in long time), main stream of flow remain in surface region (see Fig. 4.10 a-c).

Furthermore, we plot both horizontal and vertical velocity separately at different time ($T = 1, 5, 10, 50$) in different parts of region Ω. Horizontal velocity (U or U_p) with various time marching along x-axis and y-axis is shown in Fig. 4.11. Along x-axis at

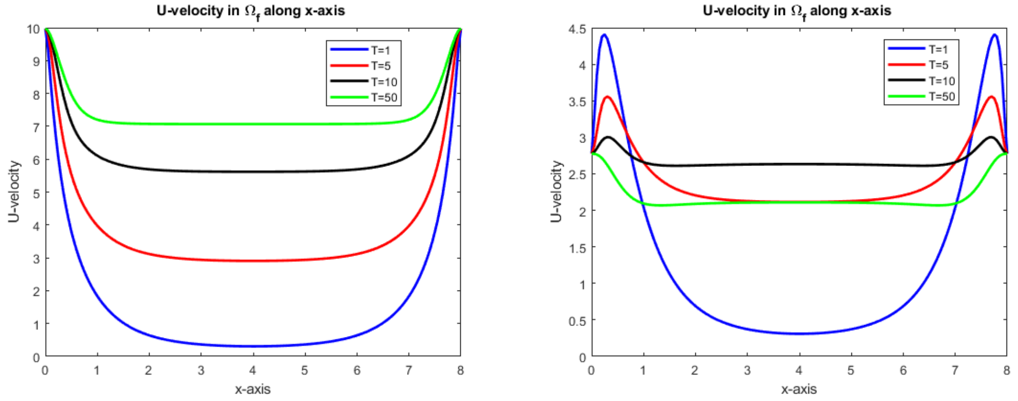

(a) At y=1.525 (b) At y=1.925

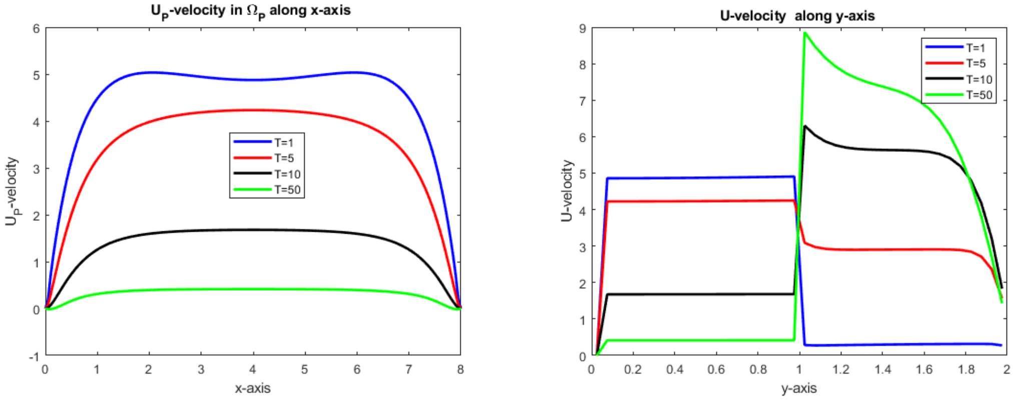

(c) At y=0.525 (d) At x=4.025

Figure 4.11: Horizontal velocities plot at different time level in different parts of regions Ω_f, Ω_p and Ω along x-axis and y-axis with $\nu = 10^{-3}, \kappa = 1, c_p = 10^{-4}$ and $\alpha = 1$.

$y = 1.525$ (almost middle part of free flow region) , at $y = 0.525$ (almost middle part porous medium region) and $y = 1.925$ (near top wall), the value of (U or U_p) is positive i.e. fluid is moving from left to right (see Fig 4.11 a-c). The results show that flow is more stable in middle of region than near the wall. Also in long time flow it becomes more and more stable and reaches the equilibrium level. Moreover, velocity value in porous media is higher than in free flow in the beginning time ($T = 1$) ; however increasing in time, the velocity value of porous media becomes much smaller than in free flow region (see Fig. 4.11 d). Next, vertical velocity (V or V_p) along x-axis and y-axis is shown in

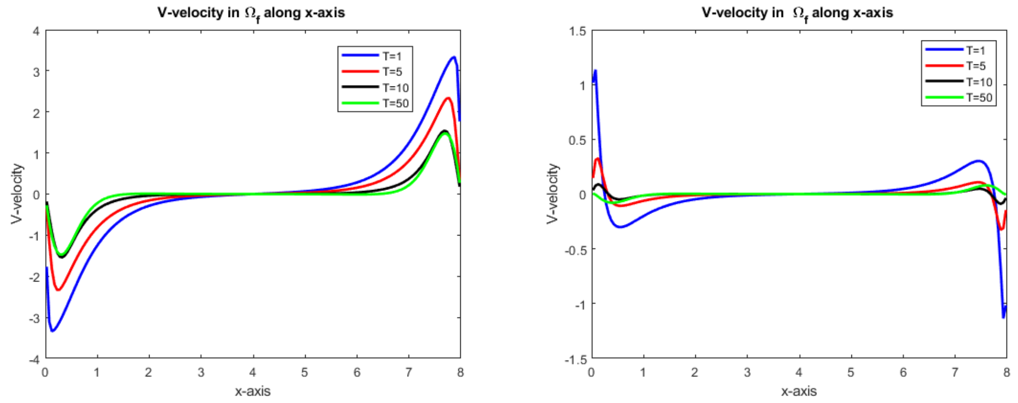

(a) At y=1.5 (b) At y=1.9

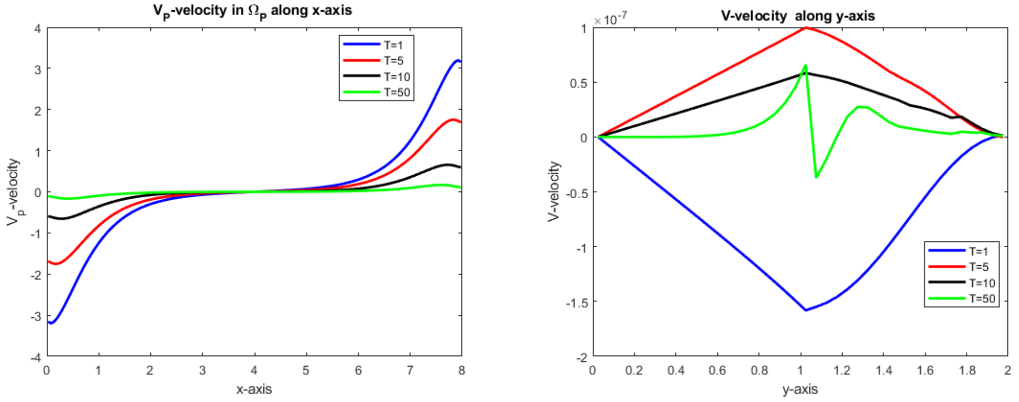

(c) At y=0.5 (d) At x=4

Figure 4.12: Vertical velocities plot at different time level in different parts of regions Ω_f, Ω_p and Ω along x-axis and y-axis with $\nu = 10^{-3}, \kappa = 1, c_p = 10^{-4}$ and $\alpha = 1$.

Fig. 4.12. The value of vertical velocity (V or V_p) is negative near left side wall region and positive near right side wall region (see Fig 4.12 a and c); although, it is almost opposite where flow is moving close by top wall (see Fig 4.12 b). Moreover, the net velocity value (V or V_p) is close zero as flow reaches to steady state (see Fig. 4.12 d).

Table 4.17 shows the errors of pressure mass in the porous medium with different time level and permeability values which we can see clearly that the scheme satisfies conservation of mass where mass error have reached within 10^{-16}. For conservation of mass, the sum of the mass flow across interface must be zero. Table 4.18 shows that

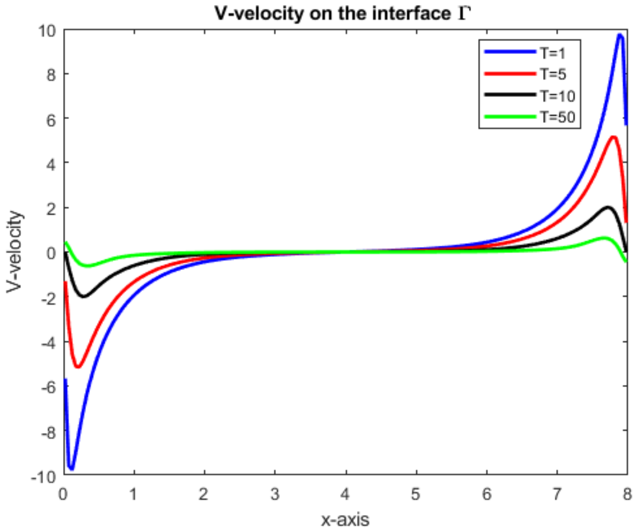

Figure 4.13: Vertical velocity at the interface with different time level with $\nu = 10^{-3}, \kappa = 1, c_p = 10^{-4}$ and $\alpha = 1$.

Table 4.17: Mass error for pressure in porous media at $\Delta x = \Delta y = \frac{1}{10}, \Delta t = \frac{1}{4}\Delta x^2, c_P = 10^{-4}, \alpha = 1, \mu = 10^{-3}$.

T\\κ	10^{-4}	10^{-3}	10^{-2}	10^{-1}	10^{0}
$T = 1$	5.0834E-17	4.1234E-17	7.3306E-17	2.5523E-16	1.8070E-16
$T = 2$	3.6288E-16	2.8924E-16	3.7583E-16	1.4229E-16	2.2341E-16
$T = 5$	9.3913E-16	2.4639E-16	2.9947E-16	2.5991E-16	1.2415E-16
$T = 10$	1.6832E-15	3.7444E-16	2.3858E-16	1.6210E-16	6.8591E-17
$T = 15$	2.2188E-16	4.6445E-16	4.3705E-16	1.1826E-16	3.9873E-17

Table 4.18: Total mass at interface Γ where $\Delta x = \Delta y = \frac{1}{10}, \Delta t = \frac{1}{4}\Delta x^2, c_P = 10^{-4}, \alpha = 1, \nu = 10^{-3}$.

T\\κ	10^{-4}	10^{-3}	10^{-2}	10^{-1}	10^{0}
$T = 1$	2.3735E-16	1.3932E-16	3.1124E-16	1.0417E-15	7.3493E-16
$T = 2$	3.9996E-16	1.1848E-15	1.5171E-15	6.2369E-16	8.70583E-16
$T = 5$	4.1668E-15	8.3627E-15	1.3559E-16	1.0405E-16	5.4411E-16
$T = 10$	8.2895E-15	1.7705E-16	7.2437E-16	8.6096E-16	4.2145E-16
$T = 15$	9.1894E-15	2.5518E-15	1.0505E-15	2.1519E-15	3.8819E-16

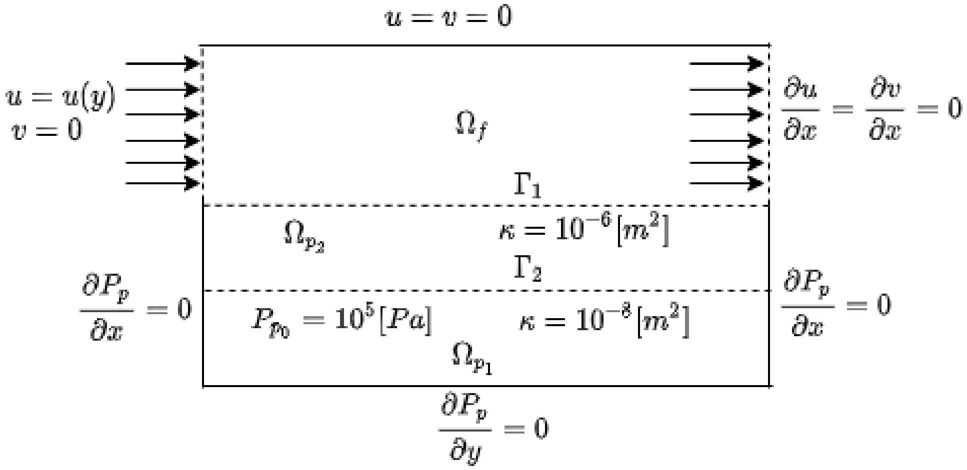

Figure 4.14: The coupled free flow and two layers porous media flow.

our scheme satisfies the discrete mass balance errors across the interface Γ almost upto machine accuracy which is also confirmed by Fig. 4.13 (symmetry curve axis at $y = 1$).

4.4.3 Realistic Problem

Experiment 3 (Inflow-outflow problem of free and two layers porous media flows)

The numerical simulations for the realistic problem are taken in this subsection. We consider the coupled domain $32m \times 2m$ presented in Fig. 4.14. The porous medium contains two highly permeable layer $[0, 32m] \times [0, 0.5m]$ and $[0, 32m] \times [0.5m, 1m]$. The fluid is water with density $\rho = 10^3[kg/m^3]$ and dynamic viscosity $\mu = 10^{-3}[Pas]$. The soil is isotropic with permeability $\kappa = 10^{-8}[m^2]$ in the bottom layer and the permeability $k = 10^{-6}[m^2]$ is in the upper layer of the porous medium. The soil compressibility parameter is $c_p = 10^{-4}[1/Pa]$. The BeaversJoseph coefficient is $\alpha = 10^{-3}$. The gravitational effects

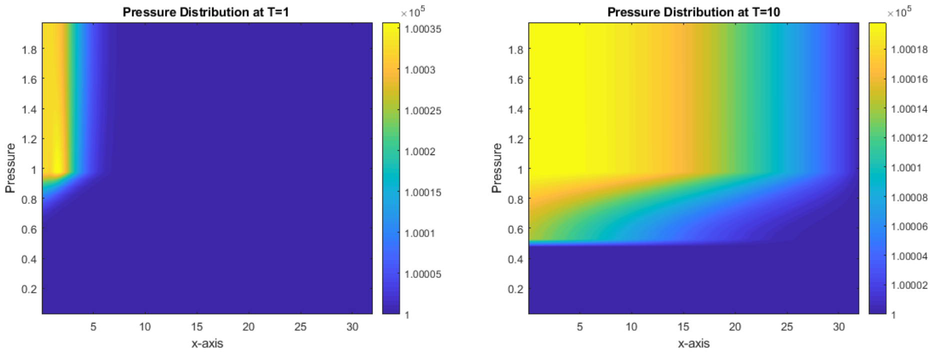

(a) T=1s (b) T=10s

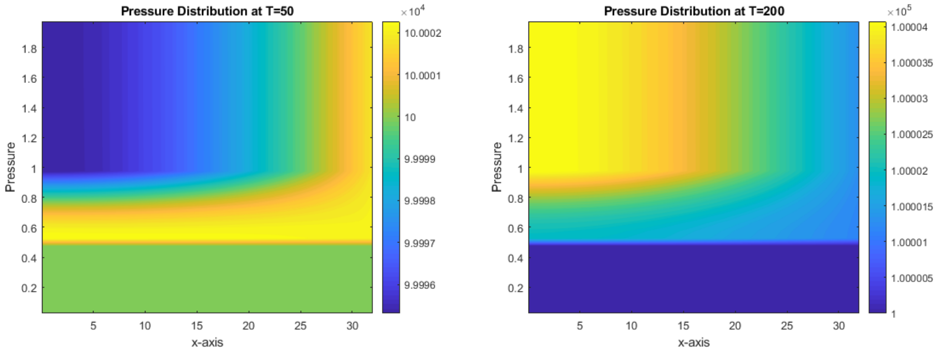

(c) T=50s (d) T=200s

Figure 4.15: Pressure distribution at different time level in the coupled domain with $\Delta x = \Delta y = 0.05$ and $\Delta t = 0.5\Delta x^2$.

are neglected. We consider the following coupled system as presented in Fig. 4.14,

$$\begin{cases} \frac{\partial \mathbf{u}}{\partial t} = -\nabla p + \nu \nabla^2 \mathbf{u}, & (x,y,t) \in \Omega_f \times (0,T], \\ \nabla.\mathbf{u} = 0, & (x,y,t) \in \Omega_f \times (0,T], \\ c_p \frac{\partial p_p}{\partial t} + \nabla.\mathbf{u}_p = 0, & (x,y,t) \in \Omega_p \times (0,T], \\ \mathbf{u}_p = -\frac{\kappa_1}{\mu} \nabla p_p, & (x,y,t) \in \Omega_{p_1} \times (0,T], \\ \mathbf{u}_p = -\frac{\kappa_2}{\mu} \nabla p_p, & (x,y,t) \in \Omega_{p_2} \times (0,T], \\ v = v_p, & (x,y,t) \in \Gamma_1 \times (0,T], \\ p - 2\nu \frac{\partial v}{\partial y} = p_p, & (x,y,t) \in \Gamma_1 \times (0,T], \\ u + \frac{\sqrt{\kappa_2}}{\alpha} \left(\frac{\partial v}{\partial x} + \frac{\partial u}{\partial y} \right) = 0, & (x,y,t) \in \Gamma_1 \times (0,T], \\ \left[p_p \right] = 0, \quad [\frac{\kappa}{\mu} p_{p_y}] = 0, & (x,y,t) \in \Gamma_2 \times (0,T], \end{cases}$$

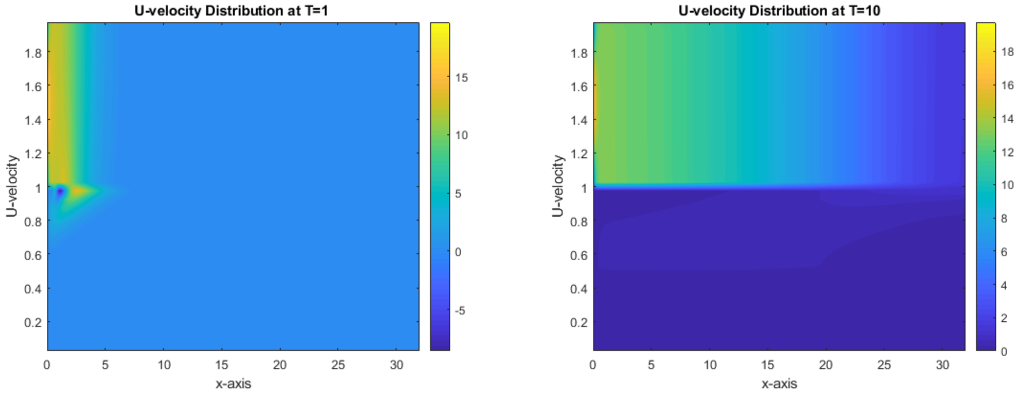

(a) T=1s (b) T=10s

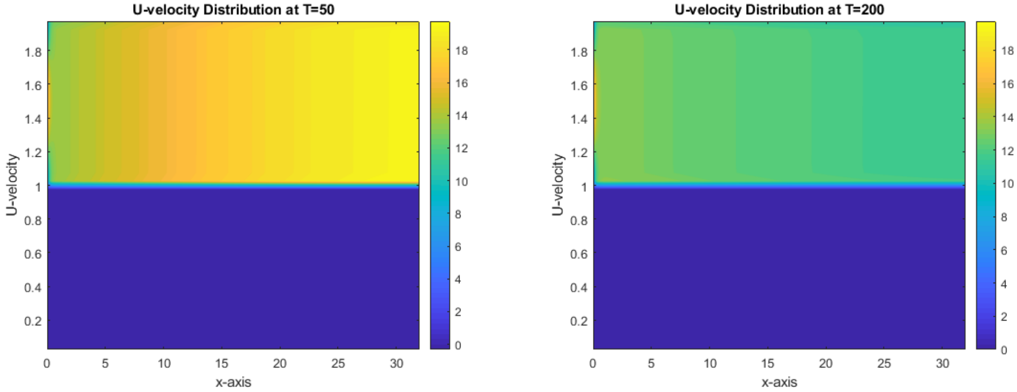

(c) T=50s (d) T=200s

Figure 4.16: U-velocity distribution at different time level in the coupled domain with $\Delta x = \Delta y = 0.05$ and $\Delta t = 0.5\Delta x^2$.

and the right side function $\mathbf{F}$ and f_p are zero; where Γ_1 is the interface between free flow and porous media flow and Γ_2 is the interface between two layers of porous media.

We choose zero free flow velocity $u_0 = 0, v_0 = 0$ and the atmospheric pressure $P_0 = 10^5[Pa]$ as initial conditions for pressure in both surface flow and porous medium. The set of boundary conditions is prescribed in Fig. 4.14. The inflow conditions at the left boundary of the free flow domain is taken same as Experiment 2, $u = U(1 - 4(y-1.1)^2)[m/s]$ with $U = 20$ and $v = 0$. The no-flow condition at the left boundary of the porous medium domain is given by $\partial p/\partial x = 0$ and the outflow conditions are

$\partial u/x = 0, v/\partial x = 0$. To demonstrate the effectiveness of our proposed scheme numerical

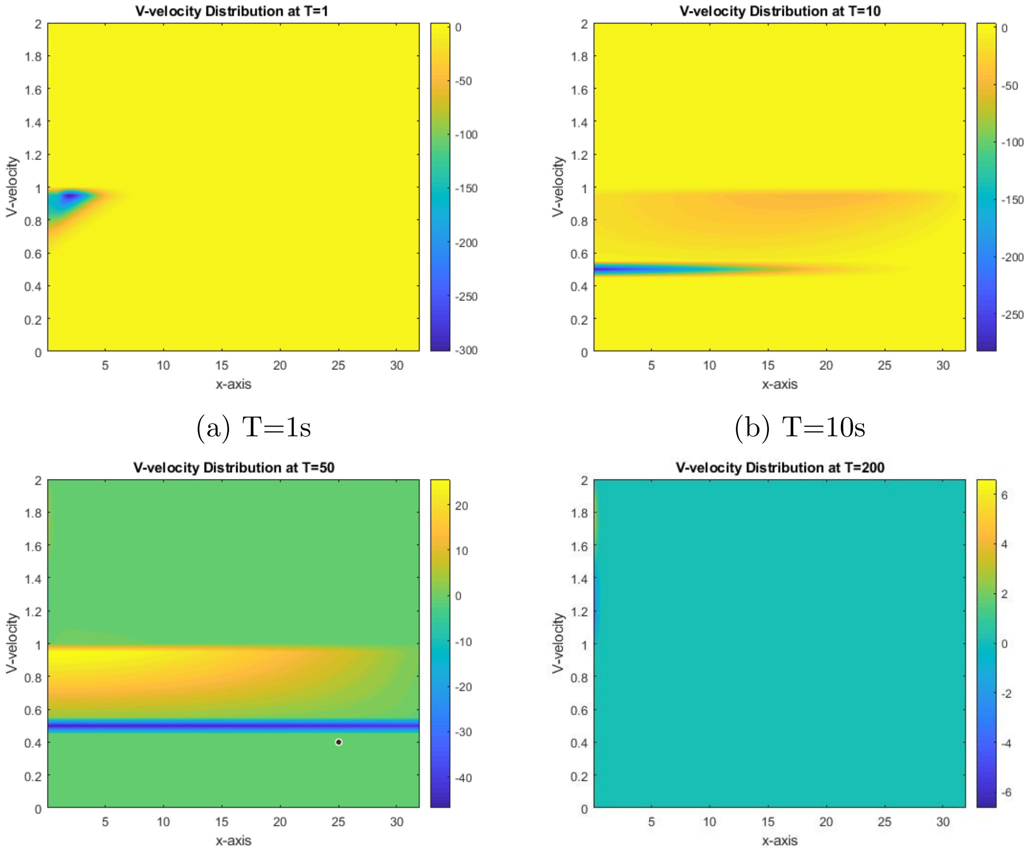

(a) T=1s (b) T=10s

(c) T=50s (d) T=200s

Figure 4.17: V-velocity distribution at different time level in the coupled domain with $\Delta x = \Delta y = 0.05$ and $\Delta t = 0.5\Delta x^2$.

simulations are done by our Pressure-velocity scheme for coupled free and porous media flow systems for $T = 1s$, 10s, 50s and 200s where the mass preservingg solution-flux scheme in chapter 3 is considered to solve layers problem in porous media. We use $\Delta x = \Delta y = 0.05$ and $\Delta t = 0.5\Delta x^5$. Finally numerical solutions for pressure and velocities in the coupled domain for realistic example at different times are produced. Pressure distribution distribution is shown in Fig. 4.15. The amount of inflow of water produces an increase of the pressure in the free flow domain and, as a result, a pressure difference in the porous medium generates the fluid flow in the porous layer. Since the upper layer of porous medium is more permeable than the lower one, the pressure is higher in upper layer region because the water can go through easier. Also by advancing time, the coupled system approaches towards steady state.

Horizontal velocity distribution is shown in Fig. 4.16. The horizontal velocity appears negative value (flow is in right to left direction) in small portion of region near inflow wall and free-porous interface Γ_1 at $T = 1$. Also, the value of horizontal velocity in free flow is much higher than in porous media. Further, as a flow approaches to a steady state, the horizontal velocity value becomes constant in free flow region (main stream flow region) except near inflow wall. Vertical velocity distribution is shown in Fig. 4.17. Fig. 4.17 shows that flow is moving faster toward porous media through interface Γ_1 near inflow wall at $T = 1$; but the flow is moving faster toward porous media through interface Γ_2 at $T = 10$. However, as a flow approaches to a steady state, the vertical velocity comes closer to zero. Also, vertical velocity value becomes almost same in whole region. Thus, Fig. 4.16 and Fig. 4.17 show that the whole flow system in inflow-outflow setting is dominated by horizontal velocity.

4.5 Conclusion

The interactions between the free flows and porous medium flows present commonly in science and engineering work. Therefore, there is increasing interest to simulate interactions in the free flow and porous medium systems. Only free flow or porous medium domains domains have been extensively studied, but a challenge of numerical solution arises in case of coupling between the flow models at the interfaces.

In this work, we have studied the time-dependent Stokes-Darcy problems with a set interface conditions to describe fluid flows and proposed a conservative pressure- velocity scheme for solving such the systems. We developed an efficient method to approximate the problem at the interface that ensures our scheme to preserve mass over the whole domain including across the interface. Numerical simulations were provided two model problems with known analytical solutions, two real problems and a realistic problem to show mass conservation and the convergence of the proposed algorithm in time and space sizes. The numerical results from two model problems showed that all primary variables are second order accurate in L_2 norm except the pressure in free flow which is first-order accurate in L_2 norm. Numerical results of two most popular benchmark problems in fluid flows (lid driven and inflow- outflow problem) and the realistic setting problem showed excellent performance of the proposed scheme.

Many extensions to this work are possible such as the proposed method provides a fundamental and flexible way in solving coupled Navier-Stokes and Darcy flow problems and it is readily extendible to multi-physics fluid flows for applications in various engineering analysis. It can be developed in multi-time step algorithms, using higher order schemes in time and application of various kinds of space discretization techniques in both flow domains. The two-fluid-phase porous medium systems can be considered to simulate evaporation from the soil influenced by the wind, wood drying or river interaction with unsaturated ground water aquifers.

Bibliography

[1] Abide, S., and Viazzo, S. A 2d compact fourth-order projection decomposition method. *Journal of Computational Physics 206*, 1 (2005), 252–276.

[2] Adams, L., and Li, Z. The immersed interface/multigrid methods for interface problems. *SIAM Journal on Scientific Computing 24*, 2 (2002), 463–479.

[3] Alloui, Z., Rebhi, R., Mamou, M., and Vasseur, P. Effects of quadratic drag on natural convection in a tilted porous layer with uniform heat flux from the side. *International Journal of Heat and Mass Transfer 115* (2017), 314–325.

[4] Arbogast, T., and Brunson, D. S. A computational method for approximating a darcy–stokes system governing a vuggy porous medium. *Computational Geosciences 11*, 3 (2007), 207–218.

[5] Attanayake, C., and Senaratne, D. Convergence of an immersed finite element method for semilinear parabolic interface problems. *Applied Mathematical Sciences 5*, 3 (2011), 135–147.

[6] Balmforth, N. J., and Mandre, S. Dynamics of roll waves. *Journal of Fluid Mechanics 514* (2004), 1–33.

[7] Bates, P., Chen, Z., Sun, Y., Wei, G.-W., and Zhao, S. Geometric and potential driving formation and evolution of biomolecular surfaces. *Journal of Mathematical Biology 59*, 2 (2009), 193.

[8] Beavers, G. S., and Joseph, D. D. Boundary conditions at a naturally permeable wall. *Journal of Fluid Mechanics 30*, 1 (1967), 197–207.

[9] Bell, J. B., Colella, P., and Glaz, H. M. A second-order projection method for the incompressible navier-stokes equations. *Journal of Computational Physics 85*, 2 (1989), 257–283.

[10] Benjamin, T. B. Wave formation in laminar flow down an inclined plane. *Journal of Fluid Mechanics 2*, 6 (1957), 554–573.

[11] Benney, D. Long waves on liquid films. *Journal of Mathematics and Physics 45*, 1-4 (1966), 150–155.

[12] Boyd, J. P. *Chebyshev and Fourier spectral methods.* Courier Corporation, 2001.

[13] Brock, R. R. Development of roll waves in open channels.

[14] Brown, D. L., Cortez, R., and Minion, M. L. Accurate projection methods for the incompressible navier–stokes equations. *Journal of Computational Physics 168*, 2 (2001), 464–499.

[15] Cao, Y., Gunzburger, M., Hu, X., Hua, F., Wang, X., and Zhao, W. Finite element approximations for stokes–darcy flow with beavers–joseph interface conditions. *SIAM Journal on Numerical Analysis 47*, 6 (2010), 4239–4256.

[16] Carr, E. J., and March, N. G. Semi-analytical solution of multilayer diffusion problems with time-varying boundary conditions and general interface conditions. *Applied Mathematics and Computation 333* (2018), 286–303.

[17] Carr, E. J., Turner, I., and Perre, P. Macroscale modelling of multilayer diffusion: using volume averaging to correct the boundary conditions. *Applied Mathematical Modelling 47* (2017), 600–618.

[18] Chorin, A. J. The numerical solution of the navier-stokes equations for an incompressible fluid. *Bulletin of the American Mathematical Society 73*, 6 (1967), 928–931.

[19] Chorin, A. J. Numerical solution of the navier-stokes equations. *Mathematics of Computation 22*, 104 (1968), 745–762.

[20] Craster, R. V., and Matar, O. K. Dynamics and stability of thin liquid films. *Reviews of Modern Physics 81*, 3 (2009), 1131.

[21] DAlessio, S., Pascal, J., and Jasmine, H. Instability in gravity-driven flow over uneven surfaces. *Physics of Fluids 21*, 6 (2009), 062105.

[22] Dauth, M., and Aksel, N. Breaking of waves on thin films over topographies. *Physics of Fluids 30*, 8 (2018), 082113.

[23] Dawson, C. N., and Dupont, T. F. Explicit/implicit, conservative domain decomposition procedures for parabolic problems based on block-centered finite differences. *SIAM Journal on Numerical Analysis 31*, 4 (1994), 1045–1061.

[24] De Monte, F. Transient heat conduction in one-dimensional composite slab. a naturalanalytic approach. *International Journal of Heat and Mass Transfer 43*, 19 (2000), 3607–3619.

[25] Discacciati, M. Domain decomposition methods for the coupling of surface and groundwater flows. Tech. rep., EPFL, 2004.

[26] Discacciati, M., Miglio, E., and Quarteroni, A. Mathematical and numerical models for coupling surface and groundwater flows. *Applied Numerical Mathematics 43*, 1-2 (2002), 57–74.

[27] Discacciati, M., and Quarteroni, A. Convergence analysis of a subdomain iterative method for the finite element approximation of the coupling of stokes and darcy equations. *Computing and Visualization in Science 6*, 2-3 (2004), 93–103.

[28] Ergun, S., and Orning, A. A. Fluid flow through randomly packed columns and fluidized beds. *Industrial & Engineering Chemistry 41*, 6 (1949), 1179–1184.

[29] Ervin, V., Jenkins, E., and Sun, S. Coupled generalized nonlinear stokes flow with flow through a porous medium. *SIAM Journal on Numerical Analysis 47*, 2 (2009), 929–952.

[30] Fedkiw, R. P., Aslam, T., Merriman, B., Osher, S., et al. A non-oscillatory eulerian approach to interfaces in multimaterial flows (the ghost fluid method). *Journal of Computational Physics 152*, 2 (1999), 457–492.

[31] Forchheimer, P. Wasserbewegung durch boden: Zeitschrift des vereines deutscher ingenieure, v. 45.

[32] Hauke, G. *An introduction to fluid mechanics and transport phenomena*, vol. 86. Springer, 2008.

[33] Hickson, R., Barry, S. I., Mercer, G. N., and Sidhu, H. Finite difference schemes for multilayer diffusion. *Mathematical and Computer Modelling 54*, 1-2 (2011), 210–220.

[34] Hill, A. A., and Straughan, B. Poiseuille flow in a fluid overlying a porous medium. *Journal of Fluid Mechanics. 603* (2008), 137–149.

[35] Horton, G., and Vandewalle, S. A space-time multigrid method for parabolic partial differential equations. *SIAM Journal on Scientific Computing 16*, 4 (1995), 848–864.

[36] Hou, S., and Liu, X.-D. A numerical method for solving variable coefficient elliptic equation with interfaces. *Journal of Computational Physics 202*, 2 (2005), 411–445.

[37] Jackson, A., Rybak, I., Helmig, R., Gray, W., and Miller, C. Thermodynamically constrained averaging theory approach for modeling flow and transport

phenomena in porous medium systems: 9. transition region models. *Advances in Water Resources 42* (2012), 71–90.

[38] Jones, I. P. Low reynolds number flow past a porous spherical shell. *Mathematical Proceedings of the Cambridge Philosophical Society 73*, 1 (1973), 231238.

[39] Joseph, D., Nield, D., and Papanicolaou, G. Nonlinear equation governing flow in a saturated porous medium. *Water Resources Research 18*, 4 (1982), 1049–1052.

[40] Juncu, G., and Popa, C. Brinkman-forchheimer-darcy flow past an impermeable cylinder embedded in a porous medium. *INCAS Bulletin 7*, 4 (2015), 95.

[41] Kalliadasis, S., Ruyer-Quil, C., Scheid, B., and Velarde, M. G. *Falling liquid films*, vol. 176. Springer Science & Business Media, 2011.

[42] Kandel, H., and Pascal, J. Inclined fluid-film flow with bottom filtration. *Physical Review E 88*, 5 (2013), 052405.

[43] Kandel, H. N., and Liang, D. The long wave fluid flows on inclined porous media with nonlinear forchheimers law. *AIP Advances 9*, 9 (2019), 095302.

[44] Kandel, H. N., and Liang, D. The mass-preserving solution-flux scheme for multi-layer interface parabolic equations. *Applied Numerical Mathematics 160* (2021), 42–64.

[45] Kandilarov, J. D., and Vulkov, L. G. The immersed interface method for a nonlinear chemical diffusion equation with local sites of reactions. *Numerical Algorithms 36*, 4 (2004), 285–307.

[46] Kaoui, B., Lauricella, M., and Pontrelli, G. Mechanistic modelling of drug release from multi-layer capsules. *Computers in Biology and Medicine 93* (2018), 149–157.

[47] Kapitza, P., and Kapitza, S. Wave flow of thin viscous fluid layers. *Zh. Eksp. Teor. Fiz 18*, 3 (1948).

[48] Kim, J., and Moin, P. Application of a fractional-step method to incompressible navier-stokes equations. *Journal of Computational Physics 59*, 2 (1985), 308–323.

[49] Kundu, P. K., Cohen, I. M., and Dowling, D. Fluid mechanics 4th, 2008.

[50] Lai, M.-C., Shiue, M.-C., and Ong, K. C. A simple projection method for the coupled navier-stokes and darcy flows. *Computational Geosciences 23*, 1 (2019), 21–33.

[51] Layton, W. J., Schieweck, F., and Yotov, I. Coupling fluid flow with porous media flow. *SIAM Journal on Numerical Analysis 40*, 6 (2002), 2195–2218.

[52] Leveque, R. J., and Li, Z. The immersed interface method for elliptic equations with discontinuous coefficients and singular sources. *SIAM Journal on Numerical Analysis 31*, 4 (1994), 1019–1044.

[53] Levy, A., Levi-Hevroni, D., Sorek, S., and Ben-Dor, G. Derivation of forchheimer terms and their verification by application to waves propagation in porous media. *International Journal of Multiphase Flow 25*, 4 (1999), 683–704.

[54] Li, C., and Zhao, S. A matched peaceman–rachford adi method for solving parabolic interface problems. *Applied Mathematics and Computation 299* (2017), 28–44.

[55] Li, Z. An augmented cartesian grid method for stokes–darcy fluid–structure interactions. *International Journal for Numerical Methods in Engineering 106*, 7 (2016), 556–575.

[56] Li, Z., Chen, X., and Zhang, Z. On multiscale adi methods for parabolic pdes with a discontinuous coefficient. *Multiscale Modeling & Simulation 16*, 4 (2018), 1623–1647.

[57] Li, Z., and Ito, K. Maximum principle preserving schemes for interface problems with discontinuous coefficients. *SIAM Journal on Scientific Computing 23*, 1 (2001), 339–361.

[58] Liang, D., and Zhou, Z. The conservative splitting domain decomposition method for multicomponent contamination flows in porous media. *Journal of Computational Physics 400* (2020), 108974.

[59] Liu, G., and Si, B. C. Multi-layer diffusion model and error analysis applied to chamber-based gas fluxes measurements. *Agricultural and Forest Meteorology 149*, 1 (2009), 169–178.

[60] Liu, J., and Zheng, Z. A dimension by dimension splitting immersed interface method for heat conduction equation with interfaces. *Journal of Computational and Applied Mathematics 261* (2014), 221–231.

[61] Liu, R., and Liu, Q. Instabilities of a liquid film flowing down an inclined porous plane. *Physical Review E 80*, 3 (2009), 036316.

[62] Liu, W., Cui, J., and Xin, J. A block-centered finite difference method for an unsteady asymptotic coupled model in fractured media aquifer system. *Journal of Computational and Applied Mathematics 337* (2018), 319–340.

[63] Liu, X.-D., Fedkiw, R. P., and Kang, M. A boundary condition capturing method for poisson's equation on irregular domains. *Journal of Computational Physics 160*, 1 (2000), 151–178.

[64] March, N. G., and Carr, E. J. Finite volume schemes for multilayer diffusion. *Journal of Computational and Applied Mathematics 345* (2019), 206–223.

[65] Moraiti, M. On the quasistatic approximation in the stokes–darcy model of groundwater–surface water flows. *Journal of Mathematical Analysis and Applications 394*, 2 (2012), 796–808.

[66] Mosthaf, K., Baber, K., Flemisch, B., Helmig, R., Leijnse, A., Rybak, I., and Wohlmuth, B. A coupling concept for two-phase compositional porous-medium and single-phase compositional free flow. *Water Resources Research 47*, 10 (2011).

[67] Nield, D. A., Bejan, A., et al. *Convection in porous media*, vol. 3. Springer, 2006.

[68] Pascal, J. Linear stability of fluid flow down a porous inclined plane. *Journal of Physics D: Applied Physics 32*, 4 (1999), 417.

[69] Pascal, J. Instability of power-law fluid flow down a porous incline. *Journal of Non-newtonian Fluid Mechanics 133*, 2-3 (2006), 109–120.

[70] Pascal, J., and DAlessio, S. Instability in gravity-driven flow over uneven permeable surfaces. *International Journal of Multiphase Flow 36*, 6 (2010), 449–459.

[71] Pozrikidis, C. A note on the regularization of the discrete poisson–neumann problem. *Journal of Computational Physics 172*, 2 (2001), 917–923.

[72] Rebhi, R., Mamou, M., and Alliche, M. Form drag effect and hopf bifurcation in dupuit-darcy thermal convection in a shallow well-packed porous enclosure. *Physics of Fluids 26*, 7 (2014), 074104.

[73] Rees, D., Postelnicu, A., and Storesletten, L. The onset of darcy–forchheimer convection in inclined porous layers heated from below. *Transport in Porous Media 64*, 1 (2006), 15–23.

[74] Reis, G., Tasso, I., Souza, L., and Cuminato, J. A compact finite differences exact projection method for the navier–stokes equations on a staggered grid with fourth-order spatial precision. *Computers & Fluids 118* (2015), 19–31.

[75] Rivière, B., and Yotov, I. Locally conservative coupling of stokes and darcy flows. *SIAM Journal on Numerical Analysis 42*, 5 (2005), 1959–1977.

[76] Rodrigo, M. R., and Worthy, A. L. Solution of multilayer diffusion problems via the laplace transform. *Journal of Mathematical Analysis and Applications 444*, 1 (2016), 475–502.

[77] Rybak, I., and Magiera, J. A multiple-time-step technique for coupled free flow and porous medium systems. *Journal of Computational Physics 272* (2014), 327–342.

[78] Rybak, I., Magiera, J., Helmig, R., and Rohde, C. Multirate time integration for coupled saturated/unsaturated porous medium and free flow systems. *Computational Geosciences 19*, 2 (2015), 299–309.

[79] Sadiq, I. M. R., and Usha, R. Thin newtonian film flow down a porous inclined plane: stability analysis. *Physics of Fluids 20*, 2 (2008), 022105.

[80] Saffman, P. G. On the boundary condition at the surface of a porous medium. *Studies in Applied Mathematics 50*, 2 (1971), 93–101.

[81] Samanta, A., Goyeau, B., and Ruyer-Quil, C. A falling film on a porous medium. *Journal of Fluid Mechanics 716* (2013), 414.

[82] Samanta, A., Ruyer-Quil, C., and Goyeau, B. A falling film down a slippery inclined plane. *Journal of Fluid Mechanics 684* (2011), 353.

[83] Shiue, M.-C., Ong, K. C., and Lai, M.-C. Convergence of the mac scheme for the stokes/darcy coupling problem. *Journal of Scientific Computing 76*, 2 (2018), 1216–1251.

[84] Souza, L., Mendonça, M., and Medeiros, M. The advantages of using high-order finite differences schemes in laminar–turbulent transition studies. *International Journal for Numerical Methods in Fluids 48*, 5 (2005), 565–582.

[85] Temam, R. On the approximation of the solution of the navier-stokes equations by the fractional step method (i). *Archive for Rational Mechanics and Analysis 32*, 2 (1969), 135–153.

[86] Trifonov, Y. Nonlinear waves on a liquid film falling down an inclined corrugated surface. *Physics of Fluids 29*, 5 (2017), 054104.

[87] Vafai, K., and Kim, S. On the limitations of the brinkman-forchheimer-extended darcy equation. *International Journal of Heat and Fluid Flow 16*, 1 (1995), 11–15.

[88] Vassilev, D., and Yotov, I. Coupling stokes–darcy flow with transport. *SIAM Journal on Scientific Computing 31*, 5 (2009), 3661–3684.

[89] Wang, W.-C. A jump condition capturing finite difference scheme for elliptic interface problems. *SIAM Journal on Scientific Computing 25*, 5 (2004), 1479–1496.

[90] Weisbrod, N., McGinnis, T., Rockhold, M. L., Niemet, M. R., and Selker, J. S. Effective darcy-scale contact angles in porous media imbibing solutions of various surface tensions. *Water Resources Research 45*, 4 (2009).

[91] Yih, C.-S. Stability of liquid flow down an inclined plane. *The Physics of Fluids 6*, 3 (1963), 321–334.

[92] Zhang, K. K., Shotorban, B., Minkowycz, W., and Mashayek, F. A compact finite difference method on staggered grid for navier–stokes flows. *International Journal for Numerical Methods in Fluids 52*, 8 (2006), 867–881.

[93] Zhang, Z., Xu, J., and Drapaca, C. Particle squeezing in narrow confinements. *Microfluidics and Nanofluidics 22*, 10 (2018), 120.

[94] Zhao, S. A matched alternating direction implicit (adi) method for solving the heat equation with interfaces. *Journal of Scientific Computing 63*, 1 (2015), 118–137.

[95] Zhou, Y., and Wei, G.-W. On the fictitious-domain and interpolation formulations of the matched interface and boundary (mib) method. *Journal of Computational Physics 219*, 1 (2006), 228–246.

[96] Zhou, Z., and Liang, D. The mass-preserving s-ddm scheme for two-dimensional parabolic equations. *Communications in Computational Physics 19*, 2 (2016), 411–441.

[97] Zhou, Z., and Liang, D. The mass-preserving and modified-upwind splitting ddm scheme for time-dependent convection–diffusion equations. *Journal of Computational and Applied Mathematics 317* (2017), 247–273.

[98] Zhou, Z., and Liang, D. Mass-preserving time second-order explicit–implicit domain decomposition schemes for solving parabolic equations with variable coefficients. *Computational and Applied Mathematics 37*, 4 (2018), 4423–4442.